Distribution Agreement

In presenting this thesis or dissertation as a partial fulfillment of the requirements for an advanced degree from Emory University, I hereby grant to Emory University and its agents the non-exclusive license to archive, make accessible, and display my thesis or dissertation in whole or in part in all forms of media, now or hereafter known, including display on the world wide web. I understand that I may select some access restrictions as part of the online submission of this thesis or dissertation. I retain all ownership rights to the copyright of the thesis or dissertation. I also retain the right to use in future works (such as articles or books) all or part of this thesis or dissertation.

Signature:

_____   _____

Hew Ming Helen Siaw   Date

Investigating Protein and Peptide Mediated Membrane Bending Mechanisms

By

Hew Ming Helen Siaw
Doctor of Philosophy

Chemistry

_____

Brian Dyer
Advisor

_____

James Kindt
Committee Member

_____

Khalid Salaita
Committee Member

Accepted:

_____

Lisa A. Tedesco, Ph.D.
Dean of the James T. Laney School of Graduate Studies

_____

Date

Investigating Protein and Peptide Mediated Membrane Bending Mechanisms

By

Hew Ming Helen Siaw
B.A., University of Washington, Seattle, 2014

Advisor: Brian Dyer, Ph.D.

An abstract of
A dissertation submitted to the Faculty of the
James T. Laney School of Graduate Studies of Emory University
in partial fulfillment of the requirements for the degree of
Doctor of Philosophy
in Chemistry
2021

Abstract

Investigating Protein and Peptide Mediated Membrane Bending Mechanisms

By Hew Ming Helen Siaw

The ability to control and shape lipid bilayer is key to the survival of organisms, and they have evolved mechanisms to use membrane proteins as a driving force to bend membranes. In cells, membrane proteins such as the SNARE complex generates membrane curvature in synaptic vesicles such that neurotransmitter signals can be relayed. In influenza A, the pH-driven structural rearrangement of hemagglutinin is vital to fusing the viral and the host membranes and releasing ribonucleoprotein complexes into the host cell cytoplasm. The ability to remodel lipid bilayer is also essential to immune defense across living organisms. Particularly, host-defense peptides kill pathogens or viruses by folding into secondary structures on lipid membranes and ultimately disrupting pathogenic membranes or viral envelopes. This dissertation aims to study how protein and peptide conformational changes remodel lipid membranes. We explore this question from three angles: 1) the protein crowding mechanism, 2) influenza A membrane fusion, and 3) disruption of the membrane by a host-defense peptide. Together, these studies provide a better understanding of membrane bending mechanisms and the interactions between lipid and stimuli-responsive peptides.

Investigating Protein and Peptide Mediated Membrane Bending Mechanisms

By

Hew Ming Helen Siaw
B.A., University of Washington, Seattle, 2014

Advisor: Brian Dyer, Ph.D.

A dissertation submitted to the Faculty of the
James T. Laney School of Graduate Studies of Emory University
in partial fulfillment of the requirements for the degree of
Doctor of Philosophy
in Chemistry
2021

Acknowledgements

I would like to thank Dr. Brian Dyer for his advice and mentorship in helping me grow as a scientist and as a problem solver who would not be afraid of the unknown and would be willing to face challenges with determination. I am also grateful for his continuous support in my journey of career exploration and development. I would also like to thank my committee members, Dr. James Kindt and Dr. Khalid Salaita, for their constant guidance and advice throughout my graduate career.

I am also grateful to have the opportunity to work with a group of talented lab mates and to meet some of the most amazing people. In particular, I would like to thank Gokul Raghunath, Monica Sanchez, Anthony Sementilli for their encouragement and friendship, and Micah Eller for his support on the HA2 project and the pH-jump infra-red instrumentation.

Lastly, I would like to thank my parents, Heidi and Baile, and my husband, Alan, for their unconditional support and encouragement. They are a positive shining light that guides me through all the challenges throughout the journey. Without them, this would not have been possible.

Table of Contents

Chapter 5: Characterization of a Host-Defense Peptide, Urumin, and Its Interactions with Lipid membranes and the Influenza H3N2 X-31 Hemagglutinin

Chapter 6: Conclusion

List of Figures and Tables

<center>**Chapter 1:**

Introduction to Protein and Peptide Mediated Membrane Bending

H.M.H. Siaw</center>

1.1 The importance of generating curvature in lipid membranes

The ability to control and modulate the shape of membranes is vital to eukaryotic life. For example, cytoskeletal proteins push on the cell membranes to generate protrusions and mobilize cells[1]; synaptic vesicles fuse with the plasma membrane to release the neurotransmitters at neuronal synapses with the help of fusion proteins such as SNARE complex.[2] Processes to change the membrane shape, such as bending, fusing, or protruding, require energy input to overcome energetic barriers in deforming lipid bilayers: resistance to membrane bending and resistance to membrane stretching.[3-5] This energy is provided by modifying lipid compositions or from membrane proteins that make up about 50% of the membrane surface[6]. Membrane proteins provide energy to generate curvature via various mechanisms from protein binding and oligomerization to mechanochemical input from ATP and GTPases.[1] Once the energetic barrier is overcome, membranes can curve positively or negatively, forming curved structures for biological processes.[7] **(Fig. 1)**
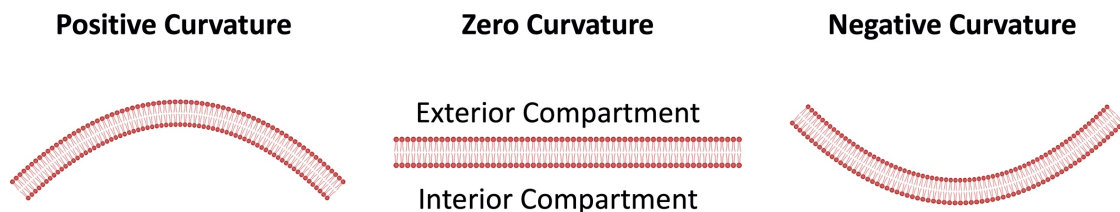
Figure 1.1 (A) Positive and negative membrane curvature.

The application of modulating membrane shape and geometry goes beyond cellular processes. Antimicrobial peptides (AMP) and host-defense peptides (HDP), an innate defense mechanism present in every multicellular organism, possess the ability to interact with lipid membranes and exert antimicrobial activities. These peptides induce membrane curvature, destabilize the membranes of pathogens and viruses, and halt their growth. [8-10] Extensive research has been dedicated to discovering HDP from natural sources such as amphibians and designing AMP for their therapeutic potential. [11]

1.2 Mechanisms to generate curvature by membrane proteins

Cells have evolved multiple solutions to the problem of overcoming membrane bending energetic barriers. One of them is utilizing and taking advantage of the membrane-associated proteins. The mechanisms contributing to membrane bending include protein scaffolding, insertion of the hydrophobic region or amphipathic helices, protein oligomerization, and protein crowding.
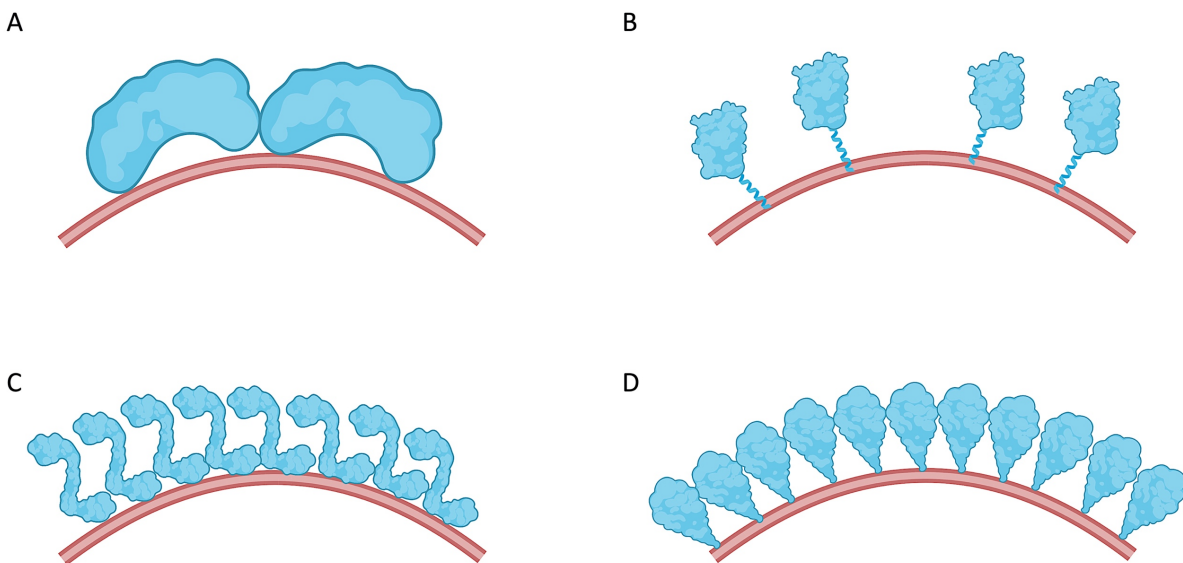
Figure 1.2 Mechanisms of protein-mediated membrane bending. (A) Protein shape. (B) Insertion of hydrophobic motif or amphipathic helices. (C) Oligomerization. (D) Protein crowding.

Protein shape

Large and intrinsically curved proteins bind to membranes and cause membrane bending. For instance, the BAR domain is crescent-shaped dimers and generates membrane curvature once bound to the membrane.[12-13] **(Fig. 2A)**

Insertion of hydrophobic protein motifs or amphipathic helices

When hydrophobic protein motif or amphipathic helices inserts between lipid headgroups on one leaflet of the lipid bilayer, it acts as a wedge and induces membrane curvature. Amphipathic helices are present on many proteins involved in membrane remodeling, such as epsin, amphiphysin, and annexin B12. Hydrophobic protein motifs include hydrophobic loops of the C2 domain of synpatotagmin-1 and Doc2b.[1, 13] **(Fig. 2B)**

Protein oligomerization

Oligomerization of several monomers into larger structures with distinct shapes can scaffold and bend membranes. Proteins from the dynamin GTPase superfamily induce membrane curvature by self-polymerizing into spirals. Coat proteins such as clathrin, COPI, COPII self-assemble into cage-like structures and induce membrane curvature essential for the process of vesicle budding.[1, 5] **(Fig. 2C)**

Protein crowding

Other membrane bending mechanisms require direct interaction and interfacing between specific proteins and the lipid membrane. In contrast, the protein crowding mechanism, which was put forth in recent years, requires no specific protein scaffolds or direct protein-lipid interaction to bend membranes. It simply states that a high surface concentration of membrane-bound protein

produces a steric pressure to bend the membrane. In particular, collisions among crowded proteins generate substantial pressure on one side of the membrane, which. If this pressure is unbalanced on the opposite membrane surface, membrane curvature can increase.[5][6, 13-14] **(Fig.2D)** Numerous experimental evidence has shown supportive evidence to this mechanism. For instance, when a high concentration of his-tagged GFP or intrinsically disordered proteins, which are known to be non-curvature generating, were bound to the Ni-NTA head group of phase-separated model liposomes, membrane tubules were observed. [15-17,18] Under the conditions of a crowded protein environment, membrane fission has also been observed. [19]

1.3 Example of protein-mediated membrane bending: Influenza A viral invasion

The process of generating membrane curvature and bending membranes play essential roles in viral infection. For viruses to enter cells and release viral RNA to the cytoplasm and subsequent viral propagation, they have to cross the lipid membranes by generating curvatures and fusing the viral and the host cell membrane.[20-21] Influenza A is one of the most common infectious diseases that causes seasonal epidemics.[22] Therefore, understanding the molecular details of its infection process and its viral coat proteins is essential for designing new therapeutics and vaccines.

Influenza A Viral Entry Process

The influenza virus initiates its infection process with its viral coat proteins, Hemagglutinin (HA). The HA protein contains 2 subunits: HA1 and HA2. The HA1 subunit binds to sialic acid receptors on the host cell and triggers endocytosis.[23] The virus then trafficks to the late endosome. The acidic pH triggers a conformational change in HA, exposing the fusion peptide in the HA protein for insertion into the endosomal membrane. [23-24] The HA protein then collapses into a trimer of hairpins and promotes the formation of a fusion pore between the endosomal membrane and the

viral membrane, which releases the viral ribonucleoproteins (RNP) into the cytosol.[21] Additional

adaptor proteins further process the viral RNP and ultimately transports it into the cellular nucleus.

[23](**Fig. 3**)
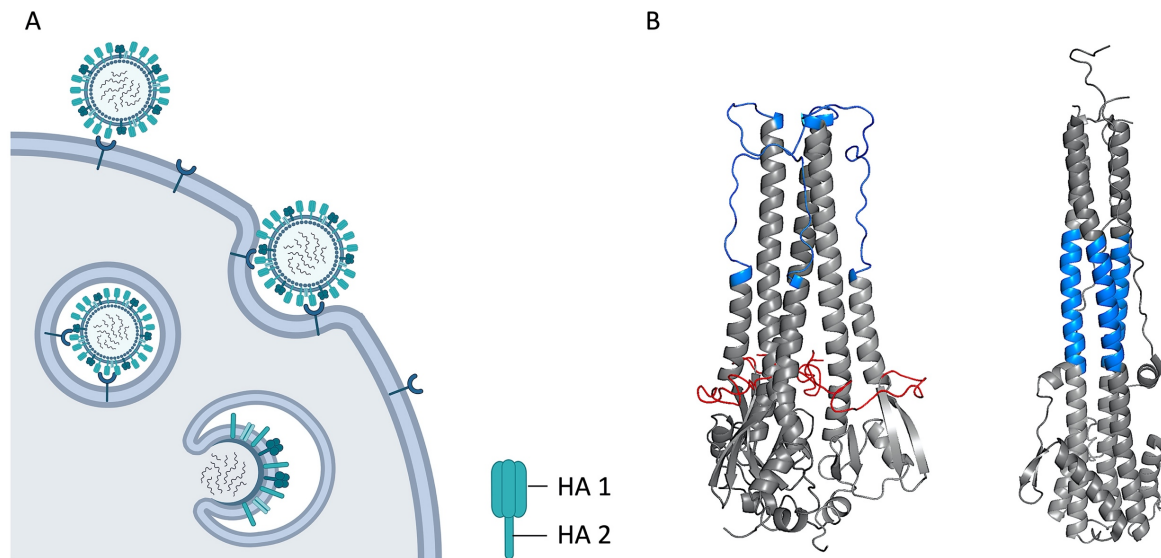
Figure 1.3 (A) Steps involved in influenza invasion and associated membrane bending events. (B)

Pre-fusion (left) and post-fusion (right) structures of HA2. The B-loop (blue) and the fusion peptide

(red) are highlighted for clarity. (PDB: 1HMQ and 1QU1)

Hemagglutinin conformational change and membrane fusion

The HA protein is a homotrimer synthesized as an inactive precursor HA0. The HA protein

covers 13.5% to 19.2% of the virus's surface area, depending on the strains and subtypes.[25]

Enzymatic cleavage of the HA0 results in two distinct subunits, HA1 and HA2, where the HA1

forms the globular head and the HA2 as the stalk and the core of the protein. The receptor-binding

domain of HA1 is bound to the sialic acid receptors on the host cell. The HA2 is a triple-stranded

alpha-helical coiled-coil with an N-terminal hydrophobic fusion peptide (FP), and a C-terminal

transmembrane domain anchors the protein to the viral membrane. At neutral pH, the FP is buried

within the hydrophobic core of the HA2 protein. [21] The protein also contains a region known as the B-loop densely populated with glutamic acid residues, and it exists as a disordered state at neutral pH.

When the virus reaches the maturing endosome, the drop of pH to a value between 5 and 6 activates a series of conformational rearrangements in the protein.[24] [26] First, the fusion peptide is released from the hydrophobic core of HA2 due to protonation of residue Asp 112. Second, protonation of residues at the HA1-HA1 interface and electrostatic repulsion between the HA1 subunits drive the HA1 dissociate. Third, the HA2 domain undergoes conformational rearrangement and achieve an intermediate structure that allows for the insertion of fusion peptide into membranes. Fourth, the C-terminal domain of the HA2 protein folds back to form an antiparallel coiled-coil, six-helix bundle scaffold, and zipping of linker leashes, bring the fusion peptide and the transmembrane domain together, promoting fusion between the viral and the host membrane. Last, the fusion between the viral and the host membrane leads to fusion pore formation. [21, 27] **(Fig. 4)**

However, the steps the HA2 protein takes to transition from the pre-fusion structure to the post-fusion structure, specifically its intermediate states, remains unknown. Two hypotheses have been proposed to explore the intermediate steps that prompt the FP insertion into the target membrane.

The first hypothesis is known as the "spring-loaded" mechanism and has shaped our understanding of how type 1 fusion protein functions as a whole. This hypothesis suggests that the HA trimer maintains a high-energy, metastable configuration at neutral pH. There is a downhill drive towards the formation of an extended coiled-coil intermediate.[28-31]. Upon acidification, the unstructured B loop folds into a coiled-coil, which relocates the FP ~100 Å towards the host

membrane for insertion. This mechanism also suggests that the interactions between HA1 and HA2 at neutral pH are key to maintaining the protein's metastability. However, the associated intermediate states and structures have not been experimentally characterized due to experimental limitations. [21, 27, 32] **(Fig. 4)**
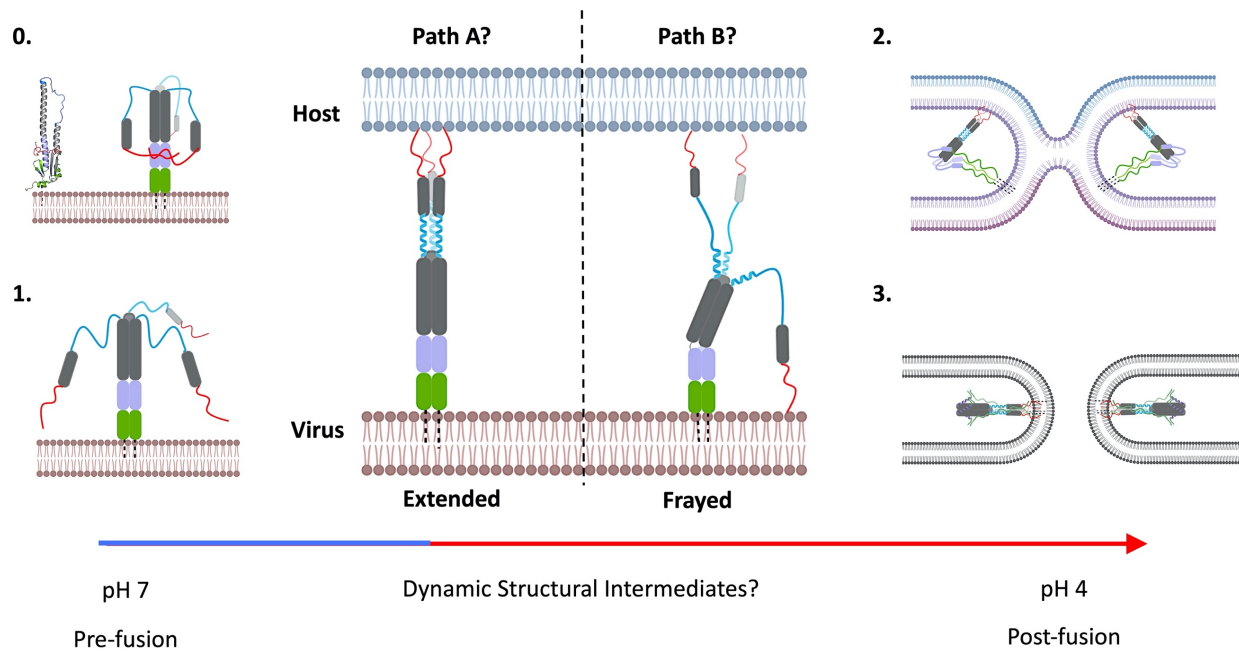
Figure 1.4 A schematic illustrating the two hypotheses: path A is the spring-loaded mechanism and path B is the mechanism suggesting the formation of a broken-symmetry intermediate.

In the second hypothesis, instead of forming a coiled-coil intermediate, partial formation of the coiled-coil results in a frayed structure with flexible C-termini containing the fusion peptides. This pathway suggests forming a broken-symmetry intermediate, which might allow the fusion peptides to insert into both the viral and host membranes.[33-34] Subsequent coiled-coil formation and zippering provide a greater free-energy release to drive dehydration and bending of the two membranes to bring them into apposition.[21] **(Fig. 4)** This mechanism is supported by molecular

dynamic simulations[33-34] and experimental studies due to methodological advancement. An HDX-MS study by Benhaim et al. observed a structurally flexible fusion domain forming before the formation of the post-fusion state. [32] In a single molecule FRET study where the HA2 was labeled with a FRET fluorescence pair, Das et al. reported the HA samples multiple intermediate conformations and maintains a highly flexible intermediate state between acid-induced HA activation and membrane fusion.[35]

Because of the different schools of thought and conflicting evidence, it is essential to discern the mechanism that causes the HA2 conformational change and describe any relevant structural intermediates that ultimately lead to membrane fusion.

1.5 Example of peptide-mediated membrane bending: host-defense peptides

Host-defense peptides (HDP, also known as antimicrobial peptides) are short, cationic peptides produced by various organisms such as animals, insects, and plants.[36] These peptides have diverse amino acid sequences, show inhibitory activity against micro-organisms, pathogens, and viruses.[37-38] by disrupting their membranes and causing cell lysis. Several mechanisms have been proposed to explore the peptide membrane interactions and explain the HDPs membrane disruption activity. It has been proposed that the cationic HDPs interact with the lipid membrane by binding to anionic lipid headgroups on the bacterial or viral membrane. This electrostatic interaction event then triggers the folding of the disordered or linear HDP into a variety of secondary structures, including alpha-helices, beta-sheets, turns, extended structures. Subsequent interaction of the HDP's hydrophobic region and the lipid membrane's hydrophobic core led to the insertion into the target membrane and pore formation.[36, 39] Other models have also been proposed to explain HDP's lytic activity, peptide concentration threshold, non-lytic membrane depolarization, charged

lipid clustering, electroporation, barrel stave, carpet model, toroidal pore, membrane thinning or thickening. [36, 39]

Recently, an HDP with anti-viral activity against influenza A has been isolated from frogs. The HDP, called urumin, has been shown to target H1 influenza A and bind to the HA2 stalk region but not the HA1 domain. Electron microscopy further showed that the peptide disrupts the PR8 influenza virion, implying a possible peptide-mediated membrane disruption due to peptide-membrane interactions.[40] Because of the anti-viral and anti-bacterial activity of HDPs, this class of peptides has been investigated for their therapeutic applications against diseases in clinical trials.[41]

1.6 Aims and scope of dissertation

This dissertation investigates the role of protein and peptide conformational changes in driving membrane bending from a general mechanistic perspective and in the context of influenza A. We used various biophysical techniques to study protein-mediated membrane remodeling in synthetic membranes, characterize the structure and properties of influenza hemagglutinin HA2 and its B-loop, and investigated the interactions between the anti-viral urumin peptide and synthetic membrane with lipid composition resembling the PR8 viral envelope.

In summary, Chapter 2 investigated the coupled effect of transient protein conformational changes and protein crowding in driving membrane curvature. We studied the process by triggering the unfolding of human serum album on synthetic liposomes under different protein density conditions. Chapter 3 characterized the recombinantly expressed HA2 subunit with spectroscopic and biochemical methods. We demonstrated that the *E. Coli.* expressed HA2 (HA2* and HA2**) was not metastable at pH 7 and were able to undergo structural transitions upon acidification. With stopped-flow fluorescence spectroscopy, we showed sub-millisecond folding dynamics associated

with the HA2 when acidified. Chapter 4 aimed to characterize the HA2 B-loop and used it as a model system to resolve the HA2 mediated membrane fusion kinetics. We synthesized the B-loop as a peptide (L40C) and characterized its biophysical properties. Using steady-state FRET and stopped-flow FRET, we demonstrated the peptide's ability to crosslink liposomes as it underwent the pH-driven loop-to-helix transition and coiled-coil formation. Chapter 5 studied the interactions between the HDP, urumin, with a lipid membrane. Using model membranes, we showed that the cationic peptide folded into secondary structures upon interactions with anionic lipid head groups. The peptide also did not exhibit leakage activity, suggesting that the urumin potentially disrupt lipid membranes via a non-pore forming mechanism seen in other HDPs.[39]

1.6 References

1.   McMahon, H. T.; Boucrot, E., Membrane curvature at a glance. *Journal of cell science* **2015,** *128* (6), 1065-70.

2.   Han, J.; Pluhackova, K.; Bockmann, R. A., The Multifaceted Role of SNARE Proteins in Membrane Fusion. *Front Physiol* **2017,** *8*, 5.

3.   Helfrich, W., Elastic properties of lipid bilayers: theory and possible experiments. *Z Naturforsch C* **1973,** *28* (11), 693-703.

4.   Canham, P. B., The minimum energy of bending as a possible explanation of the biconcave shape of the human red blood cell. *J Theor Biol* **1970,** *26* (1), 61-81.

5.   Stachowiak, J. C.; Brodsky, F. M.; Miller, E. A., A cost-benefit analysis of the physical mechanisms of membrane curvature. *Nature cell biology* **2013,** *15* (9), 1019-1027.

6.   Jarsch, I. K.; Daste, F.; Gallop, J. L., Membrane curvature in cell biology: An integration of molecular mechanisms. *The Journal of cell biology* **2016,** *214* (4), 375-87.

7.   Lipowsky, R., Remodeling of membrane compartments: some consequences of membrane fluidity. *Biol Chem* **2014,** *395* (3), 253-74.

8.   Zasloff, M., Antimicrobial peptides of multicellular organisms. *Nature* **2002,** *415* (6870), 389-95.

9.   Hancock, R. E.; Sahl, H. G., Antimicrobial and host-defense peptides as new anti-infective therapeutic strategies. *Nat Biotechnol* **2006,** *24* (12), 1551-7.

10.   Schmidt, N. W.; Wong, G. C., Antimicrobial peptides and induced membrane curvature: geometry, coordination chemistry, and molecular engineering. *Curr Opin Solid State Mater Sci* **2013,** *17* (4), 151-163.

11.   Pfalzgraff, A.; Brandenburg, K.; Weindl, G., Antimicrobial Peptides and Their Therapeutic Potential for Bacterial Skin Infections and Wounds. *Front Pharmacol* **2018,** *9*, 281.

12.   Chabanon, M.; Stachowiak, J. C.; Rangamani, P., Systems biology of cellular membranes: a convergence with biophysics. *Wiley Interdiscip Rev Syst Biol Med* **2017,** *9* (5).

13.   Alimohamadi, H.; Vasan, R.; Hassinger, J. E.; Stachowiak, J. C.; Rangamani, P., The role of traction in membrane curvature generation. *Mol Biol Cell* **2018,** *29* (16), 2024-2035.

14.   Derganc, J.; Copic, A., Membrane bending by protein crowding is affected by protein lateral confinement. *Biochim Biophys Acta* **2016,** *1858* (6), 1152-9.

15.   Scheve, C. S.; Gonzales, P. A.; Momin, N.; Stachowiak, J. C., Steric Pressure between Membrane-Bound Proteins Opposes Lipid Phase Separation. *Journal of the American Chemical Society* **2013,** *135* (4), 1185-1188.

16.   Stachowiak, J. C.; Schmid, E. M.; Ryan, C. J.; Ann, H. S.; Sasaki, D. Y.; Sherman, M. B.; Geissler, P. L.; Fletcher, D. A.; Hayden, C. C., Membrane bending by protein-protein crowding. *Nature cell biology* **2012,** *14* (9), 944-9.

17.   Stachowiak, J. C.; Hayden, C. C.; Sasaki, D. Y., Steric confinement of proteins on lipid membranes can drive curvature and tubulation. *Proceedings of the National Academy of Sciences* **2010,** *107* (17), 7781-7786.

18.   Busch, D. J.; Houser, J. R.; Hayden, C. C.; Sherman, M. B.; Lafer, E. M.; Stachowiak, J. C., Intrinsically disordered proteins drive membrane curvature. *Nature communications* **2015,** *6*, 7875.

19.   Snead, W. T.; Hayden, C. C.; Gadok, A. K.; Zhao, C.; Lafer, E. M.; Rangamani, P.; Stachowiak, J. C., Membrane fission by protein crowding. *Proceedings of the National Academy of Sciences* **2017,** *114* (16), E3258-E3267.

20.   Lorizate, M.; Krausslich, H. G., Role of lipids in virus replication. *Cold Spring Harb Perspect Biol* **2011,** *3* (10), a004820.

21.	Boonstra, S.; Blijleven, J. S.; Roos, W. H.; Onck, P. R.; van der Giessen, E.; van Oijen, A. M., Hemagglutinin-Mediated Membrane Fusion: A Biophysical Perspective. *Annu Rev Biophys* **2018,** *47*, 153-173.

22.	Dunning, J.; Thwaites, R. S.; Openshaw, P. J. M., Seasonal and pandemic influenza: 100 years of progress, still much to learn. *Mucosal Immunol* **2020,** *13* (4), 566-573.

23.	Dou, D.; Revol, R.; Ostbye, H.; Wang, H.; Daniels, R., Influenza A Virus Cell Entry, Replication, Virion Assembly and Movement. *Front Immunol* **2018,** *9*, 1581.

24.	Hamilton, B. S.; Whittaker, G. R.; Daniel, S., Influenza virus-mediated membrane fusion: determinants of hemagglutinin fusogenic activity and experimental approaches for assessing virus fusion. *Viruses* **2012,** *4* (7), 1144-68.

25.	Wasilewski, S.; Calder, L. J.; Grant, T.; Rosenthal, P. B., Distribution of surface glycoproteins on influenza A virus determined by electron cryotomography. *Vaccine* **2012,** *30* (51), 7368-73.

26.	Garcia, N. K.; Guttman, M.; Ebner, J. L.; Lee, K. K., Dynamic changes during acid-induced activation of influenza hemagglutinin. *Structure* **2015,** *23* (4), 665-76.

27.	Dyer, R. B.; Eller, M. W., Dynamics of hemagglutinin-mediated membrane fusion. *Proceedings of the National Academy of Sciences of the United States of America* **2018,** *115* (35), 8655-8657.

28.	Leikina, E.; LeDuc, D. L.; Macosko, J. C.; Epand, R.; Epand, R.; Shin, Y. K.; Chernomordik, L. V., The 1-127 HA2 construct of influenza virus hemagglutinin induces cell-cell hemifusion. *Biochemistry* **2001,** *40* (28), 8378-86.

29.	Carr, C. M.; Chaudhry, C.; Kim, P. S., Influenza hemagglutinin is spring-loaded by a metastable native conformation. *Proceedings of the National Academy of Sciences of the United States of America* **1997,** *94* (26), 14306-13.

30.	Carr, C. M.; Kim, P. S., A spring-loaded mechanism for the conformational change of influenza hemagglutinin. *Cell* **1993,** *73* (4), 823-32.

31.   Tamm, L. K., Hypothesis: spring-loaded boomerang mechanism of influenza hemagglutinin-mediated membrane fusion. *Biochim Biophys Acta* **2003,** *1614* (1), 14-23.

32.   Benhaim, M. A.; Mangala Prasad, V.; Garcia, N. K.; Guttman, M.; Lee, K. K., Structural monitoring of a transient intermediate in the hemagglutinin fusion machinery on influenza virions. *Sci Adv* **2020,** *6* (18), eaaz8822.

33.   Lin, X.; Noel, J. K.; Wang, Q.; Ma, J.; Onuchic, J. N., Atomistic simulations indicate the functional loop-to-coiled-coil transition in influenza hemagglutinin is not downhill. *Proceedings of the National Academy of Sciences of the United States of America* **2018,** *115* (34), E7905-E7913.

34.   Lin, X.; Eddy, N. R.; Noel, J. K.; Whitford, P. C.; Wang, Q.; Ma, J.; Onuchic, J. N., Order and disorder control the functional rearrangement of influenza hemagglutinin. *Proceedings of the National Academy of Sciences of the United States of America* **2014,** *111* (33), 12049-54.

35.   Das, D. K.; Govindan, R.; Nikic-Spiegel, I.; Krammer, F.; Lemke, E. A.; Munro, J. B., Direct Visualization of the Conformational Dynamics of Single Influenza Hemagglutinin Trimers. *Cell* **2018,** *174* (4), 926-937 e12.

36.   Haney, E. F.; Straus, S. K.; Hancock, R. E. W., Reassessing the Host Defense Peptide Landscape. *Front Chem* **2019,** *7*, 43.

37.   Mookherjee, N.; Anderson, M. A.; Haagsman, H. P.; Davidson, D. J., Antimicrobial host defence peptides: functions and clinical potential. *Nat Rev Drug Discov* **2020,** *19* (5), 311-332.

38.   Brice, D. C.; Diamond, G., Antiviral Activities of Human Host Defense Peptides. *Curr Med Chem* **2020,** *27* (9), 1420-1443.

39.   Nguyen, L. T.; Haney, E. F.; Vogel, H. J., The expanding scope of antimicrobial peptide structures and their modes of action. *Trends Biotechnol* **2011,** *29* (9), 464-72.

40.   Holthausen, D. J.; Lee, S. H.; Kumar, V. T.; Bouvier, N. M.; Krammer, F.; Ellebedy, A. H.; Wrammert, J.; Lowen, A. C.; George, S.; Pillai, M. R.; Jacob, J., An Amphibian Host Defense

Peptide Is Virucidal for Human H1 Hemagglutinin-Bearing Influenza Viruses. *Immunity* **2017,** *46* (4), 587-595.

41.   Ting, D. S. J.; Beuerman, R. W.; Dua, H. S.; Lakshminarayanan, R.; Mohammed, I., Strategies in Translating the Therapeutic Potentials of Host Defense Peptides. *Front Immunol* **2020,** *11*, 983.

Chapter 2:

Peripheral Protein Unfolding Drives Membrane Bending

2.1 Abstract

Dynamic modulation of lipid membrane curvature can be achieved by a number of peripheral protein binding mechanisms such as hydrophobic insertion of amphipathic helices and membrane scaffolding. Recently, an alternative mechanism was proposed in which crowding of peripherally bound proteins induces membrane curvature through steric pressure generated by lateral collisions. This effect was enhanced using intrinsically disordered proteins that possess high hydrodynamic radii, prompting us to explore whether membrane bending can be triggered by the folding-unfolding transition of surface-bound proteins. We utilized histidine-tagged human serum albumin bound to Ni-NTA-DGS containing liposomes as our model system to test this hypothesis. We found that reduction of the disulfide bonds in the protein resulted in unfolding of HSA, which subsequently led to membrane tubule formation. The frequency of tubule formation was found to be significantly higher when the proteins were unfolded while being localized to a phase-separated domain as opposed to randomly distributed in fluid phase liposomes, indicating that the steric pressure generated from protein unfolding can drive membrane deformation. Our results are critical for the design of peripheral membrane protein-immobilization strategies and open new avenues for exploring mechanisms of membrane bending driven by conformational changes of peripheral membrane proteins.

2.2 Introduction

Generation of membrane curvature is essential to cell function. Important cellular processes such as cell signaling, vesicle trafficking, membrane fusion, endocytosis and many others,[1, 2] depend on protein structural dynamics at the membrane interface and coupled membrane responses. The interplay between membrane geometry and protein structural dynamics is complex. Dynamin, for example, assembles into helical polymers at necks of budding vesicles and directly participates in membrane-remodeling events through a GTP hydrolysis-dependent conformational change.[3] Alternatively, the membrane interface may induce the folding of intrinsically disordered proteins.[4] For example, α-synuclein folds into α-helical structure from initially disordered random coil upon membrane binding.[5] This transition has a strong influence on membrane structure, resulting in membrane thinning[6] and induction of membrane curvature.[7] For these reasons, the effect of membrane bound proteins on shaping membranes has been of immense interest and the subject of intense study. Several classic protein-mediated membrane bending mechanisms have been proposed in the literature.[2, 8, 9] The hydrophobic insertion mechanism postulates that insertion of amphipathic helices bends the membrane by generating defects between phosphate head groups, whereas scaffolding proteins are thought to generate membrane curvature by molding it into the shape of the protein.[8]

A new membrane bending mechanism has been proposed recently in which crowding of peripherally bound proteins locally confined on the membrane surface induces curvature independent of protein scaffolding or membrane insertion.[10-12] Stachowiak *et al.* reported that confining His-tagged GFP on membrane domains generates enough steric pressure from lateral protein collisions to drive membrane bending.[12] Chen *et al.* used pipette aspiration to quantitatively study the ability of protein crowding to generate membrane curvature under controlled membrane tension. [11] Similar behavior was observed when intrinsically disordered proteins were confined to the liquid disordered domain of

phase separated liposomes.[13] A recent report suggests lateral pressure from protein crowding can stretch and bend the membrane, and leads to membrane fission.[14] Additionally, theoretical analysis has shown that crowded membrane- bound proteins generate substantial pressure at membrane surfaces.[15] These observations suggest crowding of proteins locally confined on membrane surface, such as a region of membrane phase separation, may function as a general mechanism of membrane bending regardless of the specific protein structures involved. While the efficacy of protein crowding in bending membranes still remains a subject of debate,[16] the coupled effects of protein crowding and protein conformational changes on membrane geometry have not been investigated despite the dynamic nature of protein structures. Consequently, the goal of the present study was to investigate whether a transient change in protein conformation can induce membrane curvature.

Our approach was simple in concept: tightly bind a protein to the membrane surface with protein binding lipid (Ni-NTA-DGS), then unfold it and probe the effect on membrane curvature. But this was difficult in practice, since most protein unfolding methods directly perturb the membrane, including temperature,[17] denaturants such as guanidine hydrochloride[18] and acid-induced unfolding.[19] We chose His-tagged human serum albumin[20] as a model for this study because the helical structure of HSA is stabilized by 17 disulfide bridges.[21] Reduction of these disulfide bonds by 1,4-dithiothreitol (DTT)[22] triggers unfolding of the protein and increases the Stokes radius by 1.2 fold,[23, 24] but DTT by itself does not perturb the membrane structure. We have used DTT triggered unfolding of HSA to induce membrane bending, tubulation and budding in model membrane systems.

2.3 Experimental Procedures

Large unilamellar liposomes and giant unilamellar vesicles preparation

Non-phase-separated liposomes (NPSL) contain POPC plus 10-30 mol% Ni-NTA-DGS. Composition for phase-separated liposomes (PSL) was chosen according to published composition[25]

and contains 12.5 mol% fluid phase lipid (DPhPC plus 10-30 mol% Ni-NTA-DGS), 40 mol% DPPC, 47.5 mol% cholesterol. The overall concentration of Ni-NTA-DGS is smaller in PSL than in NPSL. For instance, the overall Ni-NTA-DGS concentration in 20 mol% Ni-NTA lipid doped 1 mM PSL, where the Ni-NTA modified lipid partitions preferentially into the liquid-disordered domain, is 0.025 mM. 1 mM 20 mol% Ni-NTA lipid dopes PSL contains 0.2 mM overall Ni-NTA-DGS. Large unilamellar vesicles (LUV, referred to as liposomes) were prepared by extrusion. Lipid mixtures in chloroform solutions were dried on the inner wall of a small flask using compressed air and then lyophilized overnight under vacuum at -42 °C. Lipid cakes were rehydrated to a final concentration of 2 mM with MOPS buffer (20 mM MOPS, 100 mM NaCl, pH 7.2) for 1 hour at room temperature for NPSL or at 60 °C for PSL and vortexed occasionally. The resulting solutions were extruded through a 100 nm pore size single polycarbonate membrane (Whatman/GE Healthcare) 20 times to produce a clear solution of liposomes.

Giant unilamellar vesicles (referred to as GUV) were prepared according to a published protocol. [26] A thin film of lipid was first deposited onto an ITO coated slide and dried under vacuum for 2 hours. The lipid film was then rehydrated with 350 mM sucrose solution (~350 mOsm) to 1 mM final lipid concentration. Electroformation was performed at room temperature for non-phase-separated GUV (NPS GUV) and at 60 °C for phase-separated GUV (PS GUV). PS GUV were slow cooled overnight and NPS GUV were cooled to room temperature before experiments. Small quantities of fluorescent lipid probes (0.05 mol% Texas Red DHPE) were used to label liquid-disordered phase in PS GUV (DPhPC) and NPS GUV (POPC).

Tryptophan Fluorescence Measurement of HSA with and without DTT

20 μM human serum albumin solution was prepared with Tris HCl buffer. To unfold the protein, it was incubated with 200 mM DTT for 2 hours at room temperature. Concentration was

verified with absorbance at 280 nm using a Nanodrop 2000 spectrophotometer (ThermoFisher Scientific, Waltham, MA). Fluorescence measurements were taken on a FluoroMax spectrophotometer (Horiba Scientific, Edison, New Jersey) with a 1 cm fluorescence cuvette. Data was collected using 2 nm excitation and emission slit widths, exciting tryptophan at 295 nm with an integration time of 1 s over a total range of 285-550 nm.

Circular Dichroism

Secondary structure of 20 μM human serum albumin after incubating with 200 mM DTT for 2 hours was confirmed with CD spectroscopy. CD spectra were measured on a JASCO J-810 spectrophotometer (Jasco, Inc., Easton, MD). Samples were transferred to a quartz cuvette with a 1 mm path length. The scanning range of the instrument was set between 190-260 nm at a rate of 100 nm/min with a 2 s response time and 2 nm spectral bandwidth. Helical contents in folded and unfolded HSA were calculated using mean residue ellipticity at 222 nm,

$$MRE = \frac{\theta M}{ncl}$$……………………………….……………….………….……………...…..(Equation 1)

where θ is observed ellipticity (mdeg), c is protein concentration, l is cuvette pathlength, M is molecular weight of protein, n is the number of peptide bonds. Percent helicity is calculated as follow[27]:

$$\%Helicity = \left(\frac{-MRE222nm-3000}{33000-3000}\right) \times 100$$……………………………….………….(Equation 2)

where MRE_{222nm} is mean residue ellipticity at 222 nm, 4000 is mean residue ellipticity of β- character and random coil at 222 nm, and 33000 is mean residue ellipticity of pure helical character at 209 nm.

Equilibrium Attenuated Total Reflection Fourier Transform Infrared Spectroscopy (ATR-FTIR) of HSA in solution

ATR-FTIR measurements were performed with a Varian 660 FTIR spectrophotometer (Agilent, Santa Clara, CA) coupled to a liquid nitrogen cooled mercury cadmium telluride (MCT) detector. The internal reflection element was an 80 x 10 x 4 mm trapezoidal germanium ATR plate with an aperture angle of 45°. Ge plate was rinsed with detergent and ethanol before ATR cell assembly. Water spectrum was taken and used as background for subsequent measurements. Then, solutions of 100 µM HSA in water and 100 µM HSA with 1 mM DTT in water after 2 hours incubation were added to ATR cell respectively. Each spectrum was obtained with an average of 400 scans at 2 cm^{-1} resolution.

ATR-FTIR of HSA on Supported Lipid Bilayer

The germanium ATR reflective element was first rinsed with detergent and ethanol, then subjected to plasma cleaning for 15 minutes. The crystal was then treated with 1M H2SO4 for 15 minutes. A background of germanium ATR element and water was collected and before introducing the lipids. To form supported lipid bilayer, 2 mM PSL doped with 30 mol% Ni-NTA-DGS in fluid phase lipid was prepared at 60 °C, then added to the crystal while PSL was still at 60 °C, and allowed to incubate for 30 minutes. Water was flushed through the cell to rinse away any excess vesicles and the supported lipid bilayer spectrum was obtained.[28, 29] The supported lipid bilayer spectrum was saved and used as background spectrum for subsequent measurements. 1 µM His-tagged human serum albumin was added to the bilayer, allowed to bind to Ni-NTA for 15 minutes, and then the sample spectrum was taken. Afterwards, 1 M EDTA was added to the crystal in order to unbind His-tagged human serum albumin from the bilayer. Then, the bilayer was flushed with water in order to remove proteins, and 1 M NiCl$_2$ was added to the bilayer (final concentration 100mM) in order to recharge Ni-NTA-DGS. After flushing away NiCl$_2$ with copious amount of water, a spectrum was taken to

ensure removal of previously bound proteins from the bilayer. Then, 1 µM His-tagged human serum albumin and 10 mM DTT, pre-incubated together for 2 hours at room temperature, was added to the ATR cell. Each spectrum was obtained with an average of 400 scans at 2 cm^{-1} resolution.

Quantification of bound HSA concentration on liposomes

Fluorescence measurements were taken on a FluoroMax spectrophotometer (Horiba Scientific, Edison, New Jersey) with a 1 cm fluorescence cuvette. Data were collected using 2 nm excitation and emission slit widths, exciting the fluorophore at 488 nm with an integration time of 1 s over a total range of 285-550 nm. A calibration curve was first generated by measuring fluorescence intensities of 0.05, 0.1, 0.3, 0.5, 0.7, 0.9, and 1 µM of Alexa488 labelled His-tagged HSA at 525 nm (Fig. S9). Then, 1 mM of PSL and NPSL with 20 mol% Ni-NTA- DGS in liquid-disordered phase were incubated with 1 µM Alexa488 labelled His-tagged HSA respectively. The mixture was allowed to incubate for 30 minutes, then filtered with an Amicon centrifugal filter unit with molecular cut-off weight of 100 kDa at 14,000 g for 10 min to remove any unbound protein. Following centrifugation, the amount of Alexa488 labelled His-tagged HSA in the flow through and in collected liposomes were quantified by measuring fluorescence intensities at 525 nm.

Giant Unilamellar Vesicles Tubulation Assay

PS GUV and NPS GUV (~1 mM) were incubated with 1 µM Alexa488 labelled His-tagged HSA with or without 4 mM DTT for 2 hours. The GUV solutions were then diluted twice in 20 mM MOPS, 100 mM NaCl buffer (osmolarity adjusted with glucose to ~320 mOsm) prior to imaging at room temperature. Vesicles were observed using a confocal laser scanning microscope, a 60x oil-immersion objection, and PMT detector on a Nikon Confocal C2+ microscope (Melville, NY).

Vesicles were excited with a laser at 488 nm and/or at 561 nm. Confocal images and movies were analyzed with IMAGE J software (National Institutes of Health, Bethesda, MD).

Modelling of Steric Pressure Generated by Protein Unfolding on Giant Unilamellar Liposomes

We used a previously established thermodynamic model of membrane steric pressure[12] to compare our experimental results with the predicted effect of steric pressure on membrane bending. To compute the steric pressure generated by the bound protein layer before and after unfolding, we used the Carnahan-Starling equation of state for hard disks.[12, 30] The intrinsic assumption of this model is that the proteins are considered as spherical, non-attracting disks with uniform dimensions. Stokes radii values used for the calculation (native HSA r ~ 3.52 nm and reduced unfolded HSA r ~ 4.22 nm) were based on results obtained from size exclusion chromatography.[23] Considering the membrane-protein interface as a two-dimensional interface, the Carnahan-Starling equation can be described as follows.

$$p = \frac{4\eta}{\sigma^2 \pi}\left[1 + 2\eta \; \frac{1 - 0.44\eta}{(1-\eta)^2}\right] k_b \ldots\ldots\ldots\ldots\ldots\ldots\ldots\ldots\ldots\ldots\ldots\ldots\ldots\ldots\text{(Equation 3)}$$

The pressure is denoted by , described in terms of free energy per unit area. The protein height is denoted by σ, and fraction of membrane area covered by the protein is denoted by . k_b and T denote the Boltzmann constant and temperature respectively.

In our experiments, we modified the Ni-NTA loading density to modulate dissociation constants of the protein binding to the membrane surface. While the exact HSA binding constants were not determined directly, a reasonable assumption is that the values will fall within 1 nM to 5 µM from previously published results.[31, 32] The binding constants will affect the fraction of protein bound to the surface, in turn, affecting the fraction coverage. The fraction of proteins bound to the surface was estimated as follows.

$$\theta = \frac{[HSA]}{[HSA]+K_d}$$ ....(Equation 4)

Here, θ denotes the fraction of proteins bound to the surface. [HSA] denotes the concentration of the protein solution and K_d denotes the dissociation constant of 6x His-HSA binding to the Ni-NTA-DGS liposome surface. The number of liposomes in solution and overall available membrane surface area were determined by assuming the head group area of ~0.71 nm^2 for phosphatidylcholine lipids. [33]

2.4 Results and Discussion

Reductive Unfolding of HSA

We optimized conditions for reductive unfolding of HSA using multiple spectroscopic probes, including tryptophan fluorescence, circular dichroism (CD)spectroscopy, ATR-FTIR (**Fig. 1**) and dynamic light scattering (DLS) (**Fig. S1A-B**). Addition of DTT to a solution of HSA caused the tryptophan fluorescence to blue shift (**Fig. 1A**), consistent with previous work that demonstrated this unusual signature of HSA unfolding.[23, 34] Time-dependent tryptophan fluorescence measurements were performed to determine the incubation time necessary for protein unfolding (**Fig. S1D**). The CD spectrum also indicates some loss of the helix bands at 208 and 222 nm in the presence of DTT (**Fig. 1B**), clear evidence of HSA unfolding while retaining ~60% helical character. The infrared amide I band, arising from C=O stretching vibrations of polypeptide backbone carbonyls, is an indicator of secondary and tertiary structural changes due to its sensitivity to hydrogen bonding and to vibrational coupling. The second derivative of the amide I band is particularly sensitive to protein aggregation, showing sharp minima at 1620 and 1680 cm^{-1} due to formation of β-aggregates.[35] The second derivative spectrum of HSA (**Fig. 1C**) highlights subcomponents of the broad amide I absorbance, with minima at 1630 and 1650 cm^{-1} assigned to solvated and buried helices respectively.[36] The

minimum at 1650 cm^{-1} dominates the second derivative spectrum as expected for the predominantly

α-helical HSA, while a minimum at 1630 cm^{-1} indicates some solvated helix structure. Importantly,

the well-established signatures of antiparallel β-sheet structures characteristic of protein aggregation

are not observed for the reduced, unfolded protein, indicating that it is not aggregated.
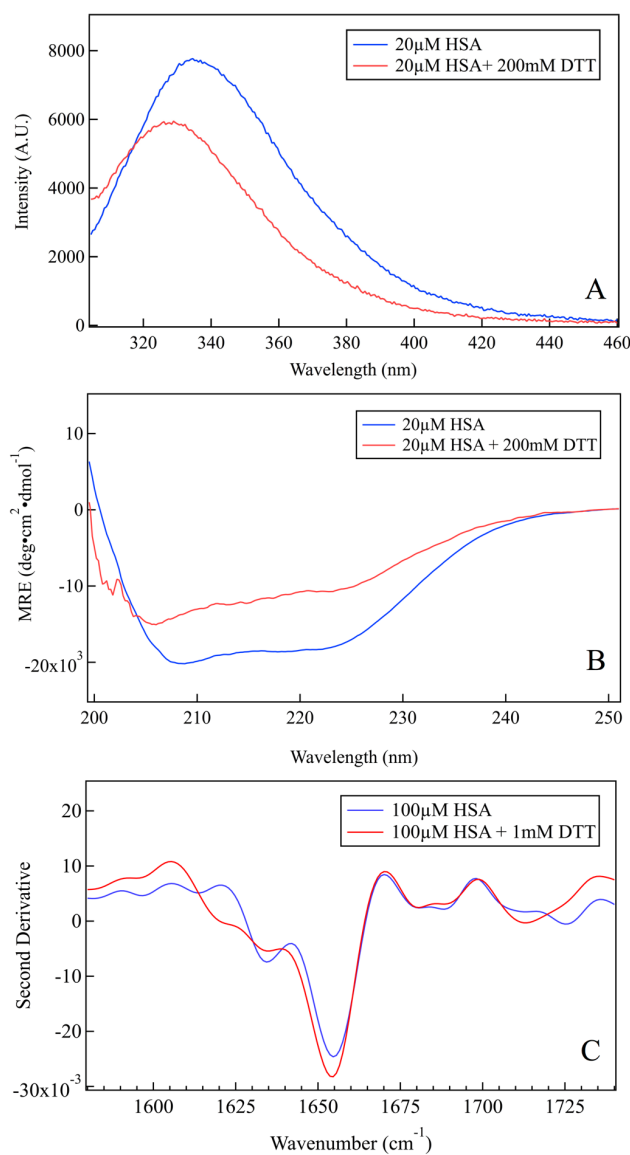
Figure 2.1 Characterization of HSA unfolding at room temperature. (A) Tryptophan fluorescence blue shifts upon reduction by DTT, characteristic of HSA unfolding. (B) Far-UV CD spectrum of folded HSA shows minima at 208 and 222 nm, characteristic of α-helical proteins; the

helix peaks decrease on addition of DTT, indicating substantial unfolding of HSA. (C) Second derivative ATR-FTIR spectrum shows a decrease of the helix bands and no aggregation of unfolded HSA.

Effect of HSA Unfolding on Large Unilamellar Liposomes

Phase-separated liposomes (PSL) with coexisting liquid-disordered (DPhPC) and liquid-ordered (DPPC) phases were used to investigate the effect of protein unfolding on membrane bending, and compared to liquid disordered (POPC) non-phase-separated liposomes (NPSL) as a control. Non-phase-separated liposomes (NPSL) are composed of POPC (+20 mol% Ni-NTA-DGS), whereas phase-separated liposomes are composed of 12.5 mol% fluid phase lipid (DPhPC + 20 mol% Ni-NTA-DGS), 40 mol% DPPC, and 47.5 mol% cholesterol. Thus, Ni-NTA-DGS occupies 2.5 mol% of the total lipid composition in PSL and makes up 20 mol% of the total lipid composition in NPSL. The composition chosen for phase separated liposomes corresponds to a region in the DPhPC/DPPC/cholesterol phase diagram where the separation of liquid-ordered and liquid disordered phases is distinct and persists up to high temperature (up to 45 °C) (**Fig. 2A**).[12, 37] DPhPC and POPC have similar bending rigidities ($\sim 10^{-20}$ J) as reported previously.[38, 39] HSA was first bound to the liposome surface via interaction of its His-tag with Ni-NTA functionalized DGS lipid head groups ($K_d \sim nM$)[40] present at 20 mol% in the liquid-disordered phase of lipid membrane, then unfolded by DTT.

Ni-NTA-DGS lipid partitions preferentially into the liquid disordered phase of PSL, due to its unsaturated hydrocarbon tail, thus resulting in an increase in local protein concentration of the bound His-tagged HSA only in the liquid-disordered phase. In contrast, the control 2 mM NPSL consisted of a single phase, liquid-disordered lipid (POPC), which led to random distribution of Ni-NTA-DGS, and hence the His-tagged HSA over the full surface area of the vesicle. Because of the difference in

distribution of His-tagged HSA, we expect a higher local protein density in PSL over NPSL (**Fig. 2B**) by maintaining the same doping level of Ni-NTA-DGS lipid in the liquid-disordered phase.

Dynamic light scattering was used 1) to determine the autocorrelation function decay times of free liposomes and HSA bound liposomes, 2) to compare the change in decay time of folded HSA relative to reductively unfolded HSA bound to liposomes, and 3) to compare effects of HSA binding and HSA unfolding on PSL versus NPSL (**Fig. 2C, D**). The DLS autocorrelation decay time is related to the liposome diffusion time and thus serves as a qualitative measure of liposome tubulation.

PSL showed a small increase in decay time upon binding of HSA at a 20 mol% Ni-NTA-DGS doping level in liquid-disordered phase (**Fig. 2C, blue trace**). Upon unfolding of HSA on PSL, a significantly larger increase in decay time was observed (**Fig. 2C, red trace**). In contrast, NPSL showed very little change in decay time upon protein binding and protein unfolding (**Fig. 2D**). We interpret the substantial increase in decay time for PSL upon protein unfolding to an increase in the diffusion time as a result of membrane bending and tubulation. We expect the formation of tubules to cause more solvent drag and consequently to slow down diffusion of the liposomes through solution. A similar effect is not observed in NPSL, therefore we conclude that tubulation does not occur in this case. We attribute the lack of tubulation to the lower local density of bound protein that results from dispersing the His-tagged HSA uniformly over the entire liposome surface. A slight increase in decay time was observed for NPSL with bound, unfolded HSA (Fig. 2D, red trace), not surprising since the hydrodynamic radius of free, unbound HSA increases substantially upon unfolding (**Fig. S1A, B**).
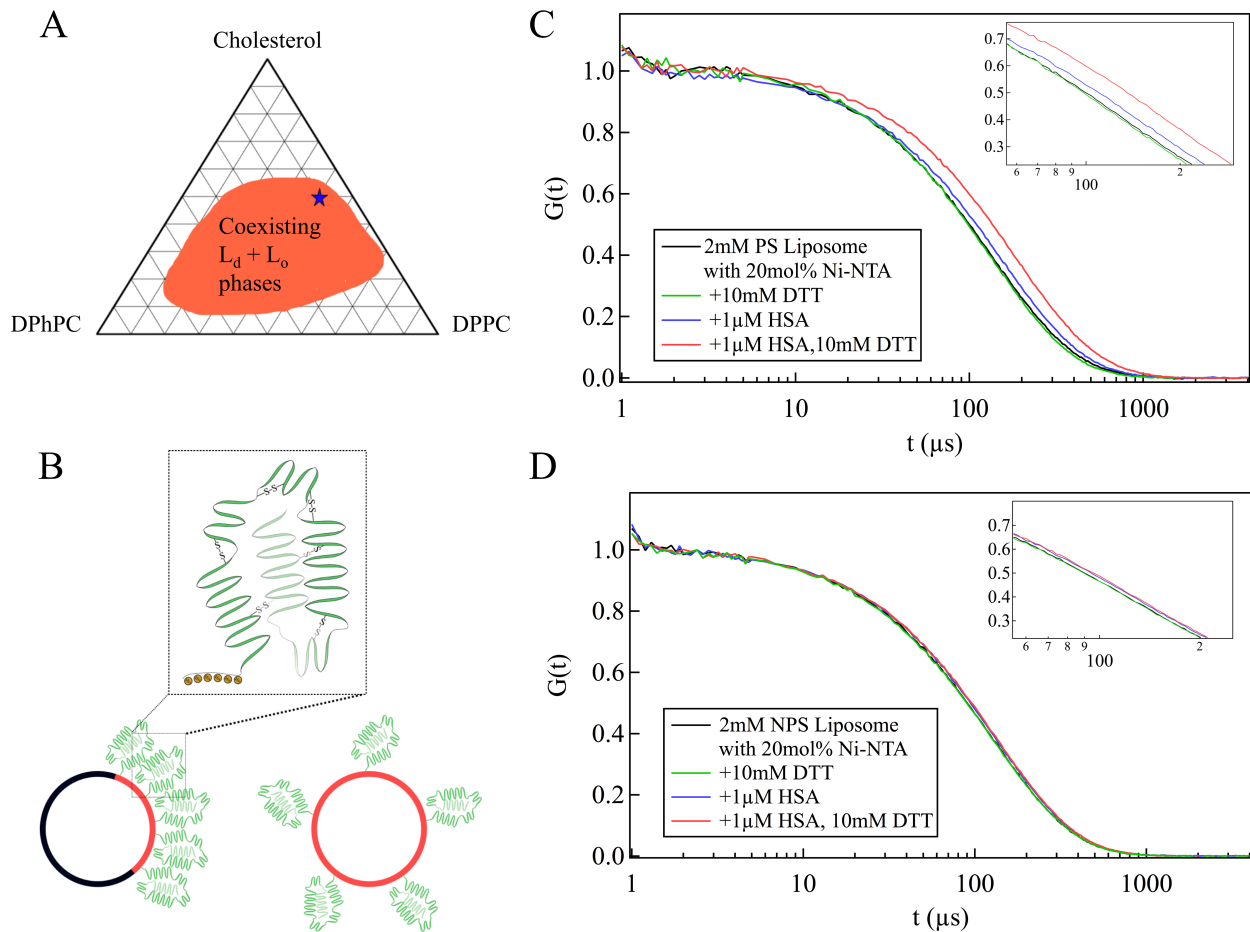
Figure 2.2 Effect of protein unfolding on lipid membranes. (A) Ternary phase diagram of DPhPC, DPPC, cholesterol at 25 °C.[12, 37] Blue star indicates selected lipid composition. (B) Depiction of distribution of liquid-disordered phase, Ni-NTA-DGS, and bound proteins in PSL (left) and NPSL (right). In PSL, liquid-disordered (Ld, red) and liquid-ordered (Lo, black) phases coexist, with Ld occupying one side of the liposome. Thus, His-tagged HSA bound to Ni-NTA-DGS is concentrated on one side of the liposome. In NPSL, His-tagged HSA bound to Ni-NTA-DGS is distributed throughout the entire surface of the liposome. Normalized DLS autocorrelation functions of (C) 2 mM PSL and (D) 2 mM NPSL with 20 mol% Ni-NTA-DGS in liquid-disordered domain, incubated with HSA (blue traces) or HSA with DTT (red traces).
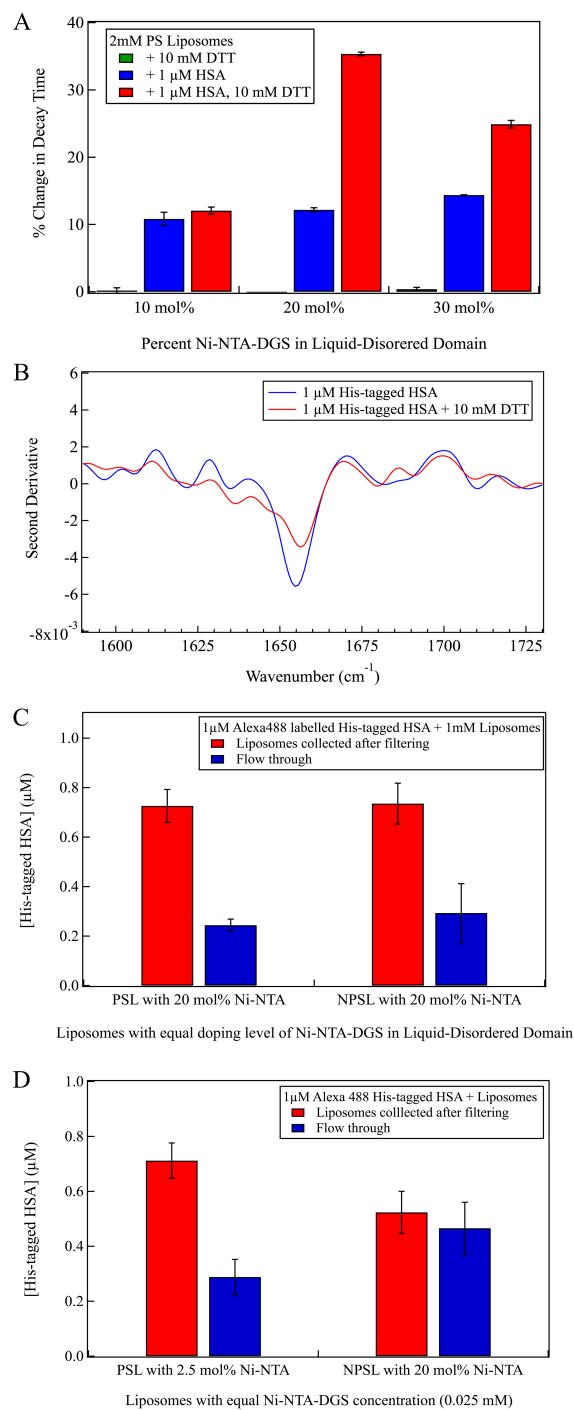
Figure 2.3 (A) Percent change in autocorrelation decay time of PSL measured after protein incubation for Ni-NTA-DGS doping levels of $10-30$ mol% in the liquid-disordered phase. (B) Second derivative IR spectrum of HSA (blue trace), HSA with DTT (red trace) on phase- separated supported lipid bilayer with 30 mol% Ni-NTA-DGS. (C&D) Fluorescence assay of bound and free HSA

concentrations (1 µM total [HSA]) for 1 mM PSL and NPSL liposomes with (C) equal doping levels (20 mol%) of Ni-NTA-DGS in liquid disordered domain and (D) equal total Ni-NTA-DGS concentrations (0.025 mM).

To investigate how coupling protein unfolding to protein crowding affects membrane curvature, we varied the percentage of Ni-NTA-DGS (10 - 30 mol% in liquid-disordered phase) to change the number of binding sites available to His-tagged HSA. Similar to the previous experiments, we first bound HSA to the membrane, then unfolded the protein with DTT. Figure 3A shows the effects of varying doping level of Ni-NTA-DGS in liquid-disordered phase of PSL in the presence of native HSA and reductively unfolded HSA (**Fig. S3 shows the corresponding G(t) curves. Table S2 shows decay time values**). Decay times shown were obtained by fitting autocorrelation functions to a single exponential. Insignificant differences in autocorrelation decay times with native and unfolded HSA were observed for 10 mol% Ni-NTA-DGS doped PSL. These results suggest that the crowding effect generated by concentrating either native or unfolded HSA on liquid-disordered phase is small at lower doping level. In contrast, at higher doping level (30 mol% Ni-NTA-DGS), the crowding effect appears to saturate, such that there is a smaller difference in autocorrelation decay times between folded and unfolded HSA on PSL compared to a doping level of 20 mol% Ni-NTA-DGS. Thus, the effect of crowding appears to be resolved best at the intermediate Ni-NTA-DGS doping level.

Using transmission electron microscopy, we observed that unfolding HSA on lipid membrane is capable of generating highly curved membrane structures in PSL with 20 mol% Ni-NTA-DGS in liquid-disordered phase, whereas folded HSA causes limited deformation (**Fig. S5B**). In PSL and NPSL with 10 mol% Ni-NTA lipid in liquid-disordered phase, folded and unfolded HSA did not alter liposome geometry (**Fig. S5A**), which agreed with dynamic light scattering measurements.

Assessing whether HSA Bound to the Lipid Bilayer Aggregates when Unfolded

To investigate whether aggregation of unfolded HSA contributes to the observed membrane bending, we performed ATR-FTIR spectroscopy on supported lipid bilayer to probe the protein structure. 1 µM his-tagged HSA was first bound to supported lipid bilayer (lipid composition remains the same as PSL), then unfolded by incubating with 10 mM DTT. As a control, we performed the same experiment without any DTT. Figure 3B shows second derivative ATR-FTIR spectra of 1 µM his-tagged HSA and 1 µM reductively unfolded his-tagged HSA bound to 30 mol% Ni-NTA-DGS containing phase-separated supported lipid bilayer. In both cases, the characteristic features of aggregated protein at 1620 cm^{-1} and 1680 cm^{-1} are clearly missing. Unfolding of His-tagged HSA in phase separated lipid systems did not generate aggregates even at the highest Ni-NTA-DGS doping level. C-H stretching bands at 2850 cm^{-1} and 2920 cm^{-1} are indicators of bilayer stability. showed binding of HSA and unfolding of HSA had no effect on the lipid bilayer (**Fig. S4B**). [29] Signature of C-H stretching region remained unchanged after the addition of 100 mM NiCl$_2$ (final concentration), therefore the supported lipid bilayer was not affected by the NiCl$_2$ treatment (**Fig. S4C**).

Quantification of Bound HSA on Liposomes

The concentrations of protein bound to PSL and NPSL under our experimental conditions were quantified and compared using fluorescence spectroscopy. We attached Alexa488 dye to His-tagged HSA and measured the fluorescence intensity of Alexa 488 fluorophore at 525 nm. A calibration curve was generated to convert measured fluorescence intensity to protein concentration (**Fig. S9**). Figure 3C shows concentrations of His-tagged HSA bound to 1 mM PSL and 1 mM NPSL with 20 mol% Ni-NTA-DGS in liquid-disordered phase as quantified by the Alexa 488 fluorescence. It is important to note that the liposome composition was designed to yield 20 mol% Ni-NTA-DGS

in the liquid-disordered phase for both PSL and NPSL, therefore the total Ni-NTA-DGS concentration in PSL is smaller because the fraction of liquid disordered phase is smaller in this case. Therefore, 1 mM PSL contains 12.5 mol% DPhPC as liquid-disordered phase, and thus contains 0.025 mM Ni-NTA-DGS (20 mol% of the liquid-disordered phase). In contrast, 1 mM NPSL contains 0.2 mM Ni-NTA-DGS. Since PSL has 8-fold fewer Ni-NTA-DGS than NPSL, PSL should have 8-fold fewer binding sites and the amount of bound protein should be 8-fold less. However, we observed that PSL and NPSL with same doping level of Ni-NTA-DGS (20 mol%) have similar amount of protein bound (~1 % difference), despite the difference in absolute number of binding sites (**Fig. 3C**). These results demonstrate that the density of HSA bound to the liquid-disordered phase is substantially higher for PSL compared to NPSL.

We repeated the same experiment maintaining the total concentration of Ni-NTA-DGS at 0.025 mM for both PSL and NPSL (**Fig. 3D**). In this case, PSL contains 2.5 mol% Ni-NTA-DGS in liquid-disordered domain and NPSL contains 20 mol% Ni-NTA-DGS. The measurement clearly demonstrates that when PSL and NPSL have identical overall concentrations of Ni-NTA-DGS hence with same number of binding sites, more proteins are bound to PSL (~1.5 fold more) (**Fig. 3D**).

The difference in bound-protein density between PSL and NPSL has been demonstrated quantitatively in previous publications. [10, 12] Also, previous studies have shown a positive correlation between binding strength of His-tagged HSA and an increase in Ni-NTA-DGS density in the membrane.[41] Since the mechanism of interaction between His-tag and Ni-NTA is universal, irrespective of the protein that carries the his-tag, we attribute the difference in bound-protein concentration to multi-valency of the His-tag interaction with the Ni-NTA, which enhances its binding affinity

We studied the membrane bending processes due to HSA unfolding with single-vesicle imaging using confocal fluorescence microscopy. First, we exposed electroformed phase-separated giant unilamellar vesicles (PS GUV) and their non-phase-separated counterparts (NPS GUV; same composition as large unilamellar liposomes) to folded HSA, then induced protein unfolding with DTT. We monitored protein binding and giant liposomes geometry changes by confocal fluorescence imaging.

First, the Alexa488 fluorophore attached to His-tagged HSA via a thiol-maleimide linkage acts as a reporter to monitor protein binding to the membrane. Second, in order to distinguish the liquid-disordered from liquid-ordered phases, the liquid-disordered phases of PS GUV and NPS GUV were doped with Texas Red DHPE, which is known to partition into the liquid-disordered phase.[42] The overlapping signal on images and intensity profile from Alexa488 and Texas Red indicated binding of his-tagged HSA to the liquid disordered phase of GUV (**Fig. 4A and 4B**). These results also provide additional evidence for partitioning of the Ni-NTA-DGS lipid into the liquid-disordered phase in PS GUV and NPS GUV.

Upon incubation of the protein bound GUV with DTT, highly flexible tubules with diffraction-limited diameters and dynamically fluctuating conformations were observed (**Fig. 4D, Movie S1**). This observation indicates an increase in spontaneous curvature of the membrane caused by enhanced lateral pressure generated from collisions between unfolded membrane bound proteins.[10, 43, 44] We varied the percentage of Ni-NTA-DGS lipid in the fluid domain of GUV to change the density of His-tagged protein bound to the membrane surface. The number of GUV that formed tubules was found to depend on the doping level of Ni-NTA-DGS in the liquid disordered domain. The percentage of GUV forming tubules in the presence of folded and unfolded HSA was plotted relative to the percentage of Ni-NTA-DGS content in liquid-disordered domain of lipid vesicles in **Figure**

4C. The resulting increase in tubule formation follows the trend predicted by the Carnahan-Starling equation[12] as shown in the overlaid curves in **Fig. 4C**. These data demonstrate qualitatively that the unfolding transition of HSA together with protein density on the liquid-disordered domain of lipid membrane affect the frequency of tubule formation. Observation of vesicles budding at PS GUV containing 30 mol% Ni-NTA-DGS (**Fig. 4D**) further highlights the coupled impact on membrane geometry.
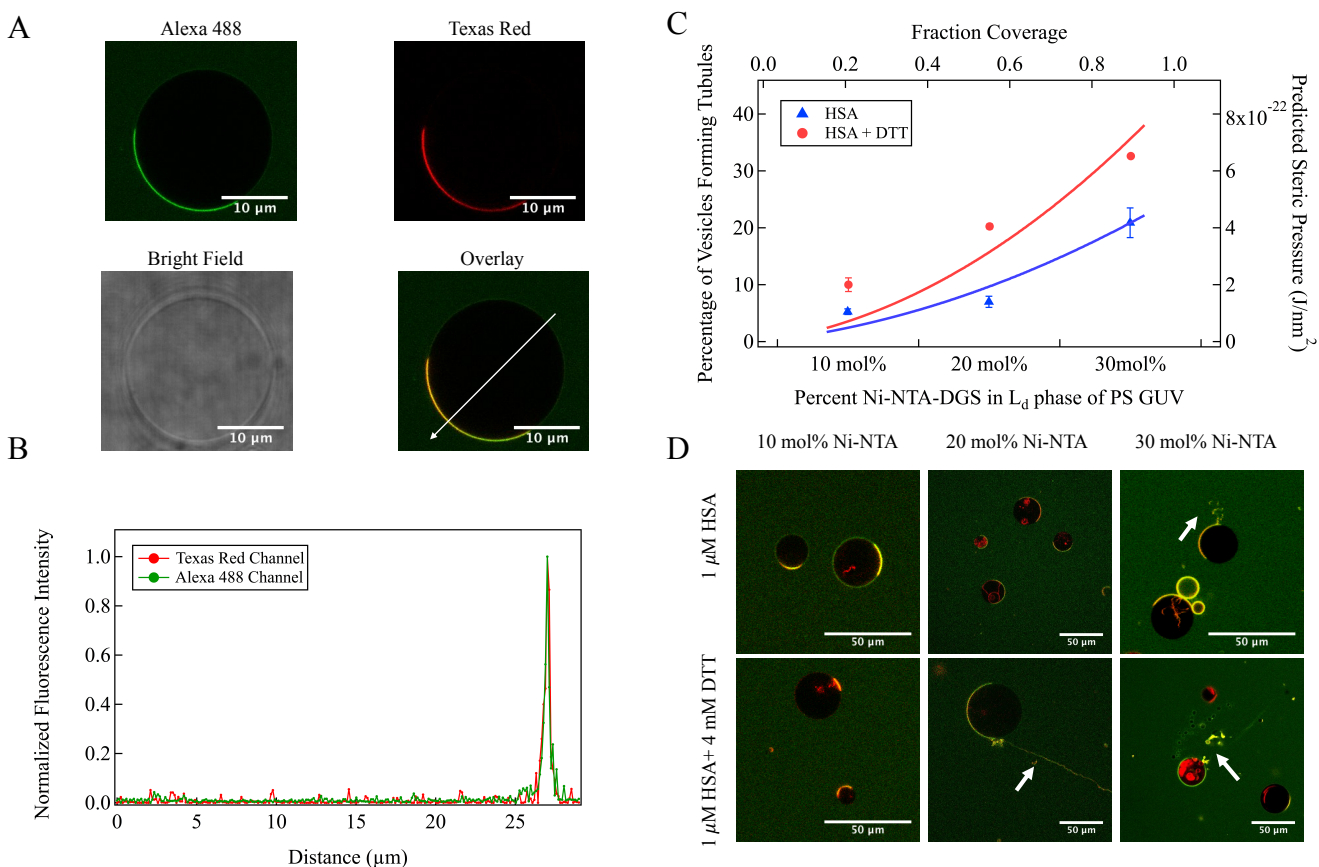
Figure 2.4 GUV tubulation Assay. (A) Confocal images of PSL GUV (+20 mol% Ni-NTA-DGS in fluid domain) incubated with 1 μM Alexa 488 labelled His- tagged HSA. Scale bar, 10 μm long. (B) Fluorescence intensity profile of PS GUV incubated with HSA, measured along the white arrow on the overlaid image. (C) Solid lines: theoretical prediction of steric pressure generated from lateral collisions versus fraction coverage for folded (blue trace) and unfolded (red trace) HSA on PS GUV.

Symbols: qualitative measurement of percentage of GUVs forming tubules determined from confocal fluorescence images as a function of increasing percentage of Ni-NTA-DGS in liquid-disordered phase in PS GUV. N = 3 independent experiments, >100 GUVs per experiment. S.D. calculated from 3 independent trials. (D) Representative confocal fluorescence images of PS GUVs containing 10, 20, 30 mol% Ni-NTA-DGS in liquid- disordered domain after incubation with HSA (upper images) or HSA with DTT (lower images). Scale bar, 50 μm long. Green color represents Alexa 488 labelled His-tagged HSA, while red color represents Texas Red doped liquid-disordered domain of GUV. Yellow color indicated overlap between the two. White arrows indicate tubules from GUV.

2.5 Conclusions

In summary, by reductively unfolding membrane bound HSA with DTT, we investigated the effect of an induced protein conformational change (unfolding) on membrane curvature. We found that the process of unfolding of a model membrane bound protein can drive membrane bending. This study improves our understanding of the contribution of protein crowding and the role of protein conformational change on membrane curvature generation. Our results are important for developing peripheral membrane protein-immobilization strategies and they open new avenues for exploring the role of conformational changes in membrane bending driven by peripheral membrane-protein interaction.

2.6 References

[1] Smith, A. W. (2012) Lipid-protein interactions in biological membranes: a dynamic perspective, *Biochim Biophys Acta 1818*, 172-177.

[2] Kirchhausen, T. (2012) Bending membranes, *Nature Cell Biology 14*, 906-908.

[3] Ferguson, S. M., and De Camilli, P. (2012) Dynamin, a membrane-remodelling GTPase, *Nat Rev Mol Cell Biol 13*, 75-88.

[4] Hofmann, H., Soranno, A., Borgia, A., Gast, K., Nettels, D., and Schuler, B. (2012) Polymer scaling laws of unfolded and intrinsically disordered proteins quantified with single-molecule spectroscopy, *Proc Natl Acad Sci U S A 109*, 16155-16160.

[5] Ferreon, A. C., Gambin, Y., Lemke, E. A., and Deniz, A. A. (2009) Interplay of alpha-synuclein binding and conformational switching probed by single-molecule fluorescence, *Proc Natl Acad Sci U S A 106*, 5645-5650.

[6] Shi, Z., Sachs, J. N., Rhoades, E., and Baumgart, T. (2015) Biophysics of alpha-synuclein induced membrane remodelling, *Phys Chem Chem Phys 17*, 15561-15568.

[7] Jiang, Z., de Messieres, M., and Lee, J. C. (2013) Membrane remodeling by alpha-synuclein and effects on amyloid formation, *J Am Chem Soc 135*, 15970-15973.

[8] McMahon, H. T., and Boucrot, E. (2015) Membrane curvature at a glance, *J Cell Sci 128*, 1065-1070.

[9] Zimmerberg, J., and Kozlov, M. M. (2006) How proteins produce cellular membrane curvature, *Nat Rev Mol Cell Biol 7*, 9-19.

[10] Stachowiak, J. C., Hayden, C. C., and Sasaki, D. Y. (2010) Steric confinement of proteins on lipid membranes can drive curvature and tubulation, *Proc Natl Acad Sci U S A 107*, 7781-7786.

[11] Chen, Z., Atefi, E., and Baumgart, T. (2016) Membrane Shape Instability Induced by Protein Crowding, *Biophys J 111*, 1823-1826.

[12] Stachowiak, J. C., Schmid, E. M., Ryan, C. J., Ann, H. S., Sasaki, D. Y., Sherman, M. B., Geissler, P. L., Fletcher, D. A., and Hayden, C. C. (2012) Membrane bending by protein-protein crowding, *Nat Cell Biol 14*, 944-949.

[13] Busch, D. J., Houser, J. R., Hayden, C. C., Sherman, M. B., Lafer, E. M., and Stachowiak, J. C. (2015) Intrinsically disordered proteins drive membrane curvature, *Nat Commun 6*, 7875.

[14] Snead, W. T., Hayden, C. C., Gadok, A. K., Zhao, C., Lafer, E. M., Rangamani, P., and Stachowiak, J. C. (2017) Membrane fission by protein crowding, *Proceedings of the National Academy of Sciences 114*, E3258-E3267.

[15] Derganc, J., and Copic, A. (2016) Membrane bending by protein crowding is affected by protein lateral confinement, *Biochim Biophys Acta 1858*, 1152-1159.

[16] Kozlov, M. M., Campelo, F., Liska, N., Chernomordik, L. V., Marrink, S. J., and McMahon, H. T. (2014) Mechanisms shaping cell membranes, *Curr Opin Cell Biol 29*, 53-60.

[17] Ahmad, B., Muteeb, G., Alam, P., Varshney, A., Zaidi, N., Ishtikhar, M., Badr, G., Mahmoud, M. H., and Khan, R. H. (2015) Thermal induced unfolding of human serum albumin isomers: assigning residual alpha helices to domain II, *Int J Biol Macromol 75*, 447-452.

[18] Santra, M. K., Banerjee, A., Rahaman, O., and Panda, D. (2005) Unfolding pathways of human serum albumin: evidence for sequential unfolding and folding of its three domains, *Int J Biol Macromol 37*, 200-204.

[19] Del Giudice, A., Dicko, C., Galantini, L., and Pavel, N. V. (2017) Time-Dependent pH Scanning of the Acid-Induced Unfolding of Human Serum Albumin Reveals Stabilization of the Native Form by Palmitic Acid Binding, *J Phys Chem B 121*, 4388-4399.

[20] Pande, V. S., and Rokhsar, D. S. (1999) Molecular dynamics simulations of unfolding and refolding of a beta-hairpin fragment of protein G, *Proc Natl Acad Sci U S A 96*, 9062-9067.

[21] Carter, D. C., He, X. M., Munson, S. H., Twigg, P. D., Gernert, K. M., Broom, M. B., and Miller, T. Y. (1989) Three-dimensional structure of human serum albumin, *Science 244*, 1195-1198.

[22] Getz, E. B., Xiao, M., Chakrabarty, T., Cooke, R., and Selvin, P. R. (1999) A comparison between the sulfhydryl reductants tris(2-carboxyethyl)phosphine and dithiothreitol for use in protein biochemistry, *Anal Biochem 273*, 73-80.

[23] Lee, J. Y., and Hirose, M. (1992) Partially folded state of the disulfide-reduced form of human serum albumin as an intermediate for reversible denaturation, *J Biol Chem 267*, 14753-14758.

[24] Cleland, W. W. (1964) Dithiothreitol, a New Protective Reagent for SH Groups*, *Biochemistry 3*, 480-482.

[25] Bordovsky, S. S., Wong, C. S., Bachand, G. D., Stachowiak, J. C., and Sasaki, D. Y. (2016) Engineering Lipid Structure for Recognition of the Liquid Ordered Membrane Phase, *Langmuir 32*, 12527-12533.

[26] Angelova, M. I., and Dimitrov, D. S. (1986) Liposome electroformation, *Faraday Discussions of the Chemical Society 81*, 303.

[27] Pattanayak, R., Basak, P., Sen, S., and Bhattacharyya, M. (2017) An insight to the binding of ellagic acid with human serum albumin using spectroscopic and isothermal calorimetry studies, *Biochem Biophys Rep 10*, 88-93.

[28] Arsov, Z., and Quaroni, L. (2008) Detection of lipid phase coexistence and lipid interactions in sphingomyelin/cholesterol membranes by ATR-FTIR spectroscopy, *Biochim Biophys Acta 1778*, 880-889.

[29] Hull, M. C., Cambrea, L. R., and Hovis, J. S. (2005) Infrared spectroscopy of fluid lipid bilayers, *Anal Chem 77*, 6096-6099.

[30] Carnahan, N. F., and Starling, K. E. (1969) Equation of State for Nonattracting Rigid Spheres, *The Journal of Chemical Physics 51*, 635-636.

[31] Lauer, S. A., and Nolan, J. P. (2002) Development and characterization of Ni-NTA-bearing microspheres, *Cytometry 48*, 136-145.

[32] Dorn, I. T., Pawlitschko, K., Pettinger, S. C., and Tampe, R. (1998) Orientation and two-dimensional organization of proteins at chelator lipid interfaces, *Biological Chemistry 379*, 1151-1159.

[33] Nagle, J. F. (1993) Area Lipid of Bilayers from Nmr, *Biophysical Journal 64*, 1476-1481.

[34] Anand, U., Ray, S., Ghosh, S., Banerjee, R., and Mukherjee, S. (2015) Structural Aspects of a Protein–Surfactant Assembly: Native and Reduced States of Human Serum Albumin, *The Protein Journal 34*, 147-157.

[35] Shivu, B., Seshadri, S., Li, J., Oberg, K. A., Uversky, V. N., and Fink, A. L. (2013) Distinct beta-sheet structure in protein aggregates determined by ATR-FTIR spectroscopy, *Biochemistry 52*, 5176-5183.

[36] Gilmanshin, R., Williams, S., Callender, R. H., Woodruff, W. H., and Dyer, R. B. (1997) Fast events in protein folding: relaxation dynamics of secondary and tertiary structure in native apomyoglobin, *Proc Natl Acad Sci U S A 94*, 3709-3713.

[37] Veatch, S. L., Gawrisch, K., and Keller, S. L. (2006) Closed-loop miscibility gap and quantitative tie-lines in ternary membranes containing diphytanoyl PC, *Biophys J 90*, 4428-4436.

[38] Dimova, R. (2014) Recent developments in the field of bending rigidity measurements on membranes, *Adv Colloid Interface Sci 208*, 225-234.

[39] Vitkova, V., Meleard, P., Pott, T., and Bivas, I. (2006) Alamethicin influence on the membrane bending elasticity, *Eur Biophys J 35*, 281-286.

[40] Gizeli, E., and Glad, J. (2004) Single-step formation of a biorecognition layer for assaying histidine-tagged proteins, *Anal Chem 76*, 3995-4001.

[41] Blanchette, C. D., Fischer, N. O., Corzett, M., Bench, G., and Hoeprich, P. D. (2010) Kinetic analysis of his-tagged protein binding to nickel-chelating nanolipoprotein particles, *Bioconjug Chem 21*, 1321-1330.

[42] Baumgart, T., Hess, S. T., and Webb, W. W. (2003) Imaging coexisting fluid domains in biomembrane models coupling curvature and line tension, *Nature 425*, 821-824.

[43] Lipowsky, R. (2013) Spontaneous tubulation of membranes and vesicles reveals membrane tension generated by spontaneous curvature, *Faraday Discuss 161*, 305-331; discussion 419-359.

[44] Stachowiak, J. C., Brodsky, F. M., and Miller, E. A. (2013) A cost-benefit analysis of the physical mechanisms of membrane curvature, *Nature Cell Biology 15*, 1019-1027.

2.7 Supplemental Information

2.7.1 Supplemental Methods

Human Serum Albumin Unfolding Characterization: Tryptophan Fluorescence Emission

Time dependent tryptophan fluorescence measurements were performed by incubating 20 μM human serum albumin with 200 mM DTT for 10 mins, 30 mins, 1 hour, and 2 hours.

Human Serum Albumin Unfolding Characterization:ANS Fluorescence Emission

20 μM human serum albumin (final concentration) was incubated with various concentrations of DTT (10 mM, 20 mM, 30 mM, 40 mM, 50 mM, 60 mM, 70 mM, 80 mM, 90 mM, 100 mM) and 50 μM ANS (final concentration) for 2 hours. Fluorescence spectra were collected by excitation at 372 nm with an integration time of 1 s over total range of 285-550 nm.

Effect of HSA unfolding on liposomes: Dynamic light scattering measurement (DLS)

1 μM His-tagged human serum albumin was added to 2 mM PSL or NPSL with 10 mol% or 20 mol% or 30 mol% Ni-NTA-DGS and incubated with or without 10 mM DTT for 2 hours. 80 μL of each sample was transferred to a 1 cm quartz cuvette and data were collected with a NanoPlus-Zeta/Nano

Particle Analyzer (Particulate Systems, Norcross, GA). 3x30 measurement runs were performed, with standard setting (Refractive index = 1.331, viscosity= 0.88, temperature = 25 ℃)

Autocorrelation functions of each data set were fitted to single exponential equation to obtain decay time (τ).

$$Ae^{\frac{-t}{\tau}}$$

, where t is overall time course of decay in μs, and τ is the decay time.

Effect of HSA unfolding on liposomes: Electron microscopy imaging

Carbon 200 mesh, copper grids were glow discharged at 10 mA for 45 s with a sputter coater prior to application of any materials. PSL and NPSL incubated with His-tagged HSA and His-tagged HSA with DTT were diluted with buffer to 0.1 mM prior applying to grids for 1 min. Excess samples were removed from grids by buffer rinse and filter paper blotting. As a control, PSL, NPSL with or without DTT were also applied to grids for 1 min. Afterwards, grids were stained with 1% uranyl acetate for 1 min, then air dried at room temperature. Images were taken with a Hitachi HT-7700 transmission electron microscope at 80 kV accelerating voltage.

Protein Labelling: Ellman's Test

To quantify the number of free sulfhydryl group on His-tagged HSA for the conjugation to Alexa488 fluorescence dye with a maleimide linkage, 4mg of DTNB was dissolved in sample buffer (0.1 M Sodium phosphate, 1 mM EDTA, pH 8.0). A set of sulfhydryl standards (cysteine hydrochloride monohydrate) with concentrations of 1.5 mM, 1.25 mM, 1.0 mM, 0.75 mM, 0.5 mM, and 0.25 mM were prepared with sample buffer. A 0.5 mM HSA solution was pre-incubated with 1 mM TCEP for

15 mins. Then 250μL sample/standard, 2.5 mL sample buffer, 50 μL DTNB reagent were mixed in test tubes, incubated for 15 mins and the absorbance was measured at $\lambda_{412\,nm}$ with a Lambda35 UV/Vis spectrophotometer (Perkin Elmer, Waltham, MA). The concentration of sulfhydryl group was determined using a standard curve derived from the CysHCl standards, and with the molar extinction coefficient of DTNB at $\lambda_{412\,nm}$ (14,150 $M^{-1}cm^{-}$)[6]. We determined that this human serum albumin preparation (Sigma; lot number SLBL5290V) contained 0.51 mol –SH/mol protein.

His-tagged HSA labelling

His-tagged HSA was dissolved in 100 mM PBS (BupH Phosphate Buffered Saline Packs, ThermoFisher Scientific, Waltham, MA). The labelling reactions were performed with the thiol-reaction using maleimide functionalized dye (Alexa488 C5 Maleimide). Protein was first incubated with 10-fold molar excess of TCEP at room temperature for 1 hour, then incubated with 10 fold molar excess dye at 4 °C, stirred overnight in the dark. Upon completion of the reaction, excess glutathione was added to the solution, then stirred for 30 mins at room temperature. Excess dye molecules were removed using a ZebraSpin Desalting Column with a 7K MW cutoff (ThermoFisher Scientific, Waltham, MA).

Native Page to compare molecular weight of HSA vs. HSA reduced by DTT:

HSA was dissolved in buffer to a concentration of 1.5 mg/mL. To prepare the unfolded sample, the 1.5 mg/mL solution of HSA was incubated with 200 mM DTT for 2 hours at room temperature. Samples were diluted 1:3 in native page buffer and run on a precast gel for 2 hours at 100 V, 160 mA on ice with Tris-Glycine native running buffer. Afterwards, the gel was stained with Coomassie Blue staining solution (0.1% Coomassie Blue R230, 50% MeOH, 7% acetic acid) for 15 mins, then destained with destaining solution (5% MeOH, 7% acetic acid) overnight at room temperature.

Equilibrium ATR-FTIR of phase separated supported lipid bilayer (containing 30 mol% of Ni-NTA-DGS) with 100mM or 1M NiCl$_2$:

Cleaning of germanium crystal and preparation of phase separated supported lipid bilayer were performed according to protocol in the method section. A buffer spectrum was collected before introducing the lipids and was used a background spectrum for subsequent measurement. Supported lipid bilayer was incubated on the crystal surface for 30 minutes. Buffer was flushed through the cell to rinse away any excess vesicles. The supported lipid bilayer spectrum was taken. Afterwards, NiCl$_2$ (100mM or 1M as final concentration) was added and incubated with the bilayer for 15 minutes, then obtained a spectrum. Each spectrum was obtained with an average of 256 scans at 2 cm^{-1} resolution.

2.7.2 Supplemental Figures

1. Characterization of the DTT induced unfolding of HSA. In Figure S1, we showed that there was a change in the hydrodynamic radius of HSA once incubated with DTT for 2 hours. From the autocorrelation function of unfolded HSA, it is shown that particles diffuse much slower than folded HSA.
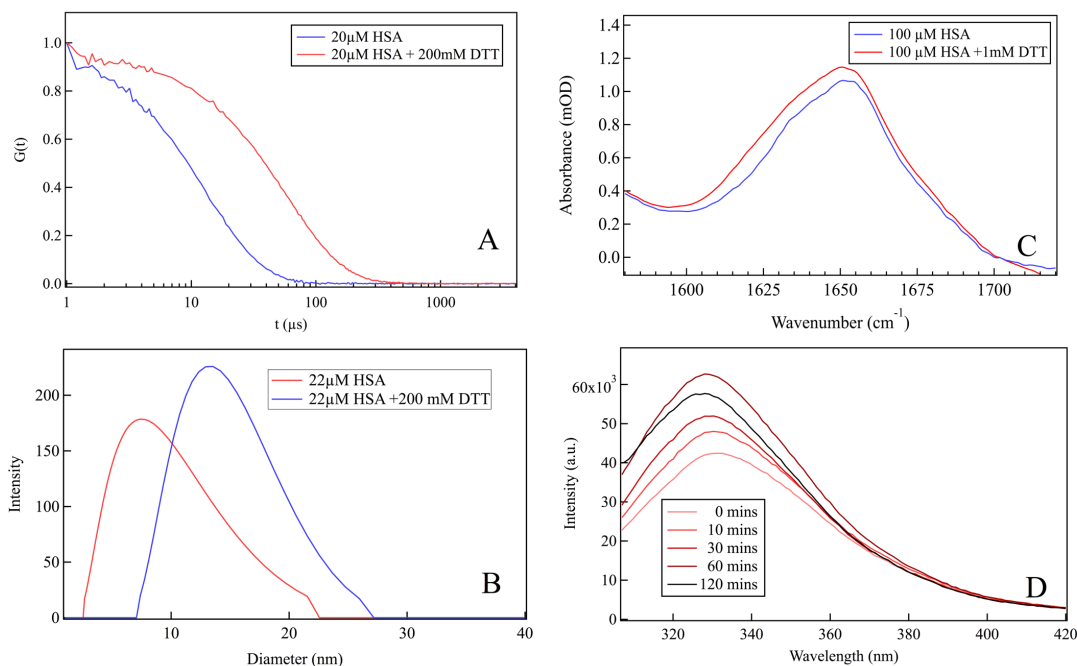
Figure S2.1 Characterization of HSA unfolding under reducing conditions. A. Dynamic light scattering autocorrelation function of unfolded HSA shows slower decay than folded HSA. B. Calculated DLS intensity profile of unfolded HSA versus folded HSA, showcasing the difference in hydrodynamic radii. C. Equilibrium ATR-FTIR absorbance spectrum in the Amide I' region. Spectra are normalized at 1550 cm^{-1} for comparison. D. Time dependent tryptophan fluorescence measurement of HSA in the presence of DTT. The graph shows blue shift in emission maxima in time dependent fashion.
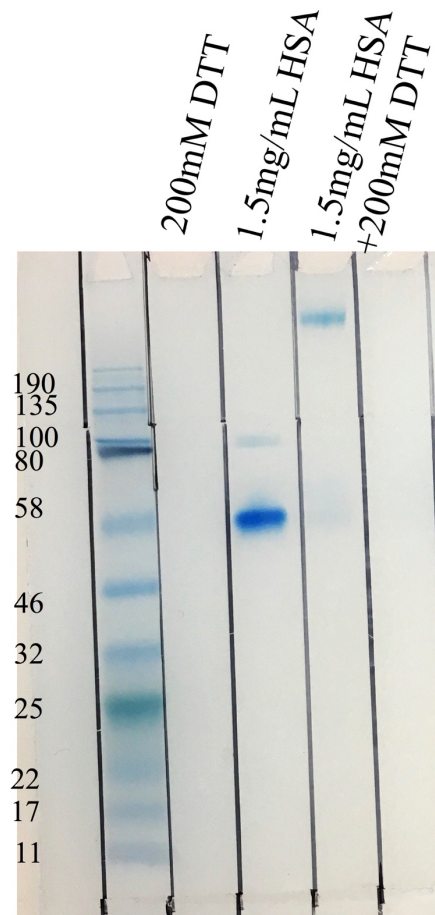
Figure S2.2 Native page of HSA and HSA unfolded with DTT. The lane containing HSA shows a band at 58 kD as expected for the native protein. In contrast, the lane containing unfolded HSA shows a band that is out of range of the protein standards, clearly indicating unfolding of the protein.
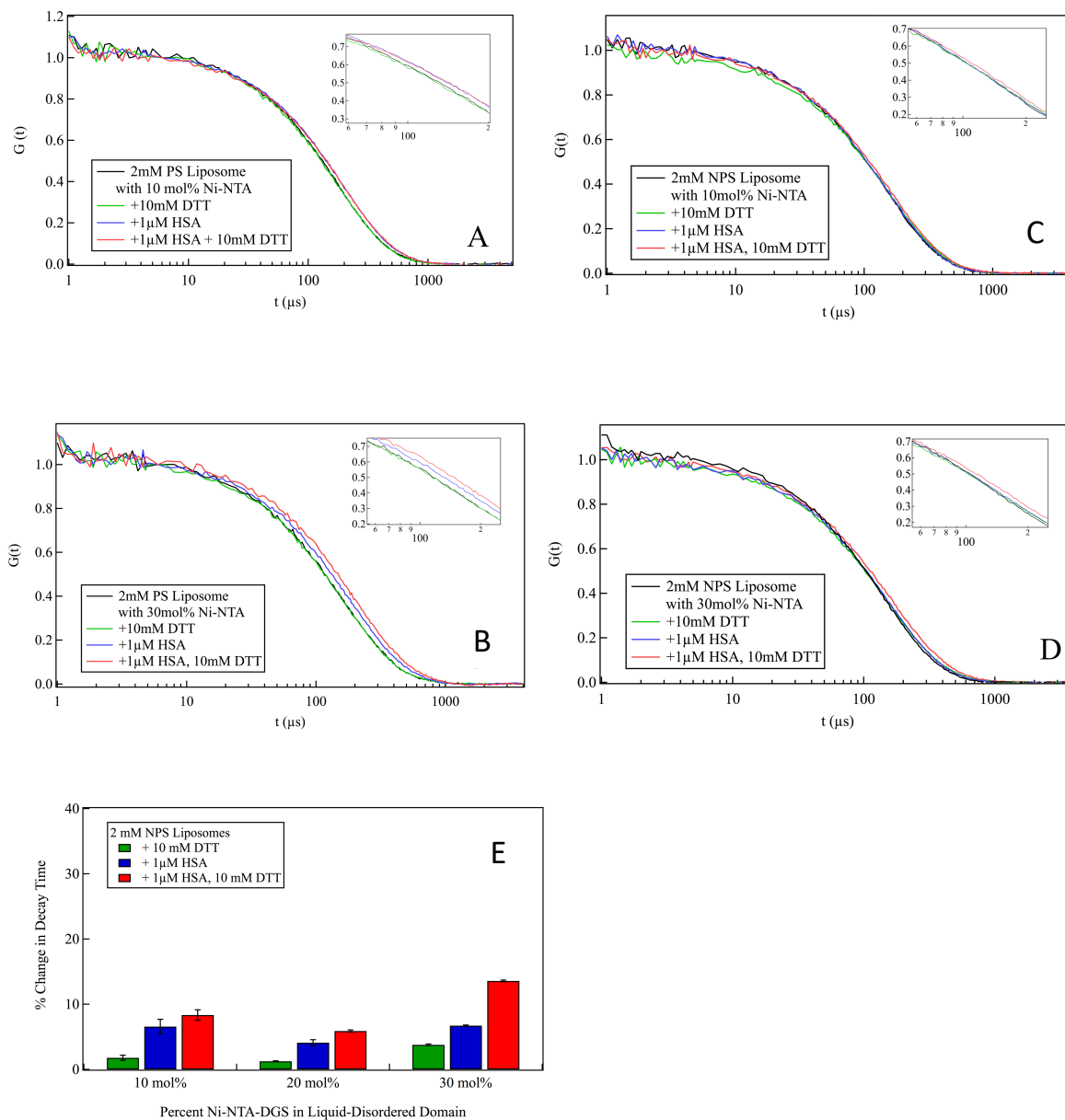
Figure S2.3 Normalized autocorrelation functions and hydrodynamic radii of PSL and NPSL containing 10 mol%, 20 mol%, and 30 mol% Ni-NTA-DGS in the presence of folded HSA and unfolded HSA. A. PSL with 10 mol% Ni-NTA shows overlapping traces for folded and unfolded HSA samples. B. PSL with 30 mol% Ni-NTA shows a slower decay in unfolded HSA than folded HSA. C. NPSL with 10 mol% Ni-NTA shows a slight difference in decay between folded and unfolded HSA D. NPSL with 30 mol% Ni-NTA shows a slower decay in unfolded HSA than folded HSA. E.

Percent change in decay time of NPSL doped with 10 mol% , 20 mol% , and 30 mol% Ni-NTA-DGS in the presence of folded and unfolded HSA. Decay times were obtained by fitting autocorrelation traces to single exponential.
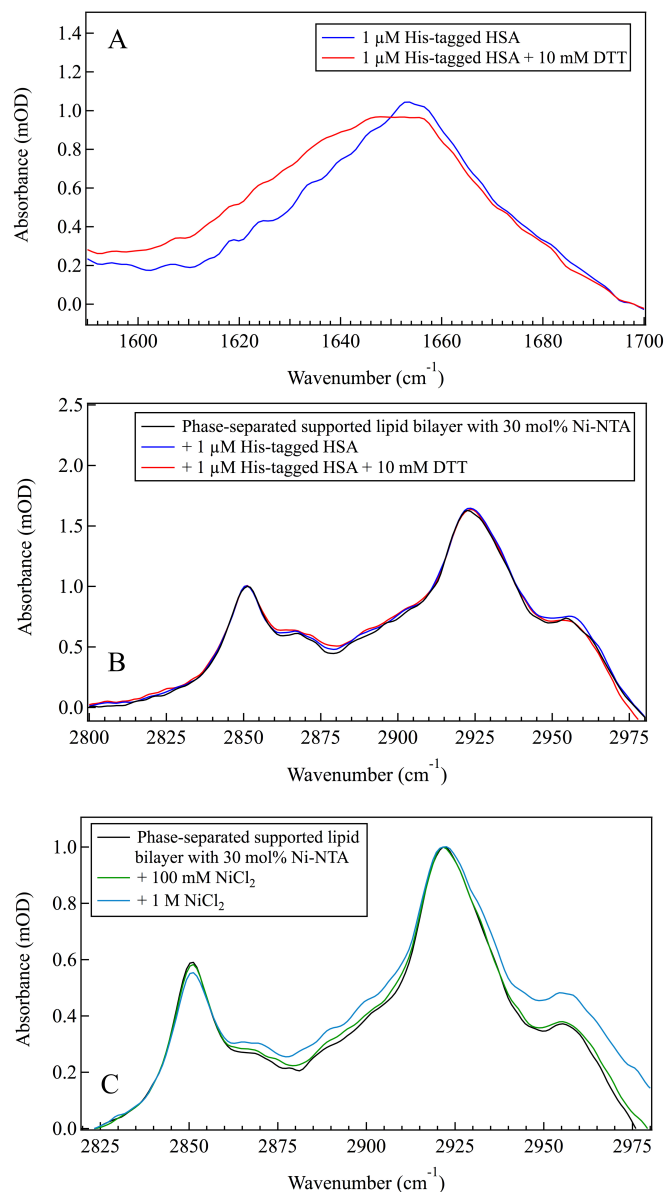
Figure S2.4 Equilibrium ATR-FTIR performed on supported lipid bilayer containing 30 mol% Ni-NTA-DGS in liquid-disordered phase. A. Equilibrium ATR-FTIR absorbance spectrum in the Amide I' region of folded (blue trace) and unfolded HSA (red trace). B. Absorbance spectrum of C-H stretching region of lipid with bound, folded HSA (blue trace) and HSA unfolded with DTT (red trace). C. Absorbance spectrum of C-H stretching region of lipid with 100 mM $NiCl_2$ (green trace) and 1 M $NiCl_2$ (blue trace).

A

| | Liposome | +10mM DTT | +1μM HSA | +1μM HSA, 10mM DTT |

NPSL 10mol% Ni-NTA

PSL 10mol% Ni-NTA

B

| | Liposome | +10mM DTT | +1μM HSA | +1μM HSA, 10mM DTT |
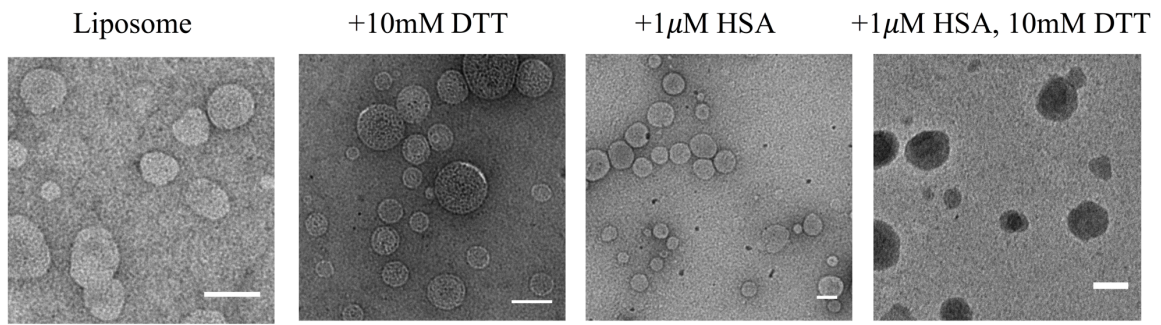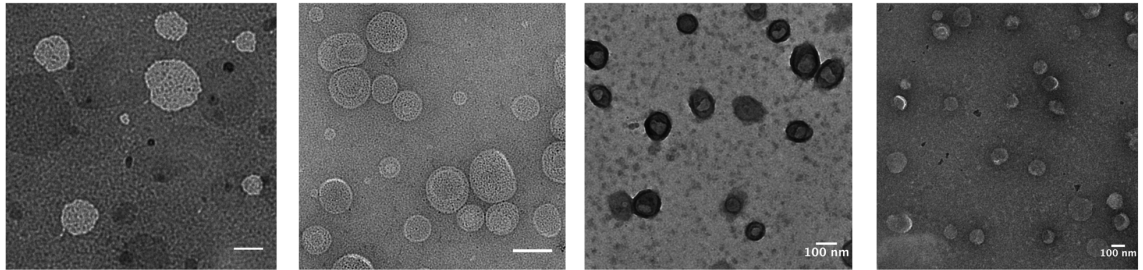
NPSL 20mol% Ni-NTA

PSL 20mol% Ni-NTA

C

| | Liposome | +10mM DTT | +1μM HSA | +1μM HSA, 10mM DTT |
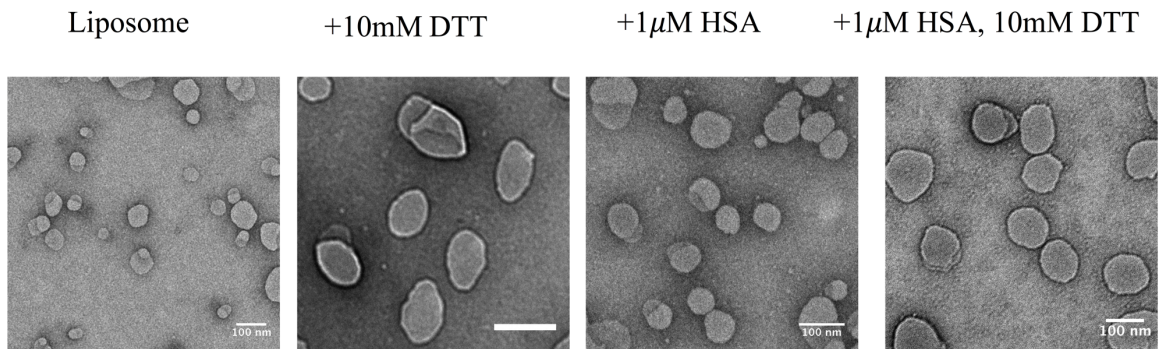
NPSL 30mol% Ni-NTA
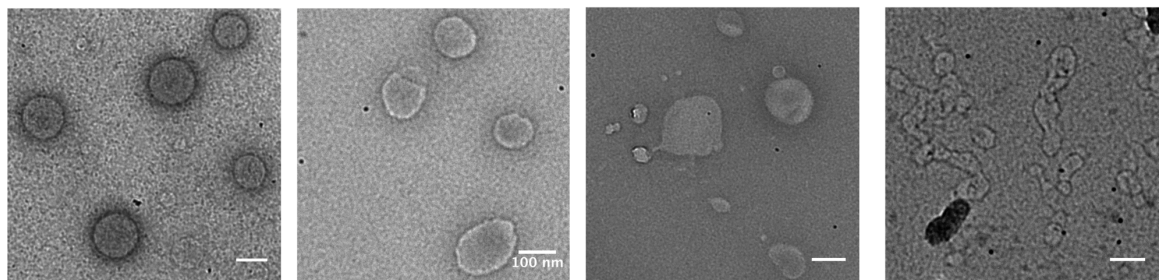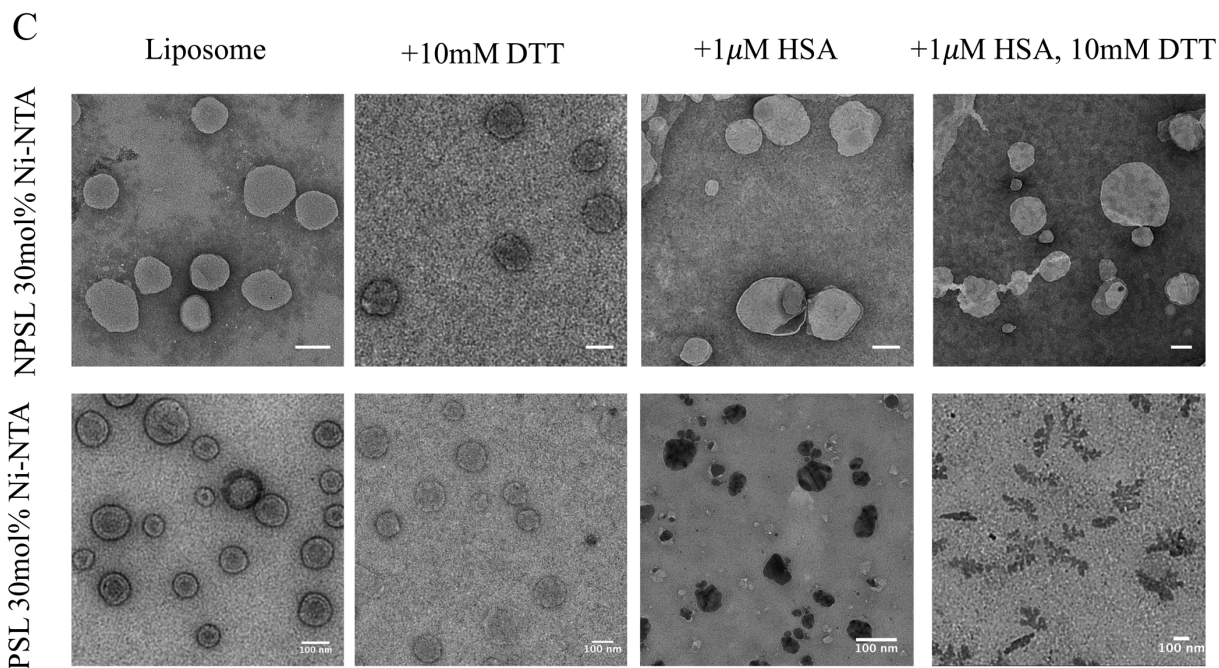
PSL 30mol% Ni-NTA

Figure S2.5 TEM images of PSL and NPSL with 10 mol%, 20 mol%, and 30 mol% of Ni-NTA-DGS in the presence of DTT, folded HSA, and unfolded HSA. A. TEM images of NPSL and PSL with 10 mol% Ni-NTA DGS show no difference in morphology. B. TEM images of NPSL and PSL doped with 20 mol% Ni-NTA C. TEM images of NPSL and PSL doped with 30 mol% Ni-NTA.
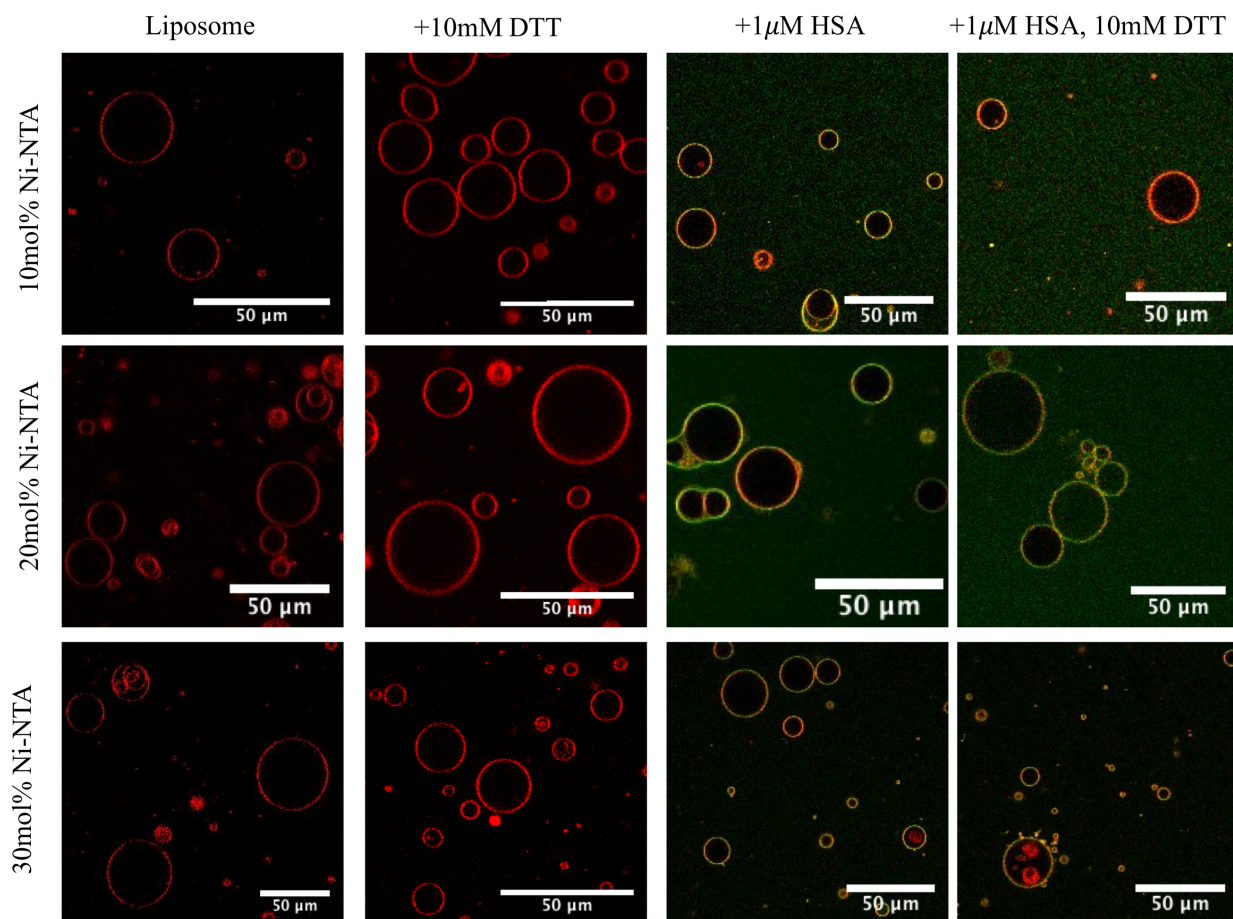
Figure S2.6 Confocal fluorescence images of NPS GUV doped with 10 mol%, 20 mol%, and 30 mol% Ni-NTA-DGS in the presence of DTT, folded HSA, and unfolded HSA. The red channel monitors the incorporation of Texas Red DHPE into the liquid- disordered phase of the lipid membrane. The green channel monitors the binding of Alexa 488 labeled His-tagged HSA to the membrane. Images of GUV with folded HSA and unfolded HSA are overlays of the corresponding red channel and green channel images. The yellow indicates regions of overlap between the two channels, interpreted as co-location of the bound protein and liquid disordered phase. Scale bar 50 μm.

10 mol% Ni-NTA PS GUV

20 mol% Ni-NTA PS GUV
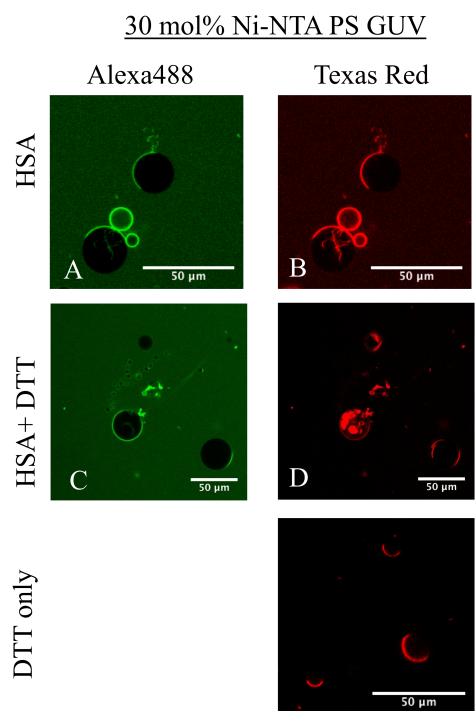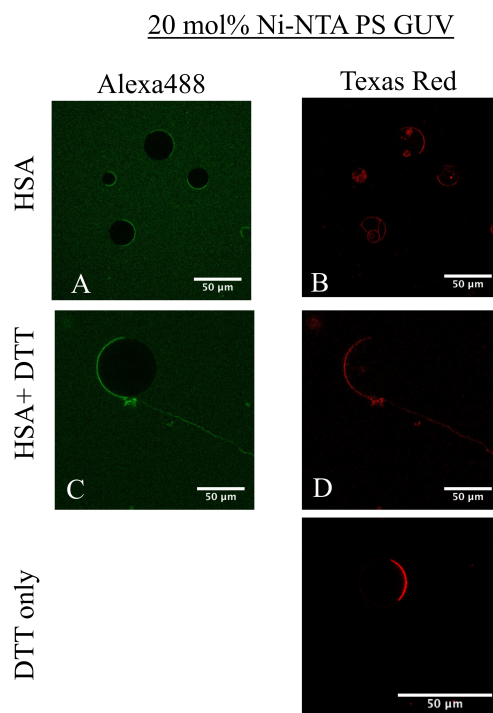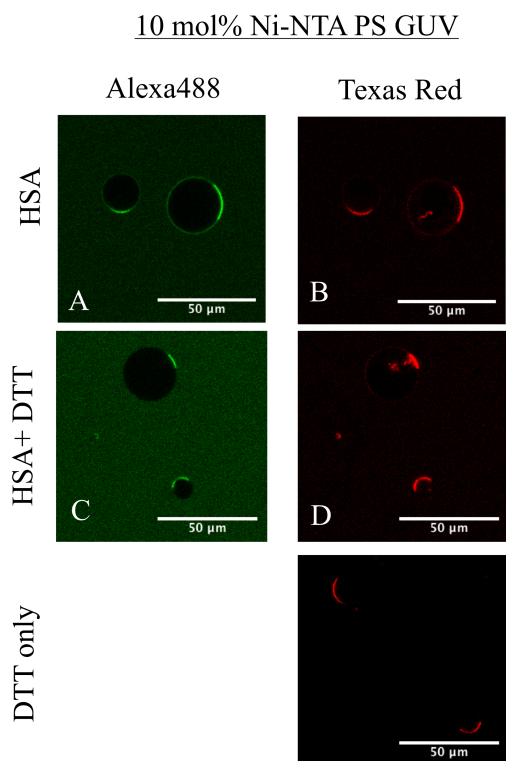
30 mol% Ni-NTA PS GUV

Figure S2.7 Confocal images of PS GUV doped with 10 mol%, 20 mol%, 30 mol% Ni-NTA-DGS in the presence of DTT, HSA, and unfolded HSA. Green channel is due to Alexa488 labeled His-tagged HSA. Red channel marks liquid disordered phase in GUV labelled with Texas Red DHPE. Scale bar 50 μm long.
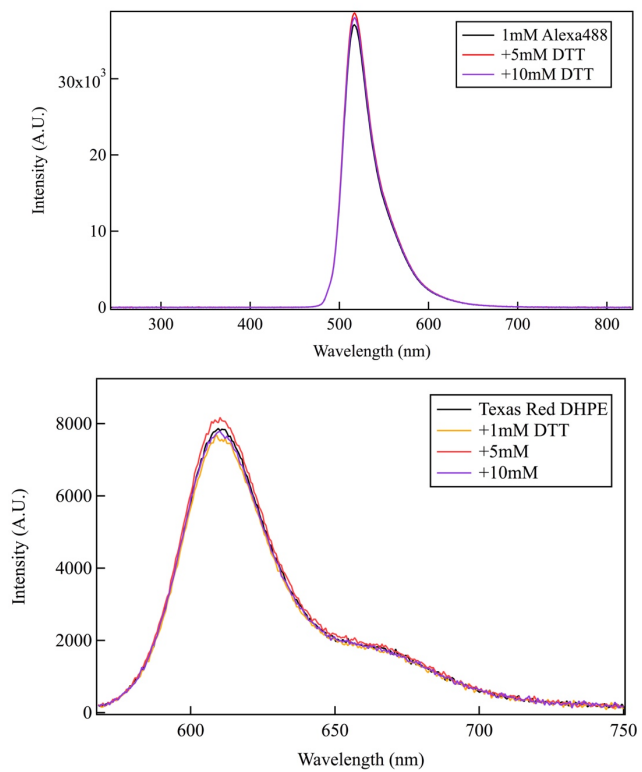
Figure S2.8 Fluorescence emission spectra of Alexa 488 and Texas Red DHPE in the presence of DTT. Spectra show no shift in emission maxima of Alexa 488 and Texas Red DHPE after incubating with various concentration of DTT. We conclude that DTT does not affect λ_{max} of either dye.

Alexa 488 Emission Calibration Curve

$y = 191863x + 2881$
$R^2 = 0.9881$
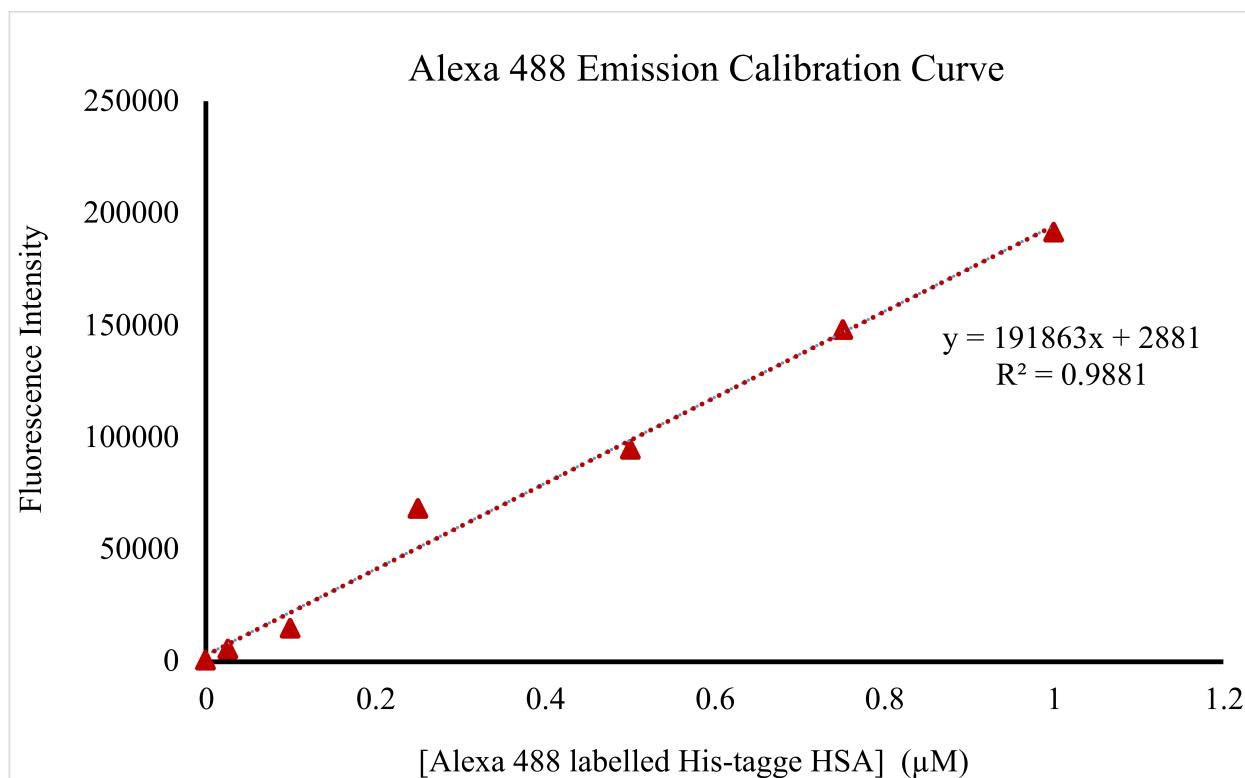
Figure S2.9 Calibration curve for quantification of His-tagged HSA bound on liposomes.

Calibration curve obtained by measuring Alexa 488 fluorescence (λ_{ex}=488nm) of labelled His-tagged HSA without any liposomes at various concentrations (0.05 to 1μM).
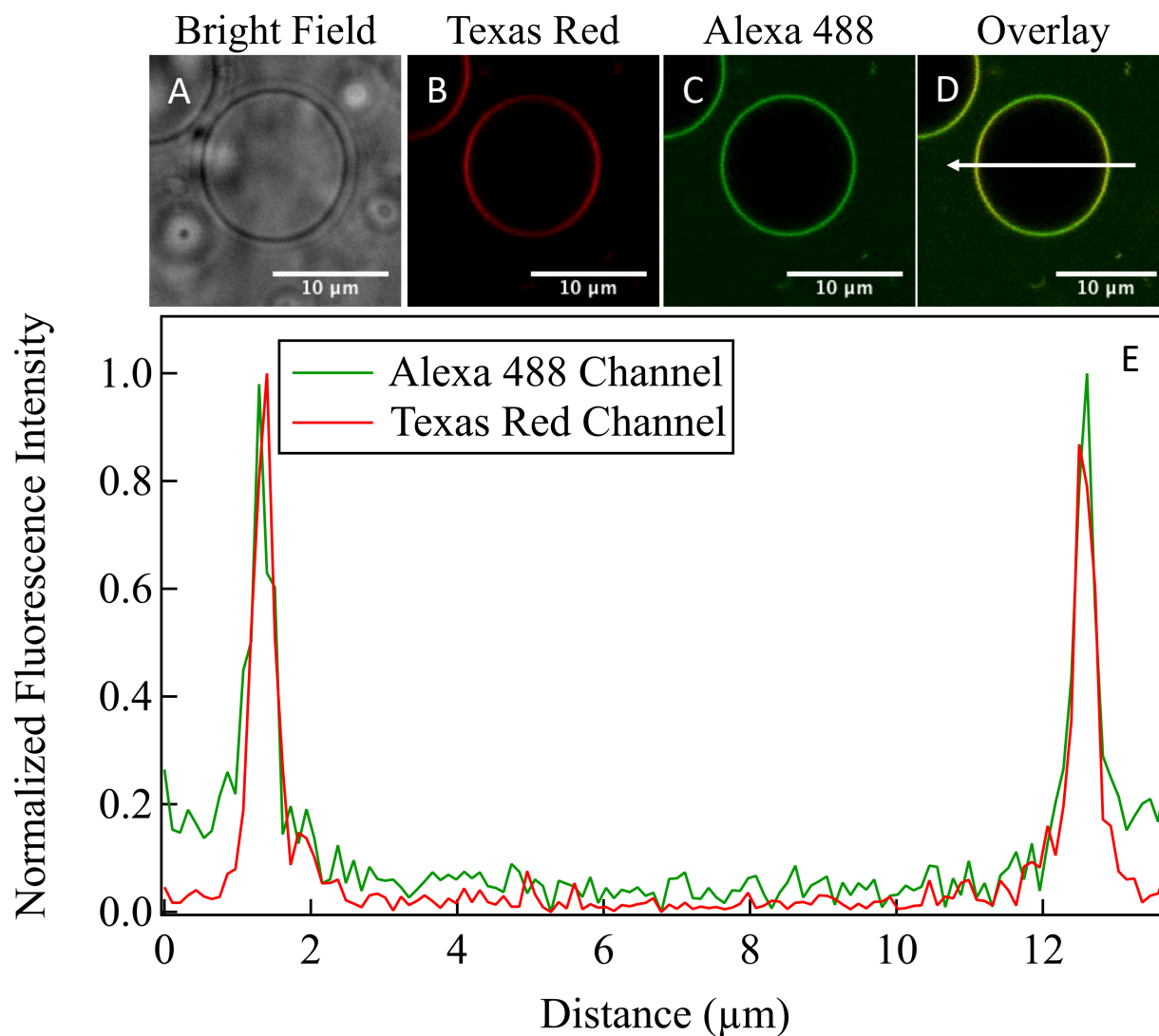
Figure S2.10 Confocal images of NPSL and corresponding intensity profile A. Confocal

imaging with bright field. B. Red channel marks liquid disordered phase in GUV labelled with Texas

Red DHPE. C. Green channel marks Alexa488 labeled His-tagged HSA. D. Overlaid image of Texas

Red and Alexa 488 channels indicates binding of HSA to liquid-disordered phase. Scale bar 10 μm.

E. Fluorescence intensity profile of the overlaid image (indicated by an arrow in the merged GUV

image).
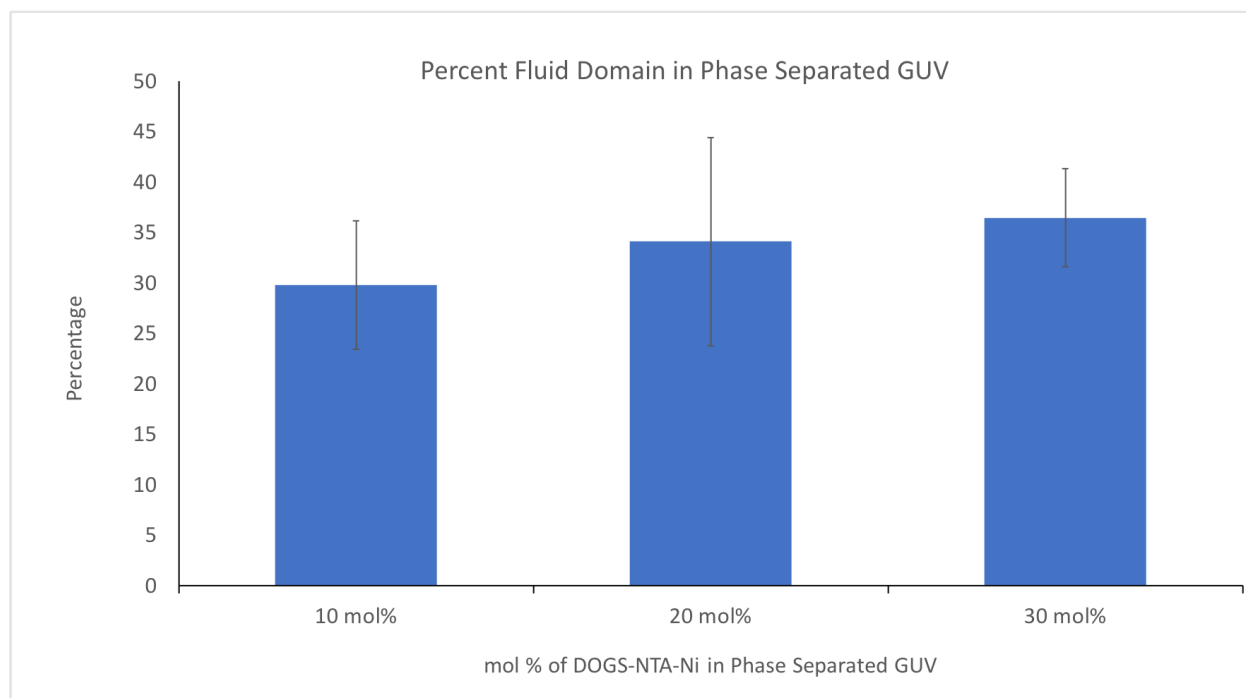
Figure S2.11 Percentage of surface area occupied by the liquid-disordered domain in phase-separated GUV containing 10 to 30 mol% Ni-NTA-DGS. About 30% of the total vesicle surface area is occupied by the liquid-disordered domain, as quantified from confocal microscopy images.

2.7.3 Supplemental Table

Table S2.1. Percent helicity of folded HSA and reductively unfolded HSA calculated

according to equation (2) and MRE at 222 nm.

	20 µM HSA	20 µM HSA + 200 mM DTT
% Helicity	55.07 ± 1.66	32.93 ± 1.87

Table S2.2. Decay Time (µs) obtained from fitting DLS autocorrelation functions to single

exponential decay model. Phase- separated liposomes (+10 mol%, 20 mol%, 30 mol% Ni-NTA-

DGS in fluid domain) with DTT, folded HSA, and unfolded HSA.

Mol% Ni-NTA-DGS	2mM PS Liposomes (µs)	+ 10mM DTT (µs)	+ 1 µM HSA (µs)	+ 1µM HSA, 10 mM DTT (µs)
10 mol%	176.60 ± 2.17E-05	172.17 ± 3.06E-05	194.51 ± 1.22E-05	197.24 ± 1.80E-05
20 mol%	140.48 ± 3.52E-05	139.68 ± 2.56E-05	160.13 ± 2.00E-05	192.58 ± 2.30E-05
30 mol%	160.40 ± 2.83E-05	160.72 ± 2.52E-05	183.42 ± 2.45E-05	200.97 ± 2.40E-05

Table S2.3 Decay Time (μs) obtained from fitting DLS autocorrelation functions to single exponential decay model. Non- phase- separated liposomes (+10 mol%, 20 mol%, 30 mol% Ni-NTA-DGS in fluid domain), with DTT, folded HSA, and unfolded HSA.

Mol% Ni-NTA-DGS	2mM NPS Liposomes (μs)	+ 10mM DTT (μs)	+ 1μM HSA (μs)	+ 1μM HSA, 10 mM DTT (μs)
10 mol%	147.03± 2.45E-05	149.21± 2.32E-05	155.52± 2.01E-05	158.46± 2.36E-05
20 mol%	131.77± 2.97E-05	131.52± 3.25E-05	137.60± 2.67E-05	139.39± 2.83E-05
30 mol%	142.14± 1.76E-05	148.84± 2.31E-05	151.58± 2.10E-05	161.55± 2.34E-05

2.7.4 Supplemental References

[1] Pande, V. S., and Rokhsar, D. S. (1999) *Proc. Natl. Acad. Sci. U.S.A. 96*, 9062-9067.

[2] Angelova, M. I., and Dimitrov, D. S. (1986) *Faraday Discus. Chem. Soc. 81*, 303.

[3] Pattanayak, R., Basak, P., Sen, S., and Bhattacharyya, M. (2017) *Biochem. Biophys. Rep. 10*, 88-93.

[4] Arsov, Z., and Quaroni, L. (2008) *Biochim. Biophys. Acta. 1778*, 880-889.

[5] Hull, M. C., Cambrea, L. R., and Hovis, J. S. (2005) *Anal. Chem. 77*, 6096-6099.

[6] Riddles, P. W., Blakeley, R. L., and Zerner, B. (1979) *Anal. Biochem. 94*, 75-81.

[7] Stachowiak, J. C., Schmid, E. M., Ryan, C. J., Ann, H. S., Sasaki, D. Y., Sherman, M. B., Geissler, P. L., Fletcher, D. A., and Hayden, C. C. (2012) *Nat. Cell. Biol. 14*, 944-949.

[8] Carnahan, N. F., and Starling, K. E. (1969) *J. Chem. Phys. 51*, 635-636.

[9] Lee, J. Y., and Hirose, M. (1992) *J. Biol. Chem. 267*, 14753-14758.

[10] Lauer, S. A., and Nolan, J. P. (2002) *Cytometry 48*, 136-145.

[11] Dorn, I. T., Pawlitschko, K., Pettinger, S. C., and Tampe, R. (1998) *Biol. Chem. 379*, 1151-1159.

[12] Nagle, J. F. (1993) *Biophys. J. 64*, 1476-1481.

[13] Nilsson, T., Lundin, C.R., Nodlund, G., Ädelroth,P., von Ballmoos, C., Brzezinski, P. (2015) *Sci. Rep. 6,* 24113.

Chapter 3:

Stability of HA2 Pre-Fusion Structure Revealed by Sub-Millisecond Conformational

Changes in the HA2 Domain of H3N2 Hemagglutinin

Siaw, H.M.H.*, Eller, M.W.*, Li, Q. and Dyer, R.B.

*Authors Siaw, H.M.H. and Eller, M.W. contributed equally

3.1 Abstract

Influenza A hemagglutinin (HA) is a homo-trimeric protein responsible for mediating viral entry. The HA1 subunit binds the host cell and triggers viral uptake. The HA2 subunit drives fusion between the viral and the host membrane via a pH-dependent conformation change in the late endosome's acidic environment. Although HA has been studied extensively, its conformational change mechanism and sequences that ultimately lead to membrane fusion remain elusive. In this study, we characterize a recombinantly expressed, truncated version of the HA2 subunit (HA2*) and demonstrate the ability to study HA's pH-driven conformational change dynamics. Our results show that the HA2* folds into a trimeric, predominantly coiled-coil structure. The HA2* also undergoes pH-driven conformation changes implying that the protein is not in a metastable state at neutral pH and would serve as an excellent model to study the pH-dependent HA dynamics. Stopped-flow fluorescence measurements reveal its folding kinetics over the sub-millisecond regime.

3.2 Introduction

Influenza hemagglutinin (HA) is a trimeric membrane glycoprotein with two distinct subunits: HA1 and HA2. The HA1 contains a receptor-binding domain responsible for attaching the virus to the host cell's sialic acid receptor and triggers endocytosis.[1] The HA2 protein consists of four parts: the endo-domain, the highly conserved stalk region, the fusion peptide (FP), and the

transmembrane domain. At neutral pH, the fusion peptide is buried within the hydrophobic pockets in the stalk region. In maturing endosomes, the acidic environment triggers large conformational changes in the HA2 protein. This prompts the insertion of FPs into the target membrane and brings the viral and host membrane into apposition for fusion.[2] Despite current knowledge of the pre-fusion and the post-fusion conformations of the HA2 protein as resolved by X-ray crystallography,[3-4] the exact mechanism that causes such conformation transition in the HA2 protein remains elusive.[2]

The spring-loaded mechanism is a hypothetical model to explain the HA2 conformation change.[5-7] This model emphasizes that the HA2 subunit is in a metastable state at neutral pH and postulates a downhill drive toward forming a coiled-coil intermediate. Specifically, the acidic pH in the maturing endosome triggers the HA1 subunit to dissociate from the HA2. Then the disordered B-loop within the HA2 folds into α-helices, resulting in an extended coiled-coil structure and insertion of FP into the target membrane. The extended coiled-coil structure then collapses on itself, and the linker leashes zip up, forming the post-fusion structure. While this model provides a framework, experimental results have been conflicting.

A series of early studies suggest that HA2 is metastable and fusion active at neutral pH. In X-ray crystallography studies, bromelain cleaved HA at neutral pH (BHA) showed pre-fusion conformation[3, 8] while bromelain cleaved HA at pH 5 (TBHA) showed post-fusion conformation.[4, 9] TBHA also exhibited increased thermostability than BHA, suggesting that HA2 is metastable at neutral pH and adopts a more stable conformation at acidic pH.[4] Further experiments studying structures of a soluble domain of the HA2 and a recombinantly expressed, full-length HA2 in *E.Coli.* at neutral pH showed that these proteins adopt post-fusion conformation, similar to the ones observed in TBHA at acidic pH.[8-9] From these observations, the authors suggest that the HA2 is fusion active at neutral pH, and acidification is not necessary to prompt the HA2 conformation

change. However, these studies did not show that there were no changes in HA2. The studies also did not examine the structural changes in the HA2 subunit with the absence of HA1.

Recent studies suggest that in the absence of the HA1 subunit, HA2 is not fusion active at neutral pH. One study examined the fusogenic activity of an HA2 construct consisting solely of the protein's soluble ectodomain (FHA2) and did not contain the HA1 subunit.[10-11] The authors reported that both lipid mixing and content mixing occurred only at acidic pH but not at neutral pH, indicating that the FHA2 caused membrane hemifusion and fusion only in acidic pH. These results clearly showed that HA2 is only fusion active upon acidification.

Understanding the HA structural transition remains key to understanding viral infection. With conflicting evidence present, it is essential to establish an HA2 model system that allows investigation into its properties without interference from the HA1 subunit. Other groups have reported the successful expression of HA2 in *E.Coli.*, characterized their oligomeric state at neutral pH, and studied the protein's ability to drive membrane fusion with fusion assay.[12-13] However, those studies did not characterize the protein's structural details during acidification, nor show that the recombinantly expressed protein could indeed undergo the pH-driven conformation change and transition from pre-fusion to post-fusion conformation.

Here, we designed, expressed, and characterized a truncated version of the HA2 subunit (HA2*). We highlighted the optimization of the expression protocol and the importance of detergent selection in HA2* expression. We then demonstrated that the HA2* folded into a trimeric coiled-coil structure at neutral pH, consistent with its pre-fusion structure. The HA2* exhibited conformational change upon acidification. Stopped-flow tryptophan fluorescence revealed sub-millisecond dynamics of this conformational change, laying the groundwork for using HA2* in studying HA2 folding dynamics. Our results suggest that HA2 is not metastable at neutral pH, and the protein undergoes pH-dependent structural transition irrespective of the presence of HA1.

3.3 Experimental Procedures

HA2* Expression and Purification

The plasmid containing the DNA sequences of H3N2 HA21–185 ectodomain with a 6x his-tag at the C-terminus (HA2*) was synthesized (Genescript). The plasmid corresponding to HA21–185 ectodomain with the disulfides at positions 109 and 113 mutated out (HA2**) was prepared at the Emory Integrated Core Facilities. The pET24a(+) plasmid was transformed into BL21 (DE3) competent cells on agar plate. After overnight growth, a single colony was transferred into LB broth with 100 μg/mL ampicillin and shook overnight at 30 °C at 200 rpm. 3.3 mL of this culture was then added to 1L LB-Kanamycin or LB-ampicillin culture media and incubated at 37 °C at 200 rpm for 5 hours. To induce protein expression, IPTG (final concentration 0.5 mM) was added, and the culture was incubated at room temperature °for 6 hours at 200 rpm. The culture was centrifuged (Beckman Coulter Avanti JXN-26) at 4°C for 10 min 5,000 g, followed by harvesting the cell pellet and storage at -80 °C. The cell pellet was lysed for 1 hour in protease inhibitor containing lysis buffer (50 mM NaH2PO4, 300 mM NaCl, 20 mM imidazole, 0.5% N-lauroylsarcosine, 0.5% Triton-X 100, pH 8) at 4 °C, followed by sonication on ice. The lysate was then centrifuged for 15 minutes at 20,000 g at 4 °C, and the supernatant was retrieved and passed through a 0.2 um filter before injecting into a his-trap FF column (GE Healthcare Life Sciences) on the FPLC (ÄKTA pure, GE Healthcare Life Sciences). The purified protein was stored at 4 °C in storage buffer (50 mM NaH2PO4, 300 mM NaCl, 0.5% N-lauroylsarcosine). The protein was used in experiments within 4 days after purification.

SDS PAGE

SDS-PAGE was used to verify the molecular weight of the expressed protein. Briefly, HA2 was first mixed with laemmli buffer in 1:1 ratio, then subject to boiling at 99 °C for 1 minute,

followed by incubation on ice for 30 minutes. The samples were loaded to 12% Mini-PROTEAN precast gels (BioRad) and run in an electrophoresis cell with SDS running buffer at 120V for 30 minutes.

Native PAGE

Native PAGE was performed to study the molecular weight of HA2 in a non-denaturing condition. HA2 was first mixed with native sample buffer (BioRad) in a 1:1 ratio and transferred to 10% Mini-Protean TGX gel (BioRad). The assay was run in Tris/Glycine buffer at 100V for 1 hour.

Size Exclusion Chromatography

SEC was performed with an FPLC (AKTA pure, GE Technologies) equipped with a size exclusion column (Sephadex 200 Increase 10/300, GE Technologies), 0.5 mL/min flow rate, and A280 detection. The column was first equilibrated with 50mM sodium phosphate buffer, pH 7, without the protein. The HA2 protein samples were first exchanged into 10 mM sodium phosphate buffer, pH 7 via dialysis with a 10kD MWCO dialysis device. The dialysis buffer was replaced each day for 3-day total dialysis time. The protein concentration was adjusted with a concentrator and then verified with the A280 absorbance using a Nanodrop 2000 spectrophotometer (ThermoFisher Scientific). The HA2 was loaded into the column at a concentration of 10 μM. A series of standard proteins comprising of vitamin B12, myoglobin, and bovine serum albumin (Sigma Aldrich) was loaded to the column to generate a calibration curve.

ELISA binding Assay

Supported lipid bilayers were prepared in 96 well glass bottom plates (Cellvis) to anchor HA2 for antibody binding assays. 2 μmol POPC and 0.5 μmol DGS-NTA(Co) were mixed in

chloroform, evaporated under a stream of nitrogen, and lyophilized. Dried lipid cakes were dissolved in 1 mL assay buffer (50 mM phosphate, 100 mM NaCl, pH 7.0). Lipid vesicles (~100 nm) were prepared by sonication of this solution until clear. Well plates were first treated with 5M NaOH (2hrs) and 1N H2SO4 (30 mins) followed by extensive wash with assay buffer. Co^{2+} doped vesicles to a final lipid concentration of 1.25 mM. The bilayers were incubated for 1 hr and washed with assay buffer. Then, HA2* (0.2 μg in 40 μL assay buffer) was added and incubated for 1 hr. The Co^{2+} headgroups were oxidized to Co^{3+} with 10 mM H_2O_2 for 15 mins, followed by incubation with assay buffer (for wells testing pH 7 conditions) or 1mM HCl (for wells testing acidic pH conditions). Before addition of antibodies, 300 μL blocking solution (5% milk in assay buffer) was added for 1hr and the wells washed 3x with assay buffer. Primary antibody (CR8020) was added as 0.4 μg in 40 μL 1% milk and incubated for 5 min, after which the wells were washed 6x with assay buffer. Secondary antibody (HRP goat anti-human) was added as 3 μg in 40 μL 1% milk and incubated for 5 min followed by a 6x wash with assay buffer, followed by HRP enzyme substrate. After 5 minutes, the reaction was stopped by the addition of 50 μL of 1 N H_2SO_4. Absorbance at 450 nm of each well was recorded using a plate reader.

Circular Dichroism

The HA2 protein samples were first exchanged into 10 mM sodium phosphate buffer, pH 7, via dialysis with a 10kD MWCO dialysis device. Dialysis buffer was replaced each day for 3-day total dialysis time. The protein concentration was adjusted with a concentrator, and then verified with the A280 absorbance using a Nanodrop 2000 spectrophotometer (ThermoFisher Scientific).

Secondary structure of HA2(6 μM) in 10mM sodium phosphate buffers of pH 4, 5, 6, 7 were acquired with a CD instrument equipped with a temperature controller (J-1500 series, JASCO). Samples were transferred to a 1 mm pathlength quartz cuvette. The scanning range of the

instrument was set between 190 and 260 nm at a rate of 200 nm/min with a 2 s response time and a

1 nm spectral bandwidth. Helical contents in HA2 were calculated using mean residue ellipticity at

222 nm:

$$MRE = \frac{\theta M}{ncl}$$……………………………….……………….……………….…………...…..(Equation 1)

where θ is the observed ellipticity (mdeg), c is the protein concentration, l is the cuvette path length,

M is the molecular weight of protein, and n is the number of peptide bonds. Percent helicity is

calculated as follows:

$$\%Helicity = \left(\frac{-MRE222nm-3000}{33000-3000}\right) \times 100$$…………………………………….………….(Equation 2)

, where MRE222nm is mean residue ellipticity at 222 nm, 3000 is the mean residue ellipticity of β-

character and random coil at 222 nm, and 33000 is the mean residue ellipticity of pure helical

character at 209 nm.

Tryptophan Fluorescence

Equilibrium tryptophan fluorescence of HA2 (6 μM) at pH 7 and pH 4, as well as

temperature-dependent spectra, were taken on a FluoroMax spectrophotometer (Horiba Scientific)

equipped with a temperature controller (Peltier, Perkin Elmer). Samples were transferred into a 1 cm

pathlength fluorescence cuvette. Data were collected using a 2 nm excitation and emission slit

widths, by exciting at 280 nm with an integration time of 10 s over a total range of 285-550 nm.

Stopped-Flow Fluorescence Spectroscopy

Protein stock in storage buffer (200 μL) was diluted to a total volume of 5 mL with

phosphate buffer, then concentrated by sequential rounds of centrifugation in a 0.5 mL centrifugal

concentrator. The final protein concentration was determined using a calculated extinction

coefficient at 280 nm of 31960 cm^{-1} M^{-1} and absorbance at 280 nm. Working solutions for

characterization and kinetics measurements were prepared from this concentrated protein

stock. Stopped flow fluorescence studies were conducted using a Biologic SFM2000 two syringe

stopped flow mixer with a microvolume cuvette. Light from a Xe lamp (HPX-2000 Mikropack) was

fiber-optically coupled to the stopped-flow mixer. The emitted light was detected at a 90° angle by

an amplified photomultiplier detector (PMM02 Thorlabs) with a DC power supply (MDC01

Tacklife). The detector output was digitized by a PCIe-6321 board (National Instruments), and data

was collected in the BIO-KINE software package (Biologic). For tryptophan fluorescence,

excitation light was filtered by a 290 nm bandpass filter and emission by a 340 nm bandpass. Syringe

1 contained 50 µM HA2** in 10 mM phosphate 100 mM NaCl at pH 7.4, whereas syringe 2

contained 19 mM HCl. The flow rate of each syringe was set to 14 mL/min and the temperature

was held at 37 °C by a circulating water bath (RTE7 Thermo). Data collection was started 20 ms

before hard stop valve closure to ensure observation of the complete mixing event. The time

resolution was 10 µs resolution for 2000 points. The background-subtracted stopped-flow traces

were smoothed using a boxcar smoothing algorithm and fit with a double exponential. (Igor Pro 5,

Wavemetrics)

3.4 Results and Discussion

Protein expression and purification

The HA2* was a construct developed according to the H3N2 hemagglutinin X-31 strain.[11]

(Fig. 1) A separate construct based on the HA2* was designed to optimize the protein yield for

stopped-flow fluorescence experiment. In the second plasmid (HA2**), cysteines at positions 109

and 113 were mutated out. Both plasmids were expressed and purified with the same method. We

investigated the effect of types of cell lines, sonication method, types of detergent, and cell lysis

GLFGAIAGFIENGWEGMIDGWYGF
RHQNSEGTGQAADLKSTQAAIDQI
NGKLNRVIEKTNEKFHQIELEFSEV
EGRIQDLEKYVEDTKIDLWSYNAEL
LVALENQHTIDLTDSEMNKLEFKTR
RQLRENEDMGNGSHKIYHKCDNA
CIESIRNGTYDHDVYRDEALNNRFQ
IKGVELKSGYKDWIVELEHHHHHH
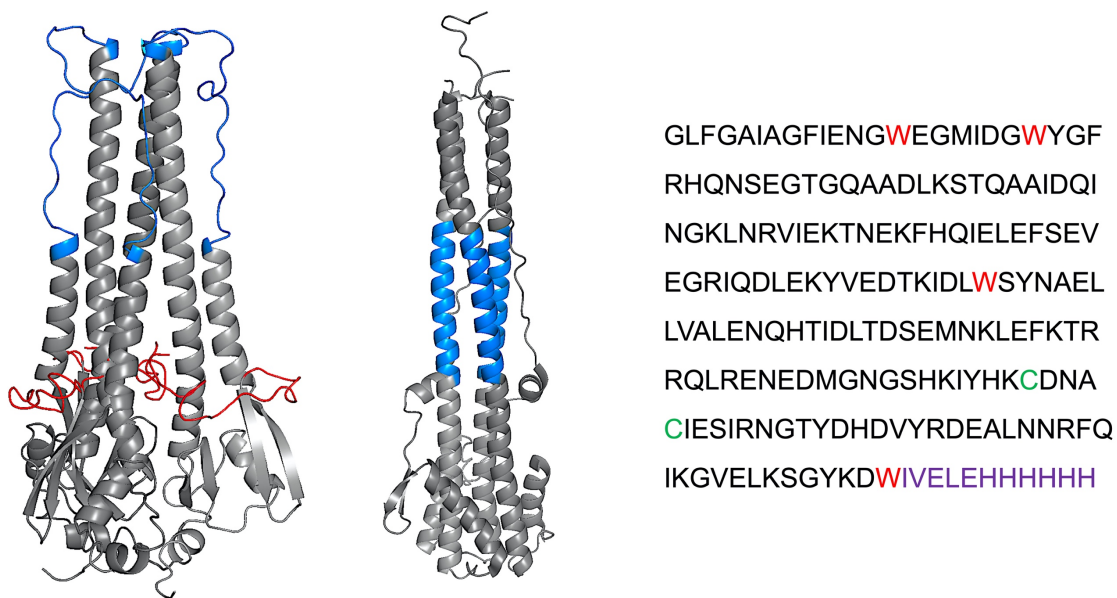
Figure 3.1 (left) Pre-fusion and post-fusion structure of HA2. The B-loop domain and fusion peptide are colored in blue and red, respectively. (right) The amino acid sequence of HA2*. There are 4 Trp residues (red) and 2 Cys residues (green). The C-terminus of the protein contains a linker and a 6x His-tag (orange). HA2** has the same amino acid sequence but with the 2 Cys removed.

 time to optimize protein yield. First, the transformation of the plasmid into BL21(DE3) competent cells produced 15% more protein than Rosetta (DE3) pLysS competent cells. Second, sonication of cell pellet in buffer with 0.5% SRC resulted in higher protein yield than in buffer without detergent. Third, purification with the anionic detergent, sarkosyl, resulted in higher protein yield than other detergents such as C8E5, n-octyl-b-d-thioglucopyranoside, and n-Dodecyl-B-D-Maltoside. Last, lysis time played a critical role in further optimizing protein yield. Increasing the lysis time from 2 hours to 2.5 hours resulted in a 25% increase in protein yield. The final optimized protein expression protocol resulted in 2.5 mg/L of HA2* and HA2**.

Using HA2* as a model to study the native folding dynamics of HA requires that the recombinantly expressed protein must be trimeric. We characterized the biochemical properties of the expressed HA2* with SDS and native PAGE, MALDI-MS, size exclusion chromatography (SEC), analytical ultracentrifugation (AUC), and enzyme-linked immunosorbent assay. The SDS PAGE characterized HA2* molecular weight in denaturing conditions. It has been reported that the molecular weight of monomeric HA2 is 26.7 kD [13], while analysis of the HA2* sequence by ExPaSy predicted molecular weight of 22.67 kD. Therefore, the distinct band observed at 25 kD on the SDS PAGE gel corresponds to HA2* monomer. **(Fig.2A)** The native PAGE described the HA2 molecular weight under non-denaturing conditions. Strong bands were observed on the gel at 25 kD, 72 kD, 95 kD, and 130 kD, while weaker bands were seen at 43 kD and between 55 kD and 75 kD. There appeared to be two components that make up the strong band at 25 kD. The band at 75 kD was attributed to trimeric HA2, while bands at 95 kD and 130 kD were attributed to higher-order oligomeric structures potentially induced by tight binding of detergent. The double bands observed at 25 kD could result from residual sarkosyl detergent being tightly bound to the HA2*. **(Fig. 2B)** Tight binding of detergent to recombinantly expressed HA2 has been observed in other studies.

In a size exclusion chromatography study, there was a significant contribution of the sarkosyl detergent (up to 175 kD) to the molecular weight of HA2. [12] UV-Vis and fluorescence studies from our lab have also shown that the detergent binds to the HA2* protein tightly, despite extended rounds of buffer exchange. (Data unpublished) SEC showed that HA2* primarily existed as a trimer at pH 7. **(Fig. 2C)** Here, a calibration curve was first generated with a calibration standard consisted of bovine serum albumin, myoglobin, and vitamin B12. **(Fig. 2D)** The HA2* was first dialyzed into 50 mM phosphate buffer at pH 7 for 3 days before injected into the column and ran under
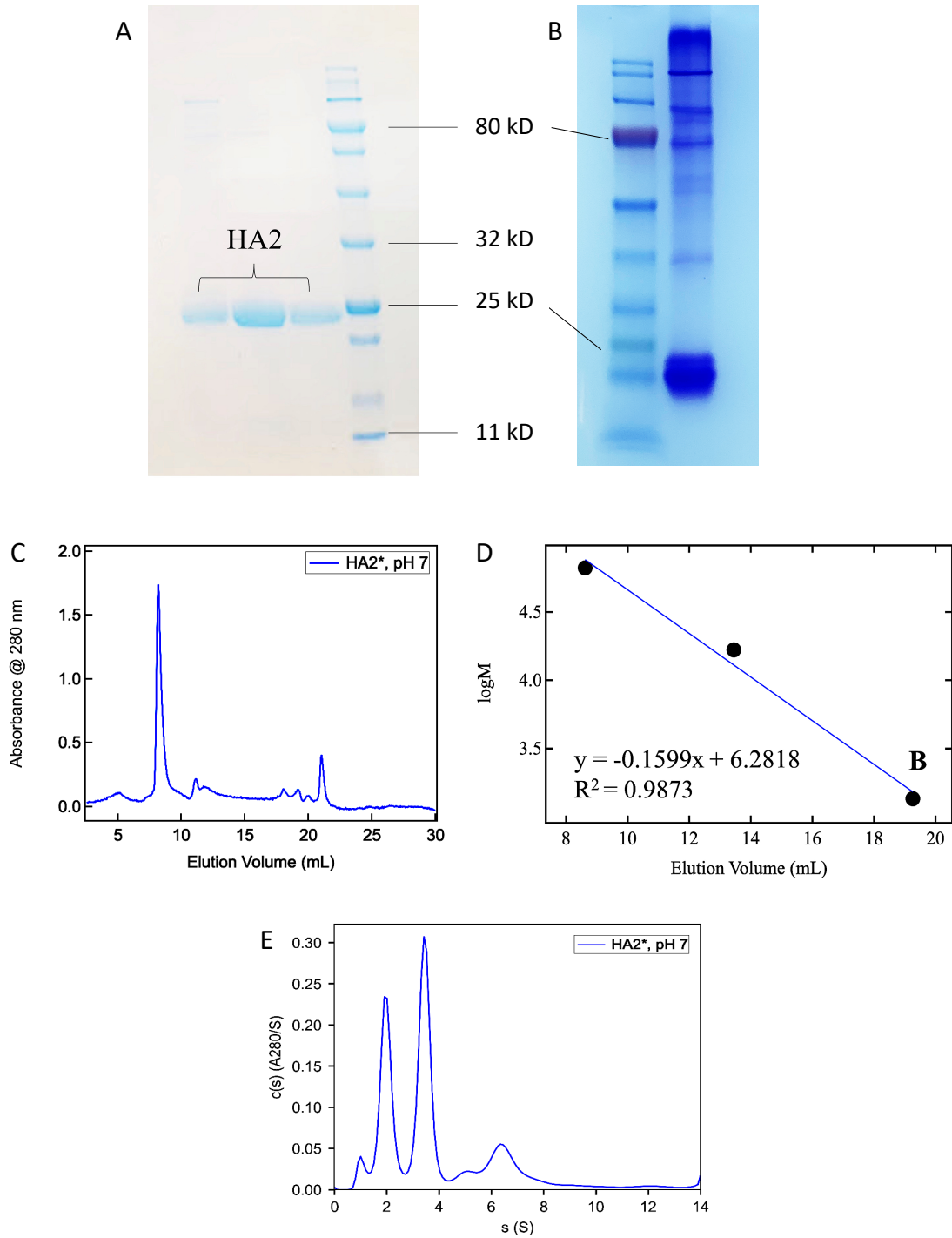
Figure 3.2 Characterization of HA2* oligomeric state. (A) SDS PAGE. (B) Native PAGE. (C) Size-exclusion chromatogram at pH 7. The peak at 8.2 mL corresponds to 93.45 kD (D) SEC calibration curve. (E) Absorbance at 280 nm from AUC showed 2 distinct peaks that correspond to 28.3 kD and 64.5 kD.

the same flow rate as the calibration standard. The chromatogram showed two dominated peaks at 8.2 mL and 21.02 mL. We calculated that the peaks corresponded to molecular weights of 93.4 kD and 0.833 kD using the calibration curve. The peak at 93.45 kD was assigned to HA2 trimer with ~ 75 kD protein and ~ 19 kD residual detergent contribution. In contrast, the peak at 0.833 kD could be a contribution from free, residual sarkosyl detergent or fragmented HA2* that was not removed during purification. The results showed that HA2* existed as a mixture of monomer and trimer, different from results reported previously in the literature. However, those studies showed that HA2 truncations formed trimeric structures by first crosslinked the proteins, followed by a size exclusion characterization. [12-13] Crosslinking might not necessarily reflect the actual oligomerization state of the protein in solution. The calibration standard consisted of mostly globular proteins and had different shapes than the HA2, which is more oblong. SEC might not truly reflect the protein's molecular weight and oligomeric states since the method separates proteins by Stokes radii. [14-15] Therefore, we sought to use AUC as a more accurate method to study the HA2* oligomeric state. [16]

The AUC reported HA2* through absorbance detection at 280 nm. HA2*showed strong absorbance at 2.03S and 3.53S, which corresponds to molecular weights 28.3 kD and 64.5 kD, respectively. **(Fig. 2E and Fig. S3.3)** This result confirmed the observation of a monomer/trimer mixture in native PAGE and SEC.

HA2 changed conformation upon acidification*

Establishing HA2* as a model system to study the HA2 pH-dependent protein folding dynamics also requires the HA2* to exhibit pH-dependent behavior while maintaining proper protein fold. Here, we characterized the secondary structure of the HA2* with spectroscopic methods, including circular dichroism (CD), fluorescence, FTIR, and ATR-IR. CD spectroscopy has

been used extensively to study protein secondary structures, including previously reported HA2 truncations.[12-13, 17] The CD spectrum of HA2* at pH 7 showed negative bands at 220 nm and 208
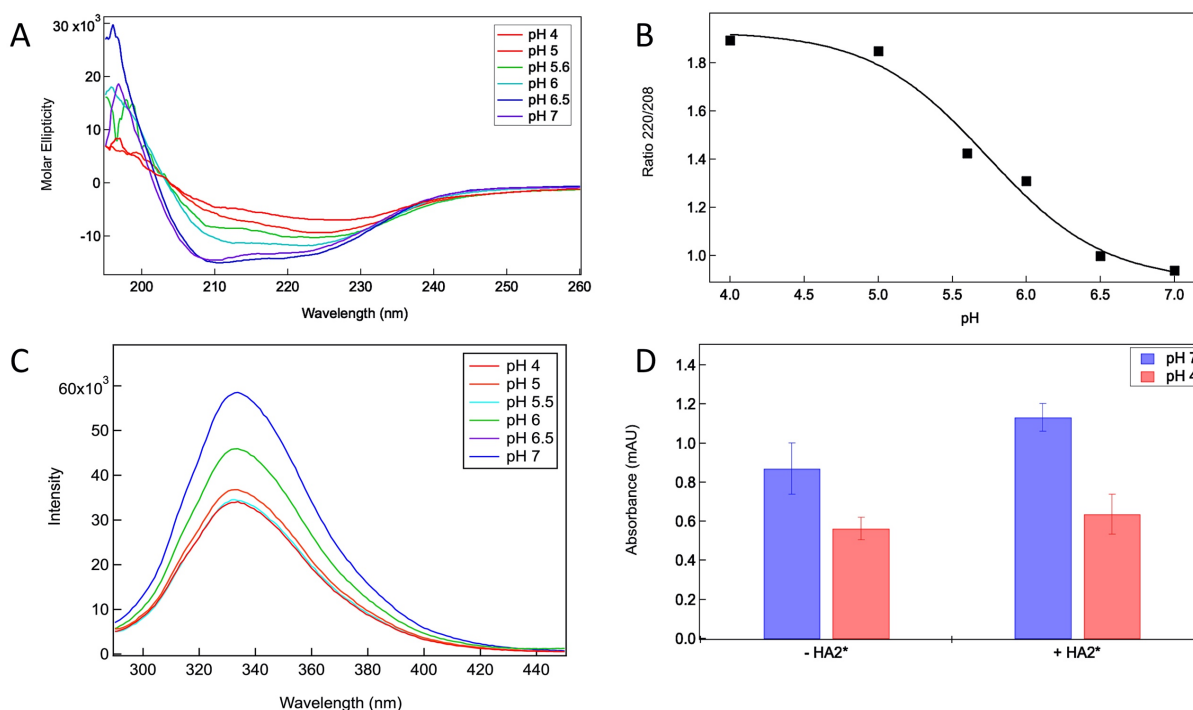
Figure 3.3 Equilibrium characterization of HA2*. (A) CD spectrum of HA2* titrated against pH gradient. (B) The ratio of 220/208 from HA2* CD spectrum. (C) Trp fluorescence of HA2* titrated against increasing acidic solution. (D) ELISA binding assay of HA2 targeting monoclonal antibody, CR8020, and HA2* at pH 7 and pH 4.

nm, with line shape characteristic to α-helical secondary structure. **(Fig. 3A)** As the HA2* solution was acidified, there was a gradual decrease in signal intensity, which could be attributed to the exposure of hydrophobic fusion peptides and subsequent protein aggregation. The acidic pH could also lead to residual anionic sarkosyl aggregation, which has been observed in UV-Vis and fluorescence. (Unpublished data) The CD signal ratio at 220 nm and 208 nm qualitatively showed whether the HA2* existed as an isolated helix or a coiled-coil structure. A 220/208 ratio greater than

1.1 may indicate a coiled-coil state. The ratio of the HA2* construct exhibited changes according to pH. The ratio increased from 0.9 at pH 7 to 1.8 at pH 4, suggesting the association of isolated helices into coiled-coil at acidic pH. **(Fig. 3B)** Fitting the pH-dependent ratio to a sigmoid showed an inflection point at pH 5.5, consistent with the estimated pH at which the native HA would undergo a conformational change.[18] Further analysis showed that the HA2* is 44% helical at pH 7 **(equation 2)**, which lies within the range of helicity reported in other studies (35% to 64%). [11-12] HA2** exhibited the same secondary structure and equivalent transition. **(Fig. S3.2B)** These results showed that HA2* and HA2** were able to undergo the expected pH-driven conformational change while maintaining its fold.

The HA2* has 4 Trp residues, which allow for monitoring the hydration environment around the residues in response to pH drop. As the HA2* was titrated against increasing acidic buffer, the tryptophan fluorescence intensity decreased, and the emission wavelength shifted minimally from 335.2 nm to 334 nm. **(Fig. 3C)** The results suggested that the hydration environment around the residues was unaffected by the acidification. Since exposed tryptophan residues fluoresced at 350 nm and buried tryptophan residues fluoresced at a shorter wavelength, the tryptophan residues of the HA2* were buried in a hydrophobic environment and were insensitive to acidification.[19] HA2** Trp fluorescence exhibited equivalent transition. **(Fig. S3.2A)** This observation was consistent with the literature, where the HA2 tryptophan fluorescence intensity decreased, and a slight blue shift in emission wavelength as the pH dropped.[19]

ELISA binding assays have been used in the literature to evaluate the proper folding of various HA constructs [20-21] and serve as an excellent tool to evaluate the fold of the HA2*. CR8020 is a broadly neutralizing antibody that binds specifically to an epitope on the stem region of HA2 of the H3N2 influenza hemagglutinin. It targets and binds the HA2 protein in its pre-fusion conformation at neutral pH and prevents the HA2 from transitioning into its post-fusion

conformation upon acidification. The HA2* was first anchored onto the supported lipid bilayer doped with Co^{2+}-NTA modified lipid via the protein's 6x-his tag. Oxidation of Co^{2+} to Co^{3+} resulted in irreversible binding with the 6x-his, thereby allowing the HA2* to bind to the surface tightly.[22] The binding of CR8020 to HA2* at neutral pH and acidic pH was followed with a colorimetric assay that utilizes the binding of a secondary antibody with horseradish peroxidase motif to the CR8020 and the HRP substrate, 3,3',5,5'-Tetramethylbenzidine. The resulting diamine oxidation product showed a yellow color and could be monitored by UV-Vis absorbance at 450 nm. At pH 7, the statistically significant higher absorbance in samples with HA2* (+ HA2*) than samples without the HA2* (- HA2*) indicated CR2080 bound to HA2* and such binding is beyond any non-specific interactions. **(Fig. 3D)** The absorbance values were not statistically different at acidic pH between samples with and without the HA2*. However, the absorbance values were statistically lower than the sample that contained HA2* at pH 7. It was clear that the CR8020 did not bind to HA2* at pH 4 but selectively bound to the protein at pH 7, suggesting that the HA2* properly folded into its pre-fusion conformation at pH 7. These results showed that at acidic pH, the HA2* underwent a pH-driven conformational change that abolished the binding of the CR8020. In conclusion, these results collectively suggested that the HA2* adopted the correct fold and could undergo a conformational transition similar to the native HA2 protein.

The recombinantly expressed HA2 is not metastable and can be used to study folding dynamics

We investigated the thermostability of the HA2* at pH 7 by subjecting the protein to gradual heating from 20°C to 80°C and monitoring its tryptophan fluorescence and CD signal intensity. **(Fig.4A and 4C)** The HA2* tryptophan fluorescence intensity decreased as temperature increased, indicating protein unfolding and exposing the tryptophan residues to an increasingly hydrophilic environment. The thermal melt curve obtained from monitoring Trp emission showed a T_m at 64.5 °C. The HA2* CD signal intensity also gradually decreased when temperature increased. These data

qualitatively indicated the HA2* was hyper-stable at pH 7, with the estimated T_m at 78.2 °C, in agreement with previously reported melting temperature. **(Fig.4D)** [8, 12]. The difference in melting temperature obtained from Trp fluorescence and CD could be due to the difference in oligomeric populations between the samples.
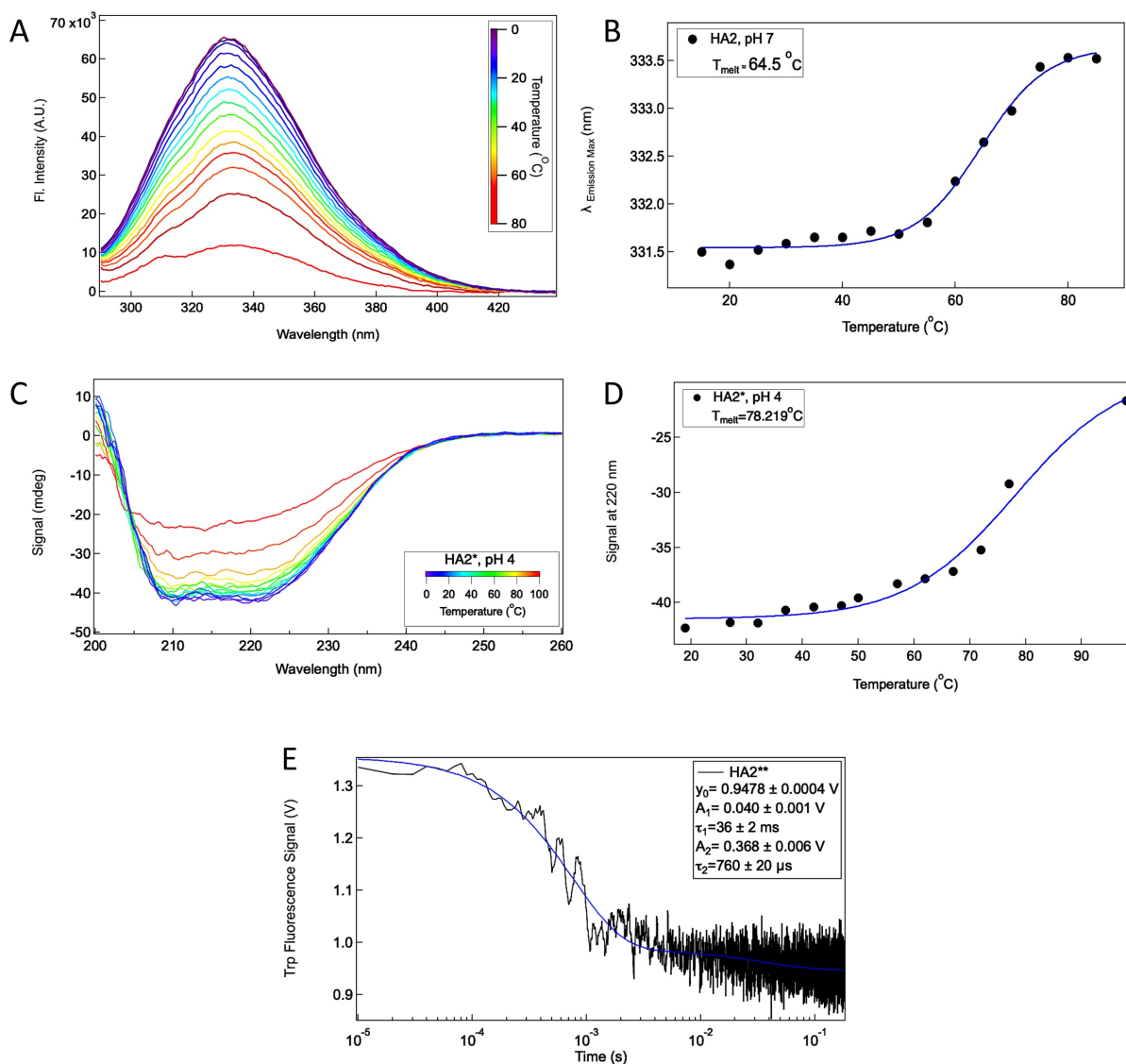

Figure 3.4 (A) Trp fluorescence melt data, from 15°C to 82°C. (B) Thermal melt curve monitoring the Trp emission wavelength. (C) CD melt data from 19°C to 95°C. (D) Thermal melt curve

monitoring CD signal at 220 nm. (E) Stopped-flow Trp fluorescence transients of HA2** showed biphasic kinetics with a fast phase at 760 μs and a slow phase at 36 ms.

Stopped-flow fluorescence spectroscopy allows for monitoring of fast dynamics within the s decrease in tryptophan fluorescence intensity of HA2** at acidic pH was used as a probe for measuring fast dynamics associated with the protein conformational changes. **Figure 4E** is a representative stopped-flow Trp fluorescence transient. The data was best fit to a double exponential and revealed two components. The fast component dominated the spectrum with a time constant of $\tau_1 = 760 \pm 20$ μs, while the contribution from the slow phase was an order of magnitude smaller with a time constant of $\tau_2 = 36 \pm 2$ ms. A previous study that used stopped-flow Trp fluorescence to study HA dynamics was limited by time resolution and deadtimes. [23] Here, we reported a biphasic kinetic behavior with a sub-millisecond time constant faster than any dynamics previously measured for HA. [23]. These results indicated that the recombinantly expressed HA2* and HA2** could be used to study fast protein folding dynamics. Applying the HA2* protein on transient time-resolved methods such as pH-jump laser spectroscopy would allow for the probing of fast-folding dynamics on the microsecond timescale and reveal intricate steps that lead to HA2 conformational change.

3.5 Conclusion

This study described a detailed characterization of HA2*, the construct corresponds to the ectodomain of the HA2 protein, with biochemical methods, equilibrium spectroscopy, and stopped-flow fluorescence spectroscopy. The HA2* was shown to exist as a monomer/trimer equilibrium at neutral pH. The HA2* also folded properly at neutral pH, with a conformation akin to the pre-fusion conformation observed in native HA and other HA2 truncations reported in the literature. This study also showed that the HA2* could undergo a pH-driven conformational change, further

establishing the feasibility of applying such construct to experiments that probe fast protein folding dynamics. Lastly, stopped-flow fluorescence served as a proof-of-concept method, showed the applicability of using the HA2* construct to study fast-folding dynamics, and revealed sub-millisecond dynamics. The extensive characterizations of the HA2* protein laid down the fundamental groundwork for applying such a system to study the HA2 conformational change.

3.6 References

1.   Skehel, J. J.; Wiley, D. C., Receptor binding and membrane fusion in virus entry: the influenza hemagglutinin. *Annu Rev Biochem* **2000,** *69*, 531-69.

2.   Boonstra, S.; Blijleven, J. S.; Roos, W. H.; Onck, P. R.; van der Giessen, E.; van Oijen, A. M., Hemagglutinin-Mediated Membrane Fusion: A Biophysical Perspective. *Annu Rev Biophys* **2018,** *47*, 153-173.

3.   Wilson, I. A.; Skehel, J. J.; Wiley, D. C., Structure of the haemagglutinin membrane glycoprotein of influenza virus at 3 A resolution. *Nature* **1981,** *289* (5796), 366-73.

4.   Bullough, P. A.; Hughson, F. M.; Skehel, J. J.; Wiley, D. C., Structure of influenza haemagglutinin at the pH of membrane fusion. *Nature* **1994,** *371* (6492), 37-43.

5.   Carr, C. M.; Kim, P. S., A spring-loaded mechanism for the conformational change of influenza hemagglutinin. *Cell* **1993,** *73* (4), 823-32.

6.   Carr, C. M.; Chaudhry, C.; Kim, P. S., Influenza hemagglutinin is spring-loaded by a metastable native conformation. *Proceedings of the National Academy of Sciences of the United States of America* **1997,** *94* (26), 14306-13.

7.   Tamm, L. K., Hypothesis: spring-loaded boomerang mechanism of influenza hemagglutinin-mediated membrane fusion. *Biochim Biophys Acta* **2003,** *1614* (1), 14-23.

8.	Chen, J.; Wharton, S. A.; Weissenhorn, W.; Calder, L. J.; Hughson, F. M.; Skehel, J. J.; Wiley, D. C., A soluble domain of the membrane-anchoring chain of influenza virus hemagglutinin (HA2) folds in Escherichia coli into the low-pH-induced conformation. *Proceedings of the National Academy of Sciences of the United States of America* **1995,** *92* (26), 12205-9.

9.	Swalley, S. E.; Baker, B. M.; Calder, L. J.; Harrison, S. C.; Skehel, J. J.; Wiley, D. C., Full-length influenza hemagglutinin HA2 refolds into the trimeric low-pH-induced conformation. *Biochemistry* **2004,** *43* (19), 5902-11.

10.	Leikina, E.; LeDuc, D. L.; Macosko, J. C.; Epand, R.; Epand, R.; Shin, Y. K.; Chernomordik, L. V., The 1-127 HA2 construct of influenza virus hemagglutinin induces cell-cell hemifusion. *Biochemistry* **2001,** *40* (28), 8378-86.

11.	Kim, C. S.; Epand, R. F.; Leikina, E.; Epand, R. M.; Chernomordik, L. V., The final conformation of the complete ectodomain of the HA2 subunit of influenza hemagglutinin can by itself drive low pH-dependent fusion. *The Journal of biological chemistry* **2011,** *286* (15), 13226-34.

12.	Ranaweera, A.; Ratnayake, P. U.; Weliky, D. P., The Stabilities of the Soluble Ectodomain and Fusion Peptide Hairpins of the Influenza Virus Hemagglutinin Subunit II Protein Are Positively Correlated with Membrane Fusion. *Biochemistry* **2018,** *57* (37), 5480-5493.

13.	Ratnayake, P. U.; Prabodha Ekanayaka, E. A.; Komanduru, S. S.; Weliky, D. P., Full-length trimeric influenza virus hemagglutinin II membrane fusion protein and shorter constructs lacking the fusion peptide or transmembrane domain: Hyperthermostability of the full-length protein and the soluble ectodomain and fusion peptide make significant contributions to fusion of membrane vesicles. *Protein Expr Purif* **2016,** *117*, 6-16.

14.	Kunji, E. R.; Harding, M.; Butler, P. J.; Akamine, P., Determination of the molecular mass and dimensions of membrane proteins by size exclusion chromatography. *Methods* **2008,** *46* (2), 62-72.

15.   Stulik, K.; Pacakova, V.; Ticha, M., Some potentialities and drawbacks of contemporary size-exclusion chromatography. *J Biochem Biophys Methods* **2003,** *56* (1-3), 1-13.

16.   Lebowitz, J.; Lewis, M. S.; Schuck, P., Modern analytical ultracentrifugation in protein science: a tutorial review. *Protein Sci* **2002,** *11* (9), 2067-79.

17.   Curtis-Fisk, J.; Spencer, R. M.; Weliky, D. P., Isotopically labeled expression in E. coli, purification, and refolding of the full ectodomain of the influenza virus membrane fusion protein. *Protein Expr Purif* **2008,** *61* (2), 212-9.

18.   Garcia, N. K.; Guttman, M.; Ebner, J. L.; Lee, K. K., Dynamic changes during acid-induced activation of influenza hemagglutinin. *Structure* **2015,** *23* (4), 665-76.

19.   Wharton, S. A.; Ruigrok, R. W.; Martin, S. R.; Skehel, J. J.; Bayley, P. M.; Weis, W.; Wiley, D. C., Conformational aspects of the acid-induced fusion mechanism of influenza virus hemagglutinin. Circular dichroism and fluorescence studies. *The Journal of biological chemistry* **1988,** *263* (9), 4474-80.

20.   Lu, Y.; Welsh, J. P.; Swartz, J. R., Production and stabilization of the trimeric influenza hemagglutinin stem domain for potentially broadly protective influenza vaccines. *Proceedings of the National Academy of Sciences of the United States of America* **2014,** *111* (1), 125-30.

21.   Rajendran, M.; Sun, W.; Comella, P.; Nachbagauer, R.; Wohlbold, T. J.; Amanat, F.; Kirkpatrick, E.; Palese, P.; Krammer, F., An immuno-assay to quantify influenza virus hemagglutinin with correctly folded stalk domains in vaccine preparations. *PloS one* **2018,** *13* (4), e0194830.

22.   Wegner, S. V.; Spatz, J. P., Cobalt(III) as a stable and inert mediator ion between NTA and His6-tagged proteins. *Angew Chem Int Ed Engl* **2013,** *52* (29), 7593-6.

23.   Krumbiegel, M.; Herrmann, A.; Blumenthal, R., Kinetics of the low pH-induced conformational changes and fusogenic activity of influenza hemagglutinin. *Biophys J* **1994,** *67* (6), 2355-60.

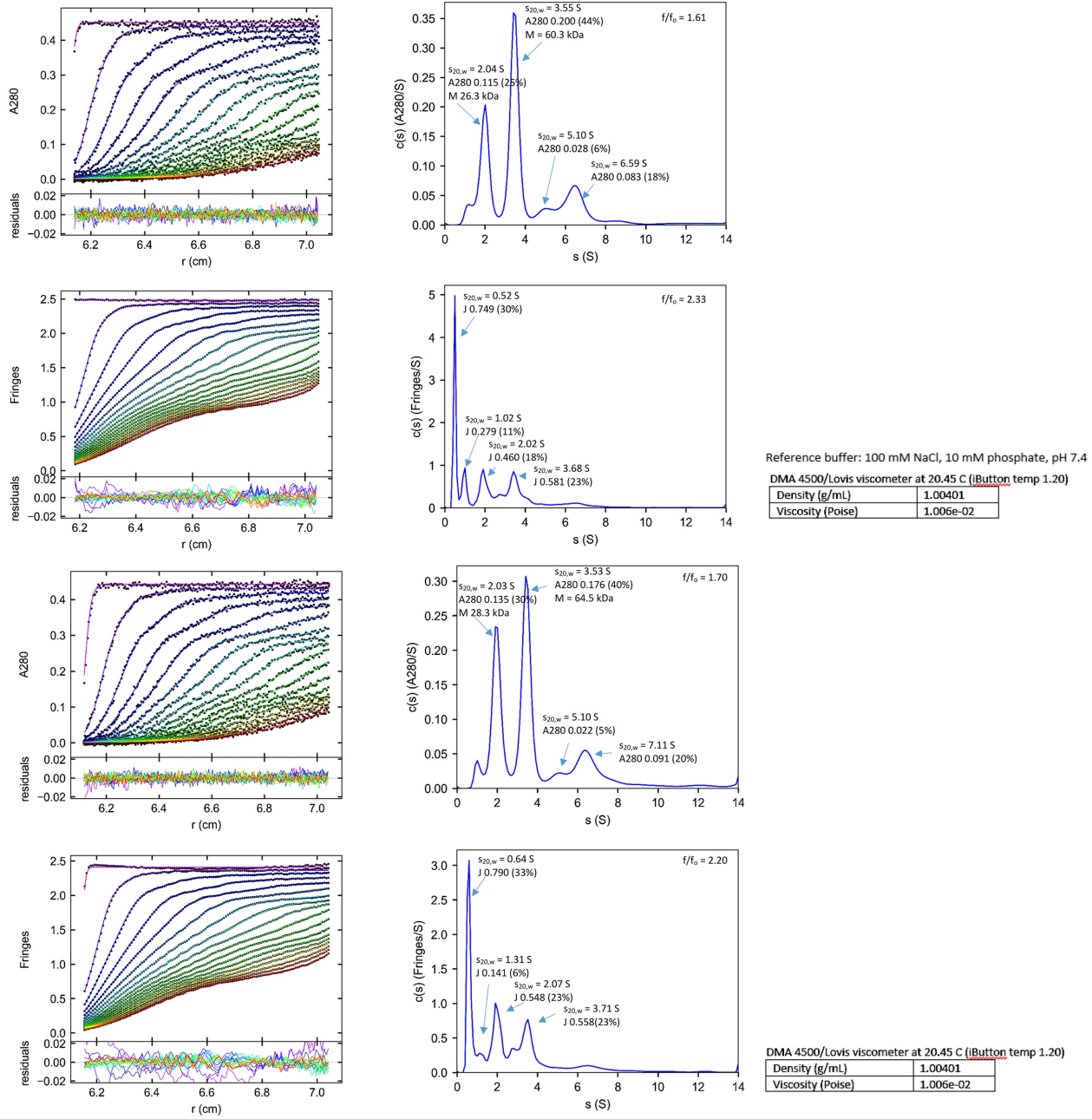## 3.7 Supplemental Information

AUC

Fig. S3.1 *Results from AUC performed on HA2* including absorbance spectra at 280 nm and interference spectra.*

Molecular weights of HA2* were indicated in the absorbance spectra.
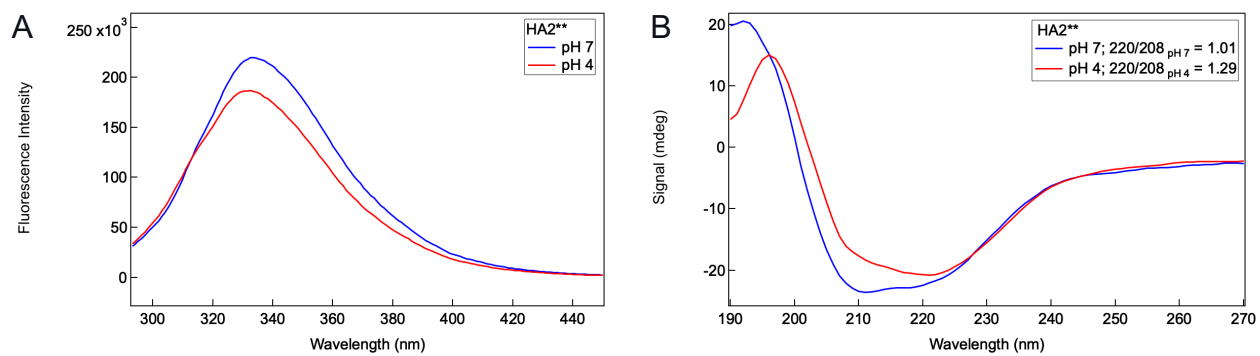
Fig. S3.2 (A) Trp fluorescence spectrum of HA2** at pH 7 and pH 4. (B) CD spectrum of HA2** at pH 7 and pH4.

<center>**Chapter 4:**</center>

<center>**pH-Dependent Liposome Crosslinking by Hemagglutinin HA2 B-Loop**</center>

<center>H.M.H. Siaw and R.B. Dyer</center>

4.1 Abstract

Upon influenza viral entry, an acidic environment in the late endosome triggers large conformation changes in viral coat protein, hemagglutinin (HA2). The transition from a pre-fusion to a post-fusion conformation facilitates the viral and the host cell membranes to fuse. It is postulated that the pH triggered folding of the B-loop domain is an essential step in forming an extended coiled-coil structure in HA2, prompting the insertion of fusion peptide into the endosomal membrane and leading to membrane fusion. This study used the B-loop domain in HA2 as a model system to study HA2 mediated membrane interactions with stopped-flow FRET Peptide corresponding to the B-loop domain (L40C) were synthesized and labeled with a donor fluorophore (sulfo-Cy3), then attached to acceptor-containing liposomes (Cy5 PE). The stopped-flow FRET resolved long timescale events likely due to liposome crosslinking due to the peptides' loop-to-coil transitions and the insertion of sulfo-Cy3 into neighboring Cy5 liposomes.

4.2 Introduction

Influenza hemagglutinin (HA) is a homo-trimeric membrane integral protein expressed throughout the flu virus. It is responsible for guiding the invasion of flu viruses into their host cells. Each monomer of the HA protein comprises a global domain (HA1) and a conserved stalk region (HA2). [1-2] The HA2 contains three essential parts: 1) a c-terminal transmembrane region which anchors the protein to the viral membrane; 2) a 40- amino acid residues B-loop domain densely populated with charged glutamic acid residues at neutral pH; 3) an N-terminus with a buried

hydrophobic fusion peptide. These three components play essential roles in facilitating later events in viral entry. Once the virus is endocytosed into the host cell, it is shuttled to the late endosome. The acidic environment drives an extensive conformation rearrangement in HA2, which leads to membrane fusion between the virus and the host cell. Early research provided a glimpse into events associated with the HA2 structural rearrangement. First, the pre-fusion and post-fusion structure of HA2 has been resolved.[3-4] Second, based on the resolved pre-fusion and post-fusion structures, it has been hypothesized that the acidic environment protonates the glutamic acid residues on the B-loop of the HA2. This then triggers the disordered B-loop to fold into alpha-helical moiety to relieve the charge repulsions. The process drives the HA2 to form a long-lived extended coiled-coil intermediate that spans across the viral and the host membrane and prompts the insertion of fusion peptide into the host cell membrane. Subsequent refolding of the C-terminal domain of HA2 then drives membrane fusion.[5-7]

Recent simulation studies present a different picture to explain the HA2 conformational change and how that process facilitates membrane fusion by overcoming the fusion barriers.[8 9-10] [2]Instead of forming an extended coiled-coil intermediate while transitioning from pre- to post-fusion, the intermediate structure involves partially folded helices and is more disordered. This flexible, disordered intermediate allows the fusion peptides on the HA trimer to simultaneously insert into both viral and host membranes.

Despite the two conflicting hypotheses, the B-loop plays a central role in both mechanisms in which its folding is essential to the HA2 conformational change and the subsequent membrane fusion. Therefore, we question whether the B-loop could serve as a model system to study HA2 mediated membrane fusion, resolved dynamics associated with the pH-driven B-loop conformation change, and followed the kinetics of liposome interactions.

To this end, we synthesized a peptide (L40C) that corresponds to the B-loop on the HA2 protein and characterized its behavior with CD spectroscopy, fluorescence spectroscopy, FTIR, and size exclusion chromatography. Then, we labeled the peptide with a donor fluorophore sulfo-Cy3 (L40C*), and covalently attached it to liposomes doped with an acceptor fluorophore Cy5. Using stopped-flow fluorescence spectroscopy and stopped-flow FRET, we followed the kinetics of L40C* conformational change and the resulting peptide association and liposome crosslinking.

4.3 Experimental Procedures

Peptide synthesis, labeling, and purification

L40C peptide:

RLIEKTNQQFELIDNEFNEVEKQIGNVINWTRDSITEVWSC was synthesized by standard Fmoc solid-phase peptide synthesis using acid-amine coupling on a Liberty 1 peptide synthesizer (CEM, Matthews, NC) using a rink-amide resin. Fmoc protected amino acids were purchased from AnaSpec, Inc. (Fremont, CA). Purifications of the L40C peptide were completed on a reverse phase C18 column (Phenomenex, Torrance, CA) with TFA as a counterion using a linear gradient of water and acetonitrile. The masses of the purified peptides were confirmed by MALDI-MS using CHCA matrix dissolved in 50:50 mixture of water: acetonitrile. MS confirmed the presence of the L40C with a mass equal to 5039 amu.

L40C peptide:*

The purified L40C peptide was labeled with sulfo-Cy3 NHS Ester (Lumiprobe, Cockeysville, MD). The sulfo-Cy3 NHS Ester was first dissolved in anhydrous DMSO then mixed with the L40 peptide in a 1:1 ratio in 10 mM sodium phosphate buffer at pH 7. The mixture was stirred at room

temperature for 2 hours. The L40C* peptide was purified on a reverse-phase C18 column. MS confirmed the presence of the L40C with a mass equal to 5637 amu.

Peptide characterization

The lyophilized L40 peptide was rehydrated with DI water to reach a final concentration of 100 μM. The peptide concentration was verified with the A280 absorbance using a Nanodrop 2000 spectrophotometer (ThermoFisher Scientific). L40 peptide was added to 10 mM phosphate buffer pH 7 or pH 4 before any measurements.

Circular Dichroism

The secondary structure of L40 in 10mM sodium phosphate buffers of pH 4 and 7 was acquired with a CD instrument equipped with a temperature controller (J-1500 series, JASCO). Samples were transferred to a 1 mm pathlength quartz cuvette. The scanning range of the instrument was set between 190 and 260 nm at a rate of 200 nm/min with a 2 s response time and a 1 nm spectral bandwidth. Molar Ellipticity were calculated:

$$MRE = \frac{\theta \cdot M}{n \cdot c \cdot l}$$ ……………………………………………………………...………………….(equation 1)

, where θ is the observed ellipticity (mdeg), c is the protein concentration, l is the cuvette path length, M is the molecular weight of protein, and n is the number of peptide bonds.

Tryptophan Fluorescence

Equilibrium tryptophan fluorescence of L40 at pH 7 and pH 4 were taken on a FluoroMax spectrophotometer (Horiba Scientific) equipped with a temperature controller (Peltier, Perkin Elmer). Samples were transferred into a 1 cm pathlength fluorescence cuvette. Data were collected using a 2 nm excitation and emission slit widths, by exciting at 280 nm with an integration time of 10 s over a total range of 285-550 nm.

Equilibrium FTIR

FTIR experiments were carried out on a Varian 660 FTIR spectrophotometer (Agilent, Santa Clara, CA) coupled to a liquid nitrogen-cooled mercury cadmium (MCT) detector. Samples were prepared in a split IR cell with a 125 µm Teflon spacer between two CaF2 windows in a copper housing. Spectra were collected for both the D2O reference and the L40C peptide sample at pD 7 and pD 4. Each spectrum was an average of 500 scans at 2 cm-1 resolution.

Size Exclusion Chromatography

SEC was performed with an FPLC (AKTA pure, GE Technologies) equipped with a size exclusion column (Sephadex 200 Increase 10/300, GE Technologies), 0.5 mL/min flow rate, and A280 detection. The column was first equilibrated with 10mM sodium phosphate buffer, pH 7 or pH 4 without the peptide. L40 was loaded into the column at a concentration of 100 µM. A series of standard proteins comprising of vitamin B12, myoglobin, and human serum albumin (Sigma Aldrich) was loaded to the column to generate a calibration curve.

Preparation of Liposomes

Liposomes contain DOPC (Avanti Polar Lipids, Alabaster, Al), 5 - 20 mol% maleimide functionalized DSPE (Nanosoftpolymers, Winston-Salem, NC), and 1 mol% of Cy5 PE (Avanti Polar Lipids, Alabaster, Al). The DOPC, maleimide functionalized DSPE, and Cy5 PE was mixed in chloroform in a glass vial and dried by N2 gas, after which the sample was placed under vacuum for at least 5 hours to ensure complete removal of solvent. The dried lipid film was rehydrated with 10 mM sodium phosphate buffer pH 7 for 1 hour, followed by 10 rounds of freeze-thaw cycles starting at room temperature and quenching to 4 °C on ice. 100 nm unilamellar vesicles were prepared by

extruding the hydrated solutions 15 times with an extrusion kit (Avanti Polar Lipids, Alabaster, Al) through 100 nm polycarbonate filters at room temperature.

Conjugation of L40C* to Liposomes

The lyophilized L40C* peptide was first rehydrated in water. A concentrated tris(2-carboxyethyl)phosphine (TCEP) solution (Sigma-Aldrich, St. Louis, MO) was prepared in 10 mM sodium phosphate buffer pH 7. The peptide and the TCEP solution were first mixed in a 1:10 ratio in 10 mM sodium phosphate buffer pH 7 and purged under N2 gas. Then, the peptide and the liposome solutions were mixed, purged with N2 gas, and stir overnight at 4 °C for reaction to complete. The peptide-liposome conjugates were applied to a 10K centricon centrifugal filter (EMD Millipore, St. Louis, MO) to remove excess peptide. The peptide liposome conjugates were then characterized by dynamic light scattering (Particulate Systems, Norcross, GA) to confirm liposome sizes after peptide conjugation.

pH-dependent steady-state FRET measurements

Steady-state FRET measurements were taken on a FluoroMax spectrophotometer. The L40C*-liposome conjugates mixed with 100 mM sodium phosphate buffer or 100 mM acetate buffer from pH 7 to pH 4 were transferred into a 1 cm pathlength fluorescence cuvette. Data were collected using a 2 nm excitation and emission slit widths, by exciting at 500 nm with an integration time of 10 s. FRET efficiency was calculated by:

$$FRET\ Efficiency = \frac{I_{Cy5}}{I_{sulfo-Cy3} + I_{Cy5}} \quad \dots\dots\dots\dots\dots\dots\dots\dots\dots\dots\dots\dots\dots\dots\text{(equation 2)}$$

, where I_{Cy5} is the Cy5 emission intensity at 694 nm, and sulfo-Cy3 is the sulfo-Cy3 emission intensity at 563 nm.

Stopped-flow experiments were performed with a Biologic 2000 stopped-flow mixing instrument (Biologic, Knoxville, TE) coupled to an HPX-2000 Xe light source and a photomultiplier tube (PMT) detector (Thor Labs, Newton, NJ).A 520/35 single-band bandpass filter (Semrock, Rochester, NY) was placed in front of the Xe light source to excite sulfo-Cy3 selectively. For detecting sulfo-Cy3 and Cy5 emission, a 560/10 bandpass filter (Omega, Austin, TX) and a 650 long-pass filter (Omega, Austin, TX) were placed in front of the PMT detector, respectively. The sample cell of the stopped-flow instrument was filled with content injected from syringe 1 and syringe 2, where syringe 1 contains either 10 mM phosphate buffer pH 7 or the L40C*-Liposome samples, and syringe 2 contains 100 mM sodium acetate buffer pH 4. Stopped-flow traces were collected for both the buffer background and L40C*-liposome sample at a 16 mL/min flow rate, with contents in syringe 1 and syringe 2 mixed in a 1:1 ratio. Stopped-flow traces were fit to single-exponential function or a double-exponential function: [11] [12]

$$F(t) = y_0 + Ae^{(-k_{obs} \cdot t)} \dots\dots\dots\dots\dots\dots\dots\dots\dots\dots\dots\dots\dots\dots\dots\dots\dots\dots\text{(equation 3)}$$

$$Tau = \frac{1}{k_{obs}} \dots\dots\dots\dots\dots\dots\dots\dots\dots\dots\dots\dots\dots\dots\dots\dots\dots\dots\dots\dots\dots\text{(equation 4)}$$

$$F(t) = y_0 + A_1 e^{(-k_{obs,1} \cdot t)} + A_2 e^{(-k_{obs,2} \cdot t)} \dots\dots\dots\dots\dots\dots\dots\dots\dots\dots\dots\text{(equation5)}$$

, where F(t) is the fluorescence at time t, A is the amplitude, k_{obs} is the observed rate constant, and tau is the time constant.

4.3 Results and Discussion

Design and equilibrium characterization of L40C peptide

The L40C peptide corresponds to the 40 amino acid residues in the B-loop region of the HA2 protein, with a cysteine residue added to C-terminus for liposome conjugation. L40C consists

of a loop region at the N-terminus and five helical turns at the C-terminus. The post-fusion crystal structure of HA2 showed the loop-to-helix folding on the B-Loop. Therefore, we expected that the L40C peptide folds into an alpha helix and form extended coiled-coil at low pH. **(Fig.1A) Figure S4.1A** showed the mass spectrum of the L40C peptide after synthesis and purification. Using circular dichroism (CD), FTIR and tryptophan fluorescence, we showed that the peptide underwent loop to helix transition upon acidification.
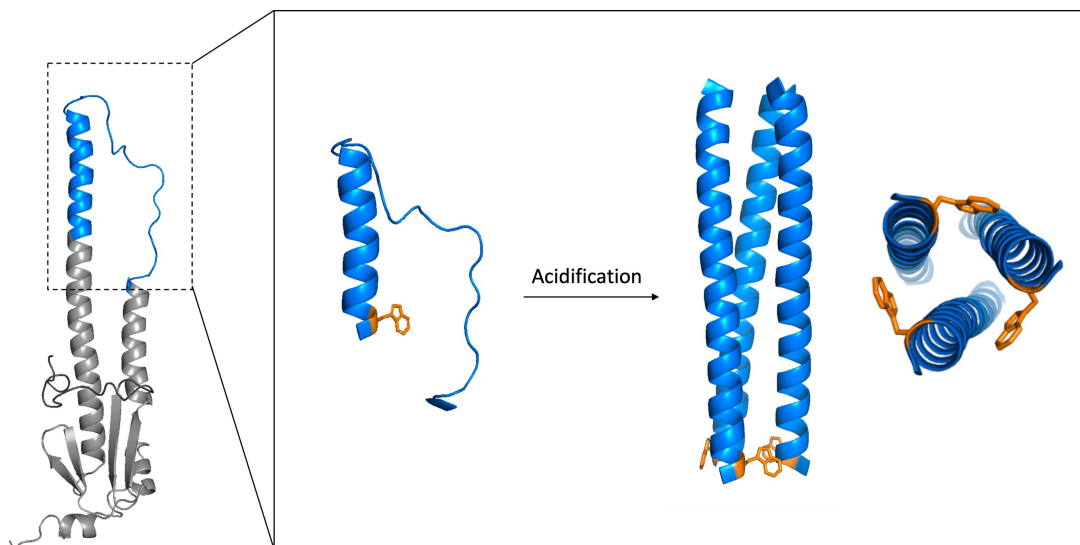
Figure 4.1 Crystal structure of HA2 at pH 7 (PDB: 1HMQ). The L40C peptide corresponds to the B-loop on the HA2 (blue). Upon acidification, the monomeric peptide folded into a trimeric coiled-coil (PDB: 1QU1). Tryptophan residues (orange) are located at the C-terminus of the peptide.

CD measures the peptide's secondary structure. It showed that at pH 7 the peptide adopted a mix of a random coil and an alpha-helical conformation. At pH4, the peptide folded and presented an alpha-helical signal in the CD spectrum, consistent with the previously resolved crystal structure. **(Fig. 2A)** The n - π * ratio at 220 nm to π - π * at 208nm has been previously used to characterize helical oligomers. The ratio qualitatively indicates the presence of helical oligomers at values greater

than 0.86. [13] [14] The 220/208 ratio of B-loop at pH 4 is greater than 1, consistent with a coiled-coil formation upon acidification. The CD signal at 222 nm for L40C showed a cooperative, thermal-unfolding transition at pH 4 with T_{melt} = 53.9°C. No transition was seen at pH 7, suggesting that the peptide exists predominantly as a monomer at pH 7 and as a trimeric, extended coiled-coil at pH 4. **(Fig. 2B)**
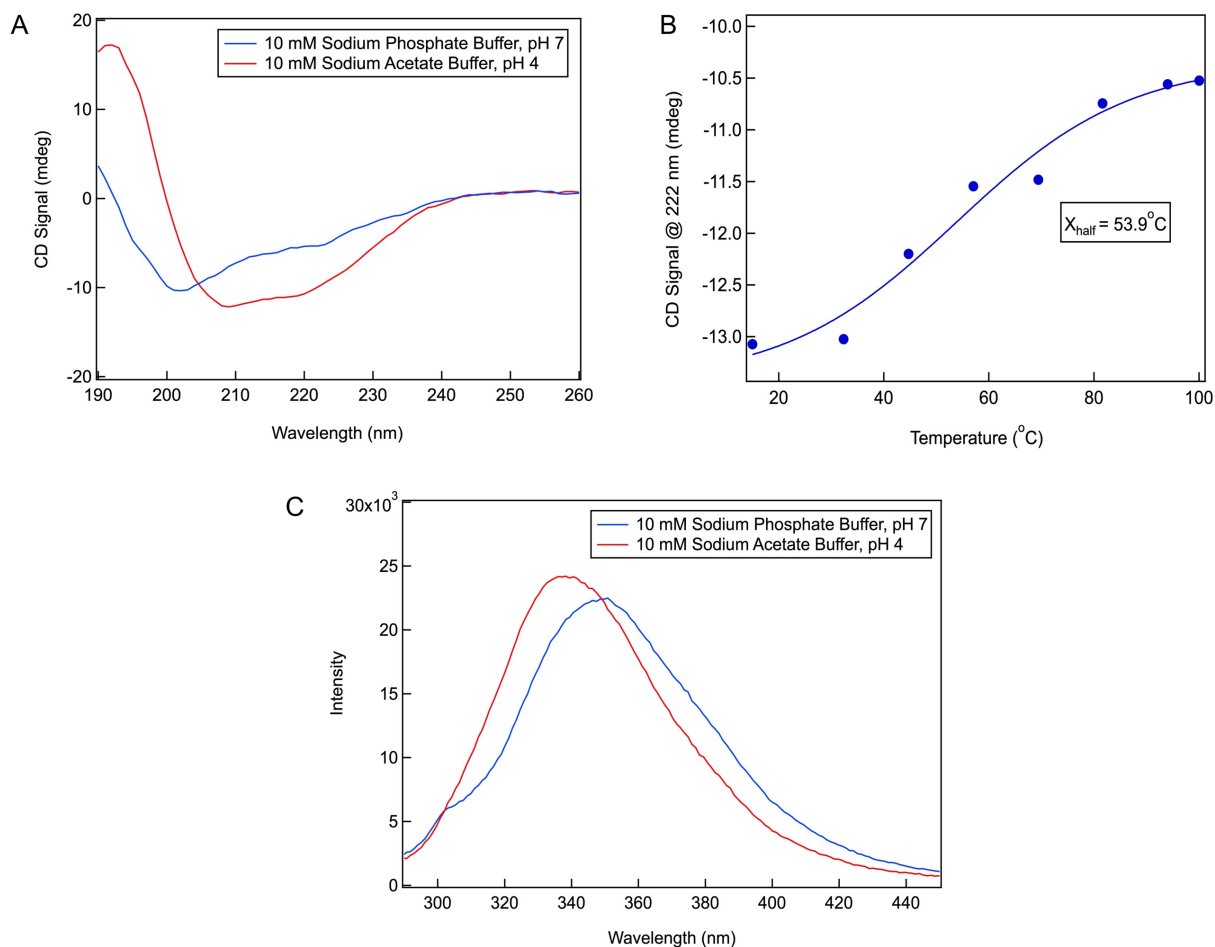

Figure 4.2 (A) CD spectra of L40C at pH 7 and pH 4. (B) Temperature melt curve of L40C at pH 4. (C) Trp fluorescence of L40C at pH 7 and pH 4.

The fluorescence of intrinsic tryptophan (trp) residues at the C-terminus of the peptide **(Fig. 2C)** reports the hydration environment around the residues. At pH 4, a blue shift in tryptophan

emission wavelength and an increase in fluorescence intensity of the peptide indicated the

tryptophan residues were buried in a more hydrophobic environment and that the helices were more

tightly packed in an acidic environment. **(Fig. 1 and Fig. 2C)** The C-terminal cysteine residue did

not alter the structure and the pH-dependent response of the peptide. **(Fig. S4.2)**
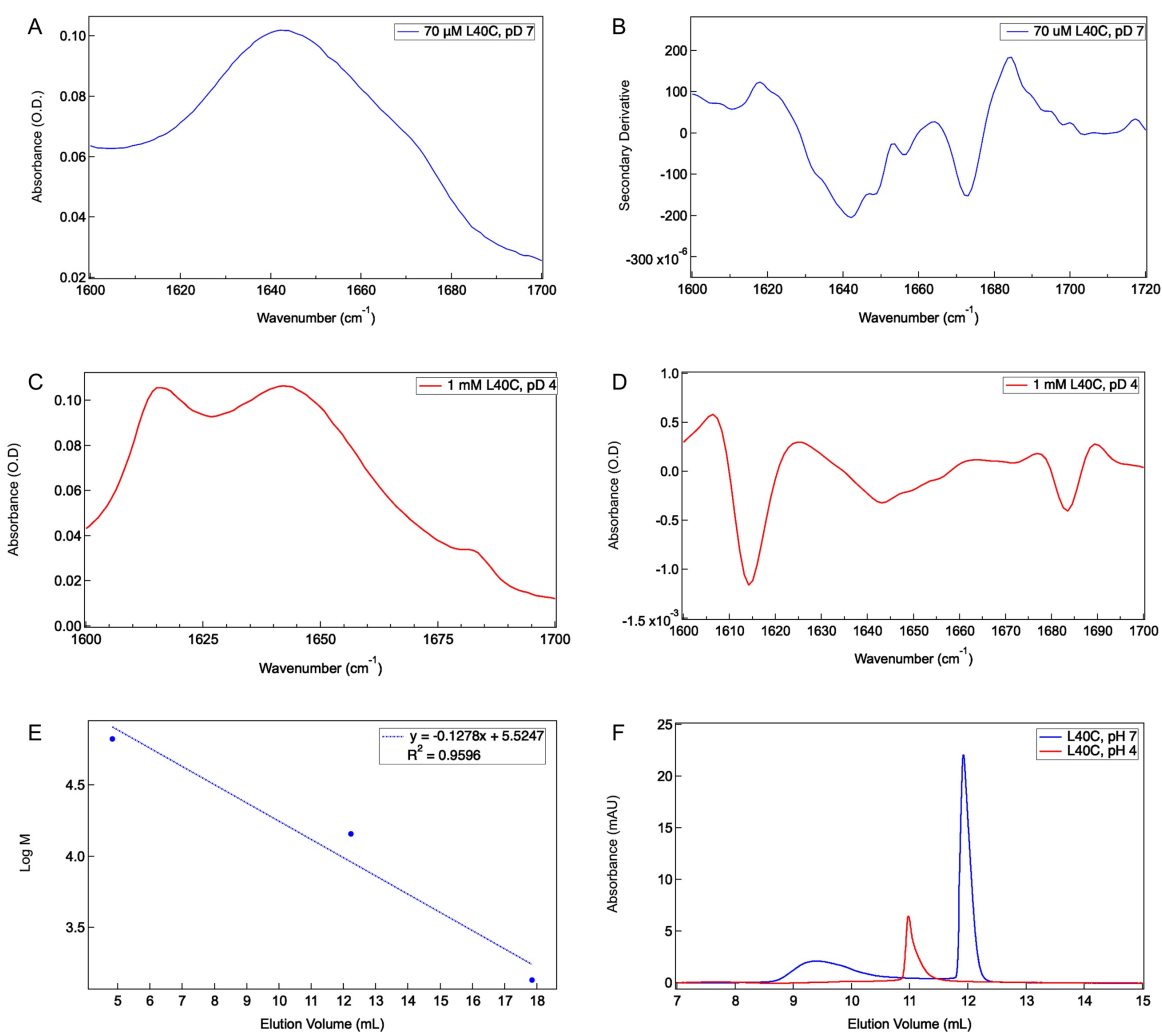
Figure 4.3 (A) FTIR absorbance spectrum of L40C at pD 7. (B) FTIR secondary derivative spectrum

of L40C at pD 7. (C) FTIR absorbance spectrum of L40C at pD 4. B) FTIR secondary derivative

spectrum of L40C at pD 4. (E) The calibration curve of size exclusion chromatography was obtained

by injecting a mix of human serum albumin (66 kD), myoglobin (17 kD), and vitamin B12 (1.35 kD).

(F) Size exclusion chromatogram of L40C at pH 7 (blue) and pH4 (red).

Figure 3A shows the FTIR absorbance spectrum of L40C at pD 7. The spectrum was processed to obtain a secondary derivative spectrum to resolve features observed in the absorbance spectrum. **(Fig. 3B)** At pD 7, a sharp negative feature at 1645 cm^{-1} represents buried helix (backbone positions in the solvent-protected, hydrophobic interior of the structure), and a negative shoulder at 1630 cm^{-1} represents solvated helix (backbone positions along each helix that are exposed to solvent). [15-16] A characteristic for coiled-coil structures, these features preliminarily indicate the formation of a helical base on the peptide at neutral pH. The negative peak at 1675 cm^{-1} represents an extended loop structure, in agreement with the secondary structure reported by CD. At pD 4, the L40C peptide showed negative features at 1614 cm^{-1} and 1681 cm^{-1}, which corresponds to the anti-parallel beta-sheet,[17] whereas the peak at 1645 cm^{-1} represents buried helix. Results from FTIR differed from CD in which CD resolved strong signal indicating alpha-helical moiety, whereas FTIR presented a mix of beta-sheet and buried helix. Peptides rich in glutamic acids are favored to form coiled-coil and prone to aggregation and forming beta-sheet aggregates. [18-20] L40C contains 6 glutamic acid residues. It could be possible that the high concentration of peptides used in the FTIR experiment favored the L40C coiled-coil to form aggregates, while the low peptide concentration in CD experiments avoided such a problem.

In addition to spectroscopic characterization, oligomeric states of the peptide at neutral and acidic pH were studied with size-exclusion chromatography. A calibration curve was first generated using a mixture of globular proteins, human serum albumin (66 kD) and myoglobin (17 kD), and vitamin B12 (1.35 kD). **(Fig. 3E)** At pH 7, the peptide eluted at 9.4 mL and 11.92 mL, whereas at pH 4 the peptide eluted at 10.9 mL. Fitting these volumes to the calibration curve revealed that the peptide existed as a mixture of monomer and oligomer at pH 7 and a trimer at pH 4. **(Fig. 3F)** These results suggested the monomeric L40C folded into a trimeric structure at low pH.

Labeling of L40C* peptide and liposome conjugation

For L40C to serve as a proxy to probe membrane fusion, we labeled the N-terminus of the L40Cy3 peptide with a sulfo-Cy3 NHS ester to provide a spectroscopic handle. The labeled peptide will be referred to as L40C*. Sulfo-Cy3 has been shown to have little interaction with the lipid membrane. [21] The labeling of L40C* was confirmed with MALDI and UV-Vis.

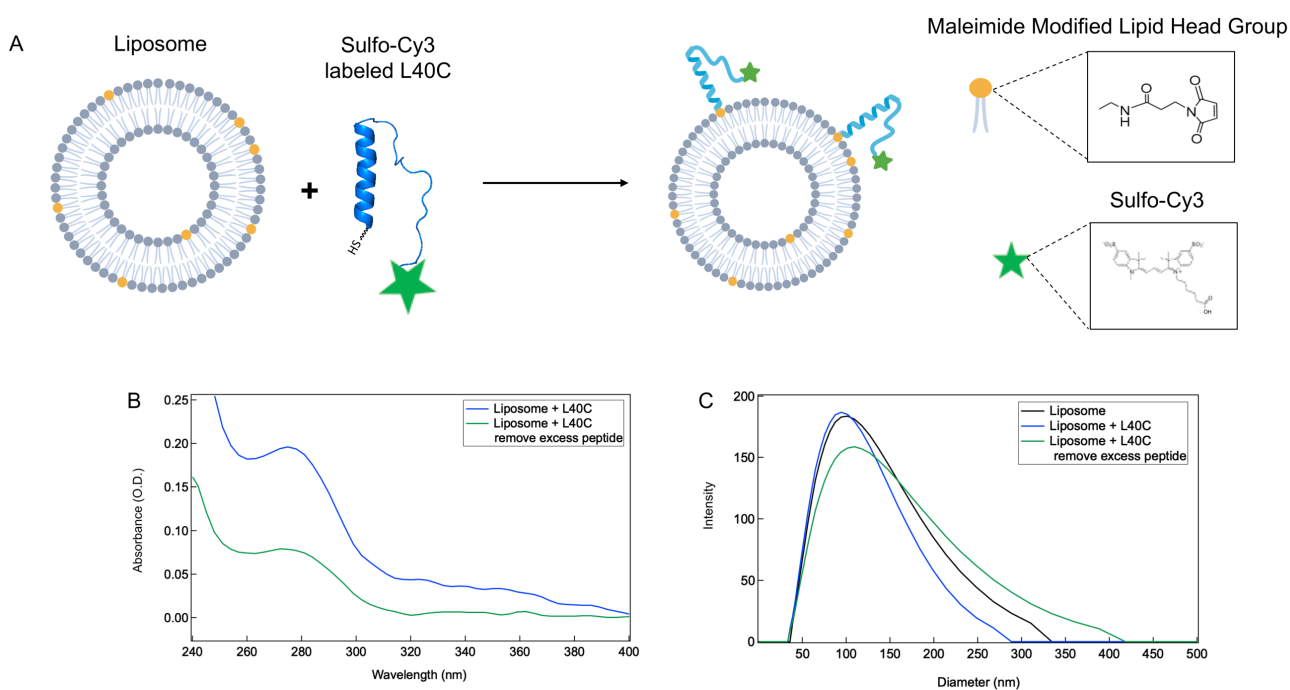**Figure 4.4**. (A) Schematic showing the attachment of the L40C* peptide to DOPC liposomes via the maleimide-modified lipid. (B) UV-Vis of DOPC liposomes conjugated to L40C*, before and after removing excess peptide with a 10K MWCO centrifugal filter. (C) Dynamic light scattering reported the size distribution of the DOPC before (black) and after L40C* peptide conjugation (blue) and removal of any unbound L40C* (green).

We synthesized DOPC liposomes doped with maleimide functionalized lipid and then conjugated the L40C* via the peptide's C-terminal cysteine residue in a 1:1 ratio. **(Fig. 4A)** Using dynamic light scattering and measuring the sulfo-Cy3 fluorescence, the sizes of peptide-liposome conjugates and peptide attachment efficiency was measured. **(Fig. S4.3)** The hydrodynamic radii of DOPC liposomes increased slightly from 92.9 nm to 106.8 nm, which showed that peptide attachment did not cause catastrophic liposome aggregation. **(Fig. 4C)** UV-Vis at 280 nm showed that spinning samples with a 10K MWCO centrifugal filter successfully removed the excess, unbound peptide. **(Fig. 4B)**

Membrane fusion activity mediated by L40C*

Using FRET, we investigated the impact of the pH-driven conformational change of L40C* on the lipid membrane. The DOPC maleimide liposomes were doped with Cy5 PE, and then the L40C* was attached. Cy5 acts as a FRET acceptor to the sulfo-Cy3 donor fluorophore on the L40C*. The FRET efficiency was minimal at pH 7 and exhibited a sudden increase at pH 4.5, indicating proximity and optimal energy transfer between Cy5 and sulfo-Cy3. **(Fig. 5A)** The FRET efficiency was fit to a sigmoid with X_{half} at pH 4.59. **(Fig. 5B)** Dynamic light scattering showed a significant increase in hydrodynamic radii of L40C* liposome conjugates as the acidity of the solution reached pH 4.5, suggesting liposome aggregation at acidic pH. **(Fig. 5C)** L40C* alone showed pH-dependence. The emission intensity of sulfo-Cy3 on the peptide decreased as pH dropped. **(Fig. 5D)** This pH-dependence was fit to a sigmoid with X_{half} at pH 5.5. **(Fig. 5E)** [22] [23] It has been reported that the pH range that activates HA is between pH 5.5 to pH 6; therefore, the decrease in sulfo-Cy3 emission has to be caused by peptide conformation change. Once pH dropped below pH 5.5, the L40C* folded into alpha-helical coiled-coil, brought the N-terminal sulfo-Cy3 into proximity, and caused fluorescence self-quenching.
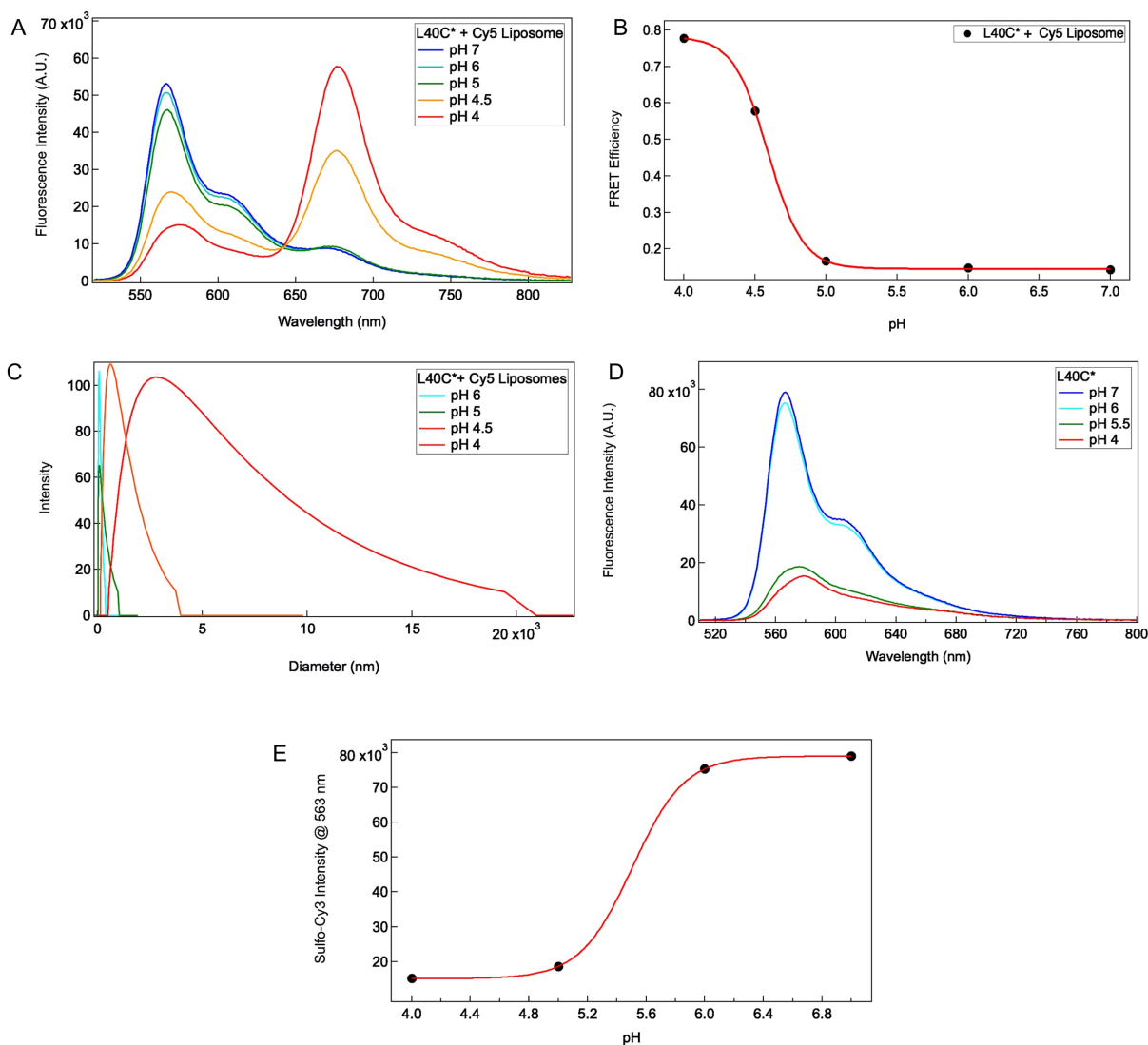
Figure 4.5. (A) Fluorescence spectra of L40C* conjugated to Cy5 liposomes containing 20 mol% maleimide lipids, titrated from pH 7 to pH 4. (B) FRET efficiency calculated for L40C*-Cy5 liposomes conjugates as a function of pH with equation 2. The values were fitted to a sigmoid. (C) Hydrodynamic radii of the L40C*-Cy5 liposomes conjugates titrated from pH 6 to pH 4, measured with dynamic light scattering. (D) Fluorescence spectra of L40C*, titrated from pH 7 to pH 4. (E) pH-dependence of sulfo-Cy3 emission intensity fit into a sigmoid, with X_{half} at pH 5.5.

Liposome leakage assay and fusion assay of L40C* liposome conjugate showed neither leakage nor fusion as the pH acidified, suggesting that at acidic pH, the extended coiled-coil L40C* crosslinked neighboring liposomes instead of fusing them. **(Fig. S4.4)** To verify that FRET and DLS observations were solely due to liposome aggregation, we first showed that acidification of L40C showed only slight peptide aggregation. **(Fig. S4.5)** Second, we measured the fluorescence lifetime of sulfo-Cy3 at pH 7 and pH 4 after conjugated L40C* to a supported lipid bilayer with the same composition as the liposomes and flushed to remove excess liposomes from the surface. The idea was that peptide anchored on a supported lipid bilayer would lack liposomes to interact with after the formation of an extended helix at acidic pH. The increase in distance between the acceptor and the donor as a result of helix formation would resulting in low FRET. [24] Indeed, we observed that the sulfo-Cy3 has a longer fluorescence lifetime at pH 4 and a shorter fluorescence lifetime at pH 7, suggesting that quenching of the donor fluorescence and low FRET at acidic pH. **(Fig. S4.6)** These results imply that the change in pH triggers a conformation change in the peptide, increasing the distance between the Cy5 acceptor in the supported lipid bilayer and the sulfo-Cy3 donor on the peptide.

We measured the fluorescence emission intensity of Cy5 liposomes at pH 7 and pH 4. The fluorescence intensity of the Cy 5 liposomes exhibited minimal change when titrated from pH 7 to pH 4. **(Fig. S4.7A)** Conjugating the dye-free L40C peptide to the Cy5 liposome resulted in no change in Cy5 emission intensity as the solution acidified. **(Fig. S4.7D)** Furthermore, the emission intensity of pure sulfo-Cy3 dye decreased slightly in the pH 4 solution. **(Fig. S4.7B)** Attaching the dye-labeled L40C* to dye-free liposomes resulted in a slight decrease in the sulfo-Cy3 intensity as the pH drops. **(Fig. S4.7C)** The decrease in sulfo-Cy3 intensity in free sulfo-Cy3 and L40C*-dye-free liposome conjugates were much smaller than the decrease in FRET samples. Therefore, the changes in sulfo-Cy3 fluorescence in the FRET samples were likely due to peptide conformation

change and subsequent liposome interactions. These results collectively confirmed that the changes in FRET efficiency and hydrodynamic radii were likely due to liposome crosslinking mediated by the pH-triggered peptide conformation change.

Stopped-flow FRET

We employed stopped-flow FRET to measure the liposome crosslinking kinetics driven by L40C* conformational change at acidic pH. The L40C* and Cy5 liposome conjugates in 10 mM phosphate pH 7 buffer were mixed with 100 mM acetate buffer at pH 4 in a 1:1 ratio. **Figure 6A** and figure 6B were representative stopped-flow FRET transients of L40C* conjugated to Cy5 liposomes. The Cy5 channel reflects the fluorescence signal from Cy5 liposomes and the traces showed an increase in Cy5 fluorescence. **(Fig. 6A)** The sulfo-Cy3 channel follows the L40C* fluorescence and the traces showed a decrease in sulfo-Cy3 fluorescence. **(Fig. 6A)** We varied the concentration of maleimide lipids in the Cy5 liposome from 10 mol% to 20 mol%. All sulfo-Cy3 and Cy5 traces were best fitted to a single exponential to extract time constants. (Equation 3) It is interesting to note that there seems to be a fast component that existed before 0.1 s across all stopped-flow traces. The time constants extracted from the sulfo-Cy3 channel span from 0.6 s to 1.27 s, but are not statistically different, whereas the time constants vary between 0.45 s to 0.65 s in the Cy5 channel. **(Fig.6C)** Peptide conformation change typically takes place on a much faster timescale. Atomistic molecular dynamic simulation for the trimeric B-loop region of HA2 of the H3 subtype showed it look over 1.4 ms for the trimeric B-loop to reach a post-fusion like coiled-coil from the pre-fusion structure. [8] The folding time for a fast-folding helical bundle protein is about 10 μs and for a tethered leucine zipper is about 30 μs. [25-26] [27] Therefore, the slow events resolved from stopped-flow FRET of L40C* and Cy5 liposome conjugates and stopped-flow fluorescence of L40C* are likely due to the formation of large structures such as liposome aggregates, but not

peptide structural rearrangement. Also, despite various modifications to the stopped-flow mixing instrument, instrumental limitation prevents access to microsecond timescale events and hinders the study of the L40C* folding dynamics on liposomes. **Figure 6D** shows FRET efficiencies extracted from stopped-flow traces and shows its evolution over time. The magnitudes of the FRET efficiencies for the peptide liposome conjugates with 10 mol% and 20 mol% maleimide lipid concentrations agree with the values extracted from steady-state FRET measurement. **(Fig. 6E)**

We performed stopped-flow fluorescence measurements on L40C* peptide, sulfo-Cy3 dye, and Cy5 liposomes separately as a control. **(Fig. 6E, S4.9A, S4.9B)** The stopped-flow transient of the L40C* exhibited biphasic behavior. By fitting the trace to a double exponential **(equation 5)**, it revealed a fast component at 4.73 ms and a slow component at 0.595 s. It has been shown that monomeric peptides representing the B-loop could adopt beta-sheet structures at neutral pH [8] [28], and glutamic acid residues in coiled-coil structures could promote aggregation. [18-20] Indeed, size exclusion chromatography of the L40C peptide showed a small population of oligomers at pH 7 **(Fig. 3F)**, and FTIR at pD 4 showed the formation of the beta-sheet at high peptide concentration. **(Fig. 3D)** Therefore, the slow component observed in the L40C* peptide could be a combination of the coiled-coil structure's aggregation after the pH-driven peptide folding and formation of beta-sheet structures from monomeric L40C* that adopted beta-sheet conformation at neutral pH. The fast component observed in L40C* could be due to the association of individual helices to form coiled-coil structures on the lipid membrane.

The stopped-flow trace of Cy 5 liposomes did not exhibit any changes in signal over time, which was not surprising given those liposomes were not conjugated to any peptides. **(Fig. S4.9B)** Also, the sulfo-Cy3 signal did not change as the solution was acidified, indicating that the signal observed in the L40C*-Cy5 liposome conjugates must be due to changes in the peptide. **(Fig. S4.9A)**
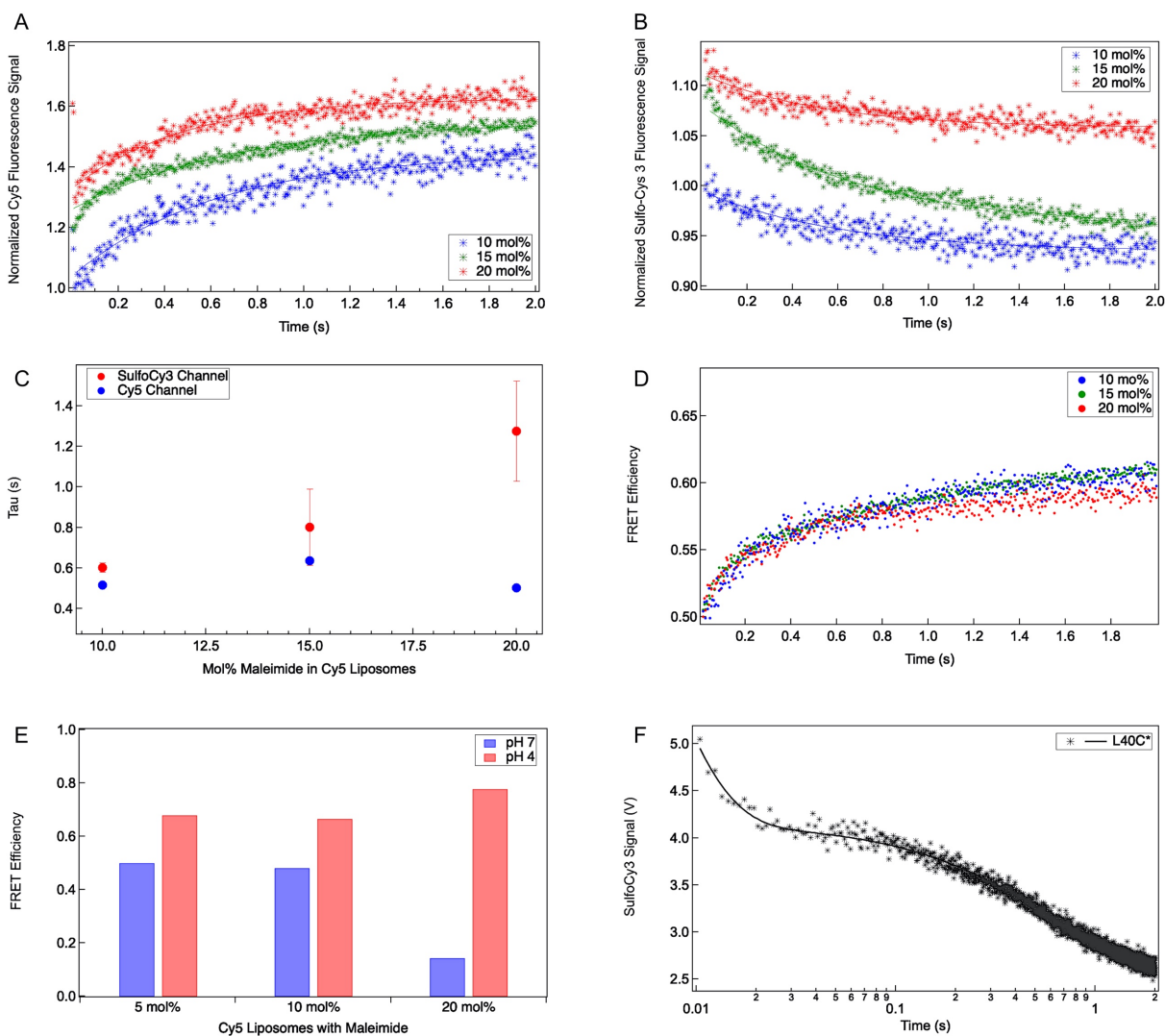
Figure 4.6. (A) Stopped-flow traces of the Cy5 channel of L40C*-Cy5 liposome conjugate at 10 mol%, 15 mol%, 20 mol% maleimide concentration from 0 to 2 s. (B) Stopped-flow traces of the sulfo-Cy3 channel of L40C*-Cy5 liposome conjugate at 10 mol%, 15 mol%, 20 mol% maleimide concentration from 0 to 2 s (C) Time constant extracted by fitting the sulfo-Cy3 and Cy5 channels to a single exponential. (D) Change in FRET efficiencies of L40C* conjugated to Cy5 liposomes obtained from sulfo-Cy3 and Cy5 traces. (E) FRET efficiencies of L40C* conjugated to Cy5 liposomes calculated from steady-state fluorescence. (F) Stopped-flow fluorescence trace of the sulfo-Cy3 channel of L40C* peptide from 0 to 2s.

The stopped-flow studies of the L40C*-Cy5 liposome conjugates revealed complex kinetics and events. In particular, the sulfo-Cy3 signal from the L40C* and Cy5 liposome conjugates contained contributions from L40C*. The sulfo-Cy3 emission intensity of the L40C* peptide showed an intrinsic pH-dependent response, including the slight decrease in sulfo-Cy3 fluorescence when the peptide was attached to pure DOPC liposomes at acidic pH and the biphasic kinetics behavior observed in stopped-flow fluorescence. **(Fig. S4.7C and 6F)** Additional studies are needed to delineate the peptide-membrane interactions.
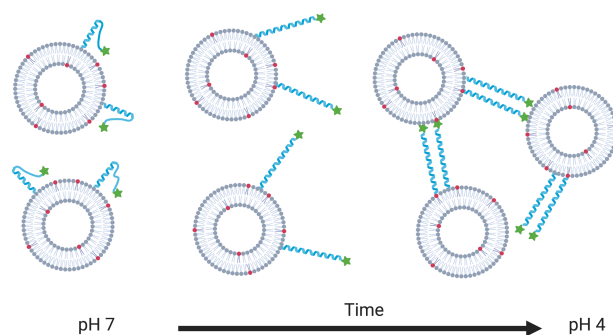
Figure 4.7. A model illustrating the pH-driven L40C* conformational change and subsequent liposome crosslinking.

On the other hand, the Cy5 fluorescence signal avoided problems encountered in the sulfo-Cy3 channel. The Cy5 fluorescence was not as sensitive as sulfo-Cy3 to liposome environment and pH and showed little fluctuation in its emission intensity. **(Fig. 6E, S4.7A, S.4.7E)** When the unlabeled L40C was attached to the Cy5 containing liposomes, the Cy5 fluorescence intensity did not change upon acidification. **(Fig S.4.7D)** Therefore, the increase in Cy5 fluorescence in the stopped-flow FRET traces of L40C* and Cy5 liposome conjugates must be due to its proximity to the sulfo-Cy3 dye on L40C* and the corresponding energy transfer. Time constants resolved from

the Cy5 channel showed no relationship to the increasing maleimide lipid concentration, suggesting liposome crosslinking happened on a similar timescale regardless of peptide concentration. Based on these results, the L40C* peptide likely led to liposome crosslinking at acidic pH by first undergoing a loop to helix transition, followed by insertion into the surrounding liposomes interaction between sulfo-Cy3 and cy5. **(Fig 5.7)** Additional studies are required to explore the role of peptide association on membrane surface on liposome crosslinking and provide more details into the steps leading up to crosslinking.

Although we initially aimed to study L40C*-mediated membrane fusion and resolve membrane fusion kinetics relevant to HA2, this study provides insights into understanding how pH-sensitive-peptide conjugated liposomes could interact under different conditions. Peptide conjugated liposomes responsive to external stimuli have been designed for drug delivery, particularly in cancer therapy. [29-31] For instance, utilizing the acidic microenvironment in cancer cells as a trigger, liposomes decorated with pH-responsive antimicrobial peptides and integrin αvβ3-targeted peptides have been designed to deliver the chemotherapy drug, paclitaxel. [29]. Furthermore, GALA peptide, a peptide that folds from random coil to alpha-helix upon acidification, has been conjugated to liposomes for drug delivery. [32-33] This study offers initial mechanistic insights into peptide mediate liposome interactions as a result of external stimuli. Additional studies would further add details to understanding pH-sensitive peptide-mediated liposome interactions and better design peptide conjugated liposomes.

4.4 Conclusion

In summary, we showed that the disordered L40C peptide folded into alpha-helical moiety upon acidification. The peptide existed as a mixture of oligomers and monomers at pH 7 and as a trimer at pH 4, as shown by size exclusion chromatography. We conjugated L40C* to Cy5

liposomes to study how liposomes interact following the acid-induced peptide conformational change. Using DLS, steady-state FRET, and stopped-flow FRET measurements, we showed that the L40C* conjugated liposomes crosslinked to each other in acidic pH at a similar timescale regardless of peptide concentration. This study offers initial mechanistic insights into peptide-mediated liposome interactions in response to pH-driven peptide conformational change. Additional studies would add value to understanding the molecular details of using peptide-conjugated liposomes for drug delivery.

4.5 References

1.   Skehel, J. J.; Wiley, D. C., Receptor binding and membrane fusion in virus entry: the influenza hemagglutinin. *Annu Rev Biochem* **2000,** *69*, 531-69.

2.   Boonstra, S.; Blijleven, J. S.; Roos, W. H.; Onck, P. R.; van der Giessen, E.; van Oijen, A. M., Hemagglutinin-Mediated Membrane Fusion: A Biophysical Perspective. *Annu Rev Biophys* **2018,** *47*, 153-173.

3.   Chen, J.; Skehel, J. J.; Wiley, D. C., N- and C-terminal residues combine in the fusion-pH influenza hemagglutinin HA(2) subunit to form an N cap that terminates the triple-stranded coiled coil. *Proceedings of the National Academy of Sciences of the United States of America* **1999,** *96* (16), 8967-72.

4.   Sauter, N. K.; Hanson, J. E.; Glick, G. D.; Brown, J. H.; Crowther, R. L.; Park, S. J.; Skehel, J. J.; Wiley, D. C., Binding of influenza virus hemagglutinin to analogs of its cell-surface receptor, sialic acid: analysis by proton nuclear magnetic resonance spectroscopy and X-ray crystallography. *Biochemistry* **1992,** *31* (40), 9609-21.

5.   Carr, C. M.; Kim, P. S., A spring-loaded mechanism for the conformational change of influenza hemagglutinin. *Cell* **1993,** *73* (4), 823-32.

6.   Bullough, P. A.; Hughson, F. M.; Skehel, J. J.; Wiley, D. C., Structure of influenza haemagglutinin at the pH of membrane fusion. *Nature* **1994,** *371* (6492), 37-43.

7.   Carr, C. M.; Chaudhry, C.; Kim, P. S., Influenza hemagglutinin is spring-loaded by a metastable native conformation. *Proceedings of the National Academy of Sciences of the United States of America* **1997,** *94* (26), 14306-13.

8.   Lin, X.; Noel, J. K.; Wang, Q.; Ma, J.; Onuchic, J. N., Atomistic simulations indicate the functional loop-to-coiled-coil transition in influenza hemagglutinin is not downhill. *Proceedings of the National Academy of Sciences of the United States of America* **2018,** *115* (34), E7905-E7913.

9.   Lin, X.; Noel, J. K.; Wang, Q.; Ma, J.; Onuchic, J. N., Lowered pH Leads to Fusion Peptide Release and a Highly Dynamic Intermediate of Influenza Hemagglutinin. *J Phys Chem B* **2016,** *120* (36), 9654-60.

10.   Lin, X.; Eddy, N. R.; Noel, J. K.; Whitford, P. C.; Wang, Q.; Ma, J.; Onuchic, J. N., Order and disorder control the functional rearrangement of influenza hemagglutinin. *Proceedings of the National Academy of Sciences of the United States of America* **2014,** *111* (33), 12049-54.

11.   Slepenkov, S. V.; Darzynkiewicz, E.; Rhoads, R. E., Stopped-flow kinetic analysis of eIF4E and phosphorylated eIF4E binding to cap analogs and capped oligoribonucleotides: evidence for a one-step binding mechanism. *The Journal of biological chemistry* **2006,** *281* (21), 14927-38.

12.   Jia, Y.; Kumar, A.; Patel, S. S., Equilibrium and stopped-flow kinetic studies of interaction between T7 RNA polymerase and its promoters measured by protein and 2-aminopurine fluorescence changes. *The Journal of biological chemistry* **1996,** *271* (48), 30451-8.

13.   Lau, S. Y.; Taneja, A. K.; Hodges, R. S., Synthesis of a model protein of defined secondary and quaternary structure. Effect of chain length on the stabilization and formation of two-stranded alpha-helical coiled-coils. *The Journal of biological chemistry* **1984,** *259* (21), 13253-61.

14.   Cooper, T. M.; Woody, R. W., The effect of conformation on the CD of interacting helices: a theoretical study of tropomyosin. *Biopolymers* **1990,** *30* (7-8), 657-76.

15.   Susi, H.; Timasheff, S. N.; Stevens, L., Infrared spectra and protein conformations in aqueous solutions. I. The amide I band in H2O and D2O solutions. *The Journal of biological chemistry* **1967,** *242* (23), 5460-6.

16.   Davis, C. M.; Cooper, A. K.; Dyer, R. B., Fast helix formation in the B domain of protein A revealed by site-specific infrared probes. *Biochemistry* **2015,** *54* (9), 1758-66.

17.   Kubelka, J.; Keiderling, T. A., Differentiation of beta-sheet-forming structures: ab initio-based simulations of IR absorption and vibrational CD for model peptide and protein beta-sheets. *Journal of the American Chemical Society* **2001,** *123* (48), 12048-58.

18.   Fiumara, F.; Fioriti, L.; Kandel, E. R.; Hendrickson, W. A., Essential role of coiled coils for aggregation and activity of Q/N-rich prions and PolyQ proteins. *Cell* **2010,** *143* (7), 1121-35.

19.   Barrera, E. E.; Zonta, F.; Pantano, S., **2020**.

20.   Haider, M. J.; Zhang, H. V.; Sinha, N.; Fagan, J. A.; Kiick, K. L.; Saven, J. G.; Pochan, D. J., Self-assembly and soluble aggregate behavior of computationally designed coiled-coil peptide bundles. *Soft Matter* **2018,** *14* (26), 5488-5496.

21.   Hughes, L. D.; Rawle, R. J.; Boxer, S. G., Choose your label wisely: water-soluble fluorophores often interact with lipid bilayers. *PloS one* **2014,** *9* (2), e87649.

22.   Swalley, S. E.; Baker, B. M.; Calder, L. J.; Harrison, S. C.; Skehel, J. J.; Wiley, D. C., Full-length influenza hemagglutinin HA2 refolds into the trimeric low-pH-induced conformation. *Biochemistry* **2004,** *43* (19), 5902-11.

23.   Garcia, N. K.; Guttman, M.; Ebner, J. L.; Lee, K. K., Dynamic changes during acid-induced activation of influenza hemagglutinin. *Structure* **2015,** *23* (4), 665-76.

24.   Rajoria, S.; Zhao, L.; Intes, X.; Barroso, M., FLIM-FRET for Cancer Applications. *Curr Mol Imaging* **2014,** *3* (2), 144-161.

25.   Kubelka, J.; Hofrichter, J.; Eaton, W. A., The protein folding 'speed limit'. *Curr Opin Struct Biol* **2004,** *14* (1), 76-88.

26.   Lindorff-Larsen, K.; Piana, S.; Dror, R. O.; Shaw, D. E., How fast-folding proteins fold. *Science* **2011,** *334* (6055), 517-20.

27.   Donten, M. L.; Hassan, S.; Popp, A.; Halter, J.; Hauser, K.; Hamm, P., pH-jump induced leucine zipper folding beyond the diffusion limit. *J Phys Chem B* **2015,** *119* (4), 1425-32.

28.   Casali, M.; Banta, S.; Zambonelli, C.; Megeed, Z.; Yarmush, M. L., Site-directed mutagenesis of the hinge peptide from the hemagglutinin protein: enhancement of the pH-responsive conformational change. *Protein Eng Des Sel* **2008,** *21* (6), 395-404.

29.   Zhang, Q.; Lu, L.; Zhang, L.; Shi, K.; Cun, X.; Yang, Y.; Liu, Y.; Gao, H.; He, Q., Dual-functionalized liposomal delivery system for solid tumors based on RGD and a pH-responsive antimicrobial peptide. *Scientific reports* **2016,** *6*, 19800.

30.   Turk, M. J.; Reddy, J. A.; Chmielewski, J. A.; Low, P. S., Characterization of a novel pH-sensitive peptide that enhances drug release from folate-targeted liposomes at endosomal pHs. *Biochim Biophys Acta* **2002,** *1559* (1), 56-68.

31.   Zhao, Y.; Ren, W.; Zhong, T.; Zhang, S.; Huang, D.; Guo, Y.; Yao, X.; Wang, C.; Zhang, W. Q.; Zhang, X.; Zhang, Q., Tumor-specific pH-responsive peptide-modified pH-sensitive liposomes containing doxorubicin for enhancing glioma targeting and anti-tumor activity. *J Control Release* **2016,** *222*, 56-66.

32.   Santiwarangkool, S.; Akita, H.; Nakatani, T.; Kusumoto, K.; Kimura, H.; Suzuki, M.; Nishimura, M.; Sato, Y.; Harashima, H., PEGylation of the GALA Peptide Enhances the Lung-

Targeting Activity of Nanocarriers That Contain Encapsulated siRNA. *J Pharm Sci* **2017,** *106* (9), 2420-2427.

33.   Subbarao, N. K.; Parente, R. A.; Szoka, F. C., Jr.; Nadasdi, L.; Pongracz, K., pH-dependent bilayer destabilization by an amphipathic peptide. *Biochemistry* **1987,** *26* (11), 2964-72.

4.6 Supporting Information

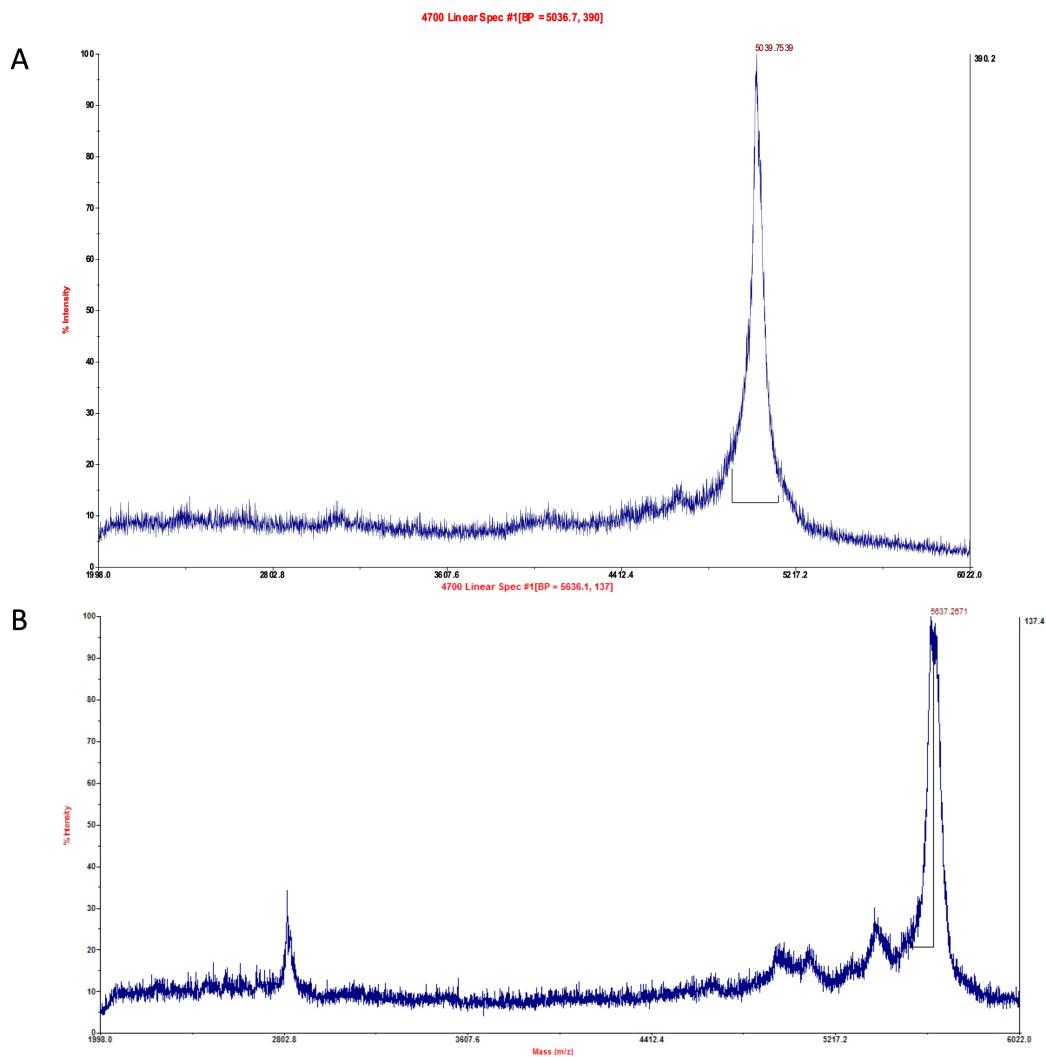### 4.6.1 Supplemental results

MALDI MS of L40C and L40C*

Figure S4.1. (A) The mass spectrum of L40C revealed a peak at 5039 amu. L40C has a theoretical mass of 5013 Da. (B) The mass spectrum of L40C* revealed a prominent peak at 5637.26 amu, assigned to [peptide + dye]$^+$ and a weaker peak at 2802.8 amu as [peptide + dye]$^{2+}$.
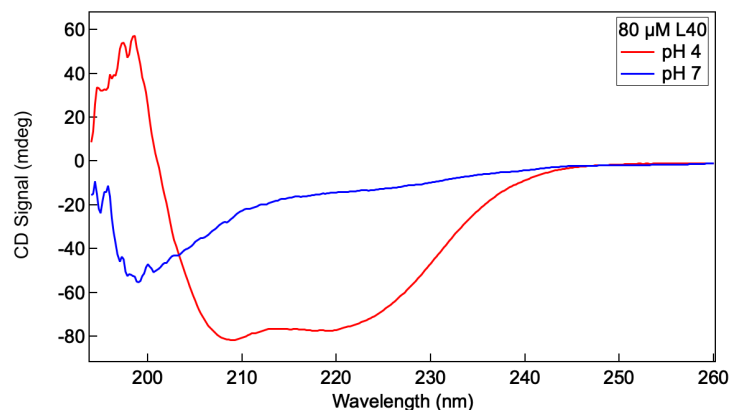
Figure S4.2. CD spectrum of L40 peptide without cysteine at the C-terminus in 10 mM phosphate buffer at pH 7 (blue) and pH 4 (red). The CD spectrum resembles the one of the L40C, with which both peptides folded into alpha-helix at pH 4.
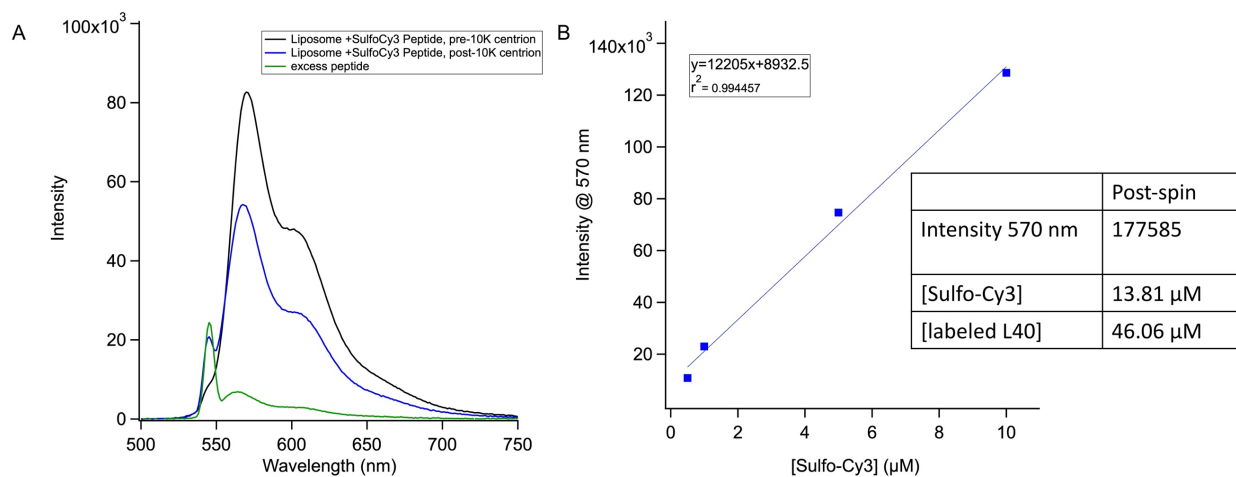
Cy3 fluorescence assay

Figure S4.3. The Cy3 fluorescence assay first obtained a calibration curve by measuring the change in Cy3 fluorescence intensity as a function of Cy3 concentration. Then, the L40C* liposome conjugate's emission intensity was fitted to the calibration curve to generate an estimate of peptide concentration.

Leakage and fusion assay
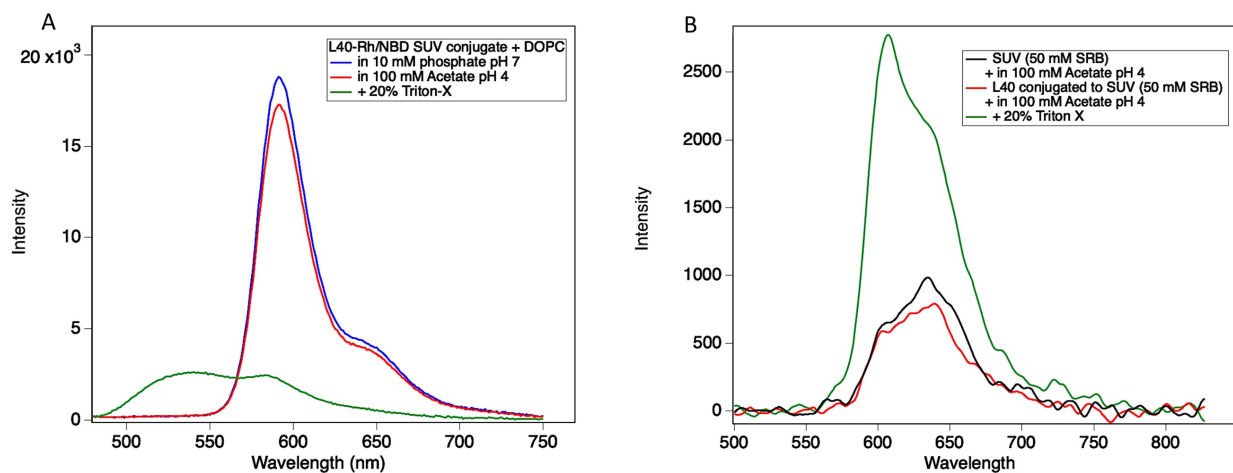
Figure S4.4. (A) Liposome fusion assay was performed according to published protocol. [34] L40C was conjugated to liposomes filled with NBD/Rhodamine dyes mixed with liposomes without any dyes or peptides. At pH 7 and pH 4, rhodamine fluoresced. The addition of Triton-X lysed the liposomes resulting in a decrease in rhodamine fluorescence. (B) Liposome leakage assay was performed according to published protocol.[35] L40C was conjugated to liposomes filled with a self-quenching concentration (50 mM) sulforhodamine B. Acidifying the samples to pH 4 did not increase sulforhodamine B fluorescence. The addition of Triton-X increased sulforhodamine B fluorescence due to the lysing of liposomes and subsequent dilution of dye.
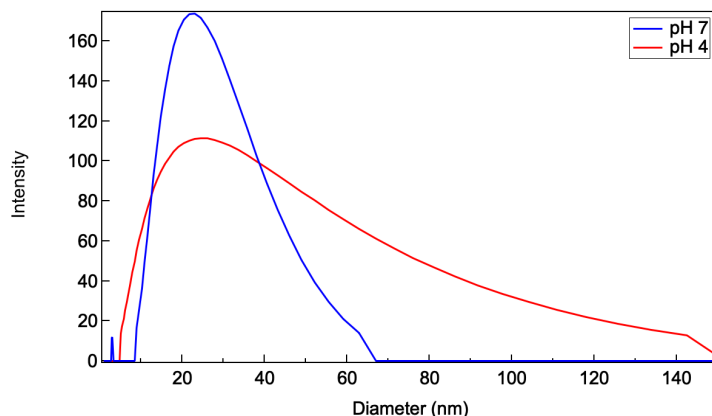
Figure S4.5. Intensity distribution of L40C in 10 mM phosphate buffer at pH 7 (blue)and pH 4 (red) measured by dynamic light scattering. Hydrodynamic radii of the peptide are 27.9 nm at pH 7 (polydispersity index = 0.169) and 32.5 nm at pH 4 (polydispersity index = 0.224).

Fluorescence lifetime of sulfo-Cy3 on L40C* at pH 7 and pH 4
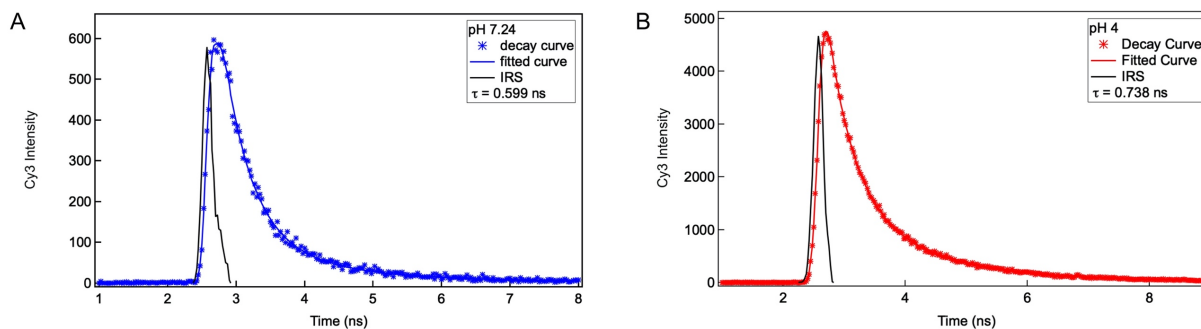
Figure S4.6. Fluorescence lifetime decay trace of L40C* attached to the supported lipid bilayer (80 mol% DOPC/ 20 mol% DSPE-maleimide) (A) At pH 7, the fluorescence lifetime of sulfo-Cy3 was 0.599 ns. (B) At pH4, the fluorescence lifetime of sulfo-Cy3 was 0.738 ns.
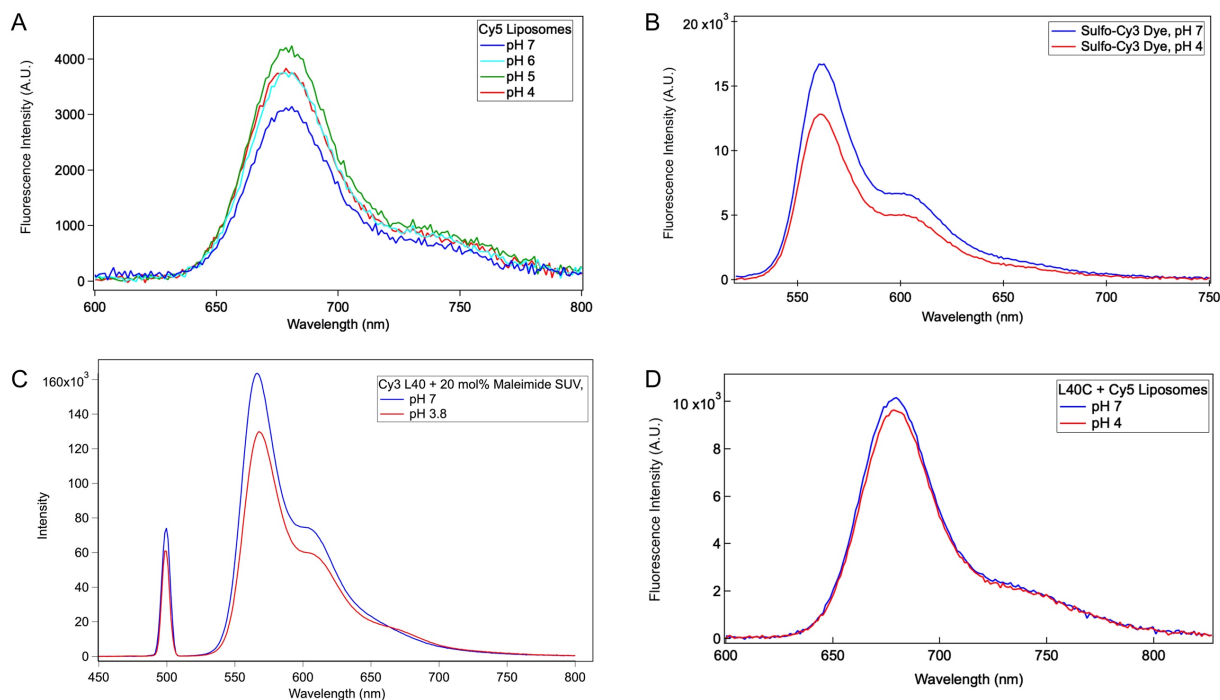
Figure S4.7. (A) Cy5 fluorescence emission of Cy5 liposomes showed an insignificant change as pH decreased. (B) Sulfo-Cy3 emission intensity showed a slight decrease when the pH decreased. (C) L40C* was attached to liposomes without Cy5. As the solution was acidified, Sulfo-Cy3 emission intensity decreased slightly, while there was no increase in fluorescence intensity at the Cy5 emission wavelength. (D) L40C was attached to Cy5 liposomes. The Cy5 fluorescence intensity did not change when the solution acidified.
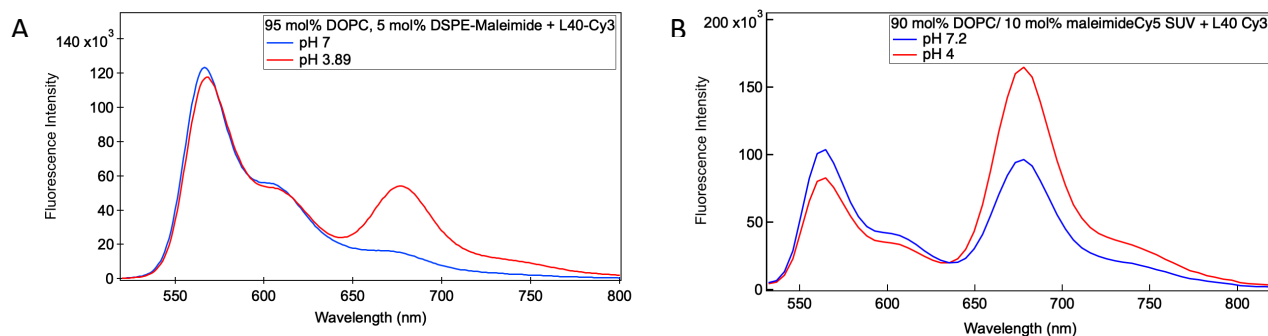
Figure S4.8. Fluorescence spectrum of L40C* conjugated to Cy5 liposomes with varying maleimide DSPE. (A) 5 mol% maleimide DSPE. (B) 10 mol% maleimide DSPE.

Stopped-flow FRET
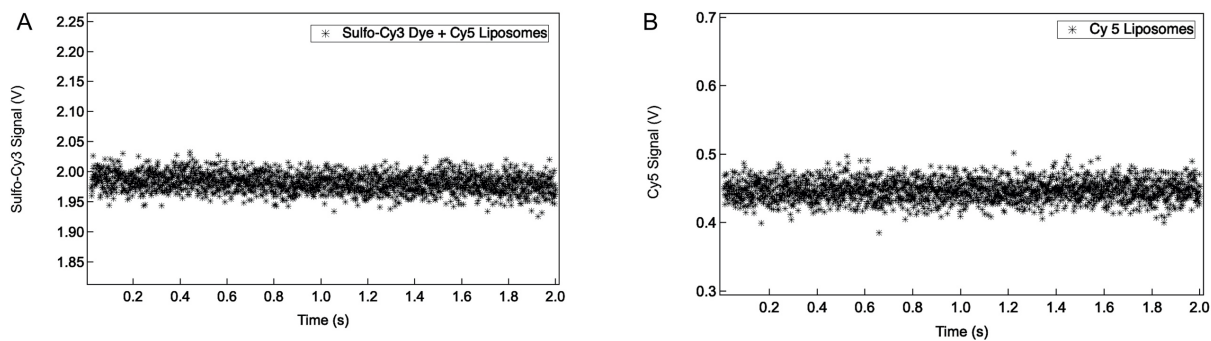
Figure S4.9. (A) Stopped flow trace of sulfo-Cy3 dye and Cy5 liposomes mixed with pH 4 buffer. (B) Stopped flow trace of Cy5 liposomes mixed with pH 4 buffer.

4.6.2 Supplemental references

34.   Kreye, S.; Malsam, J.; Sollner, T. H., In vitro assays to measure SNARE-mediated vesicle fusion. *Methods in molecular biology* **2008,** *440*, 37-50.

35.   Yu, H.; Rathore, S. S.; Lopez, J. A.; Davis, E. M.; James, D. E.; Martin, J. L.; Shen, J., Comparative studies of Munc18c and Munc18-1 reveal conserved and divergent mechanisms of Sec1/Munc18 proteins. *Proceedings of the National Academy of Sciences of the United States of America* **2013,** *110* (35), E3271-80.

Chapter 5:

Characterization of a Host-Defense Peptide, Urumin, and Its Interactions with Lipid Membranes and the Influenza H3N2 X-31 Hemagglutinin

Siaw, H.M.H. and Dyer, R.B.

5.1 Abstract

The influenza virus is the most common respiratory virus circulating among humans. With the emergence of adamantanes resistant strains, the burden of viral therapy falls on neuraminidase inhibitors and reflects the need to develop new therapeutics. Recently, a host defense peptide called urumin was isolated from skin secretions of the frog *Hydrophylax bahuvistara*. The peptide exhibited antiviral activity in MDCK cells, suppressed the growth of H1N1 viruses and selectively targeted the conserved stalk region of the influenza hemagglutinin (HA2 subunit). Electron microscopy further showed that urumin destroyed the influenza virion upon incubation. As a class of antimicrobial peptides, host defense peptides have been shown to interact with charged lipids and disrupt membranes. Specific interactions between antiviral peptide and HA2 have been presented to inhibit the pH-driven conformational rearrangement necessary for membrane fusion. This study investigated the interaction between urumin and lipids abundant in the PR8 influenza virion with model membranes. The peptide interacted specifically with negatively charged PG and PS lipids and folded from the disordered structure into alpha-helical character. Leakage assay showed that urumin was unable to significantly induce leakage in model membranes, suggesting that the peptide disrupts the influenza virion via mechanisms other than pore formation. We also showed that urumin was unable to inhibit the pH-dependent conformational change in HA2 derived from the influenza X-31 strain.

5.2 Introduction

Influenza is the most common human respiratory virus. It causes 3 - 5 million cases of new infections worldwide per year. There are two classes of approved drugs for influenza: neuraminidase inhibitors and M2 proton channel inhibitors (adamantanes). However, due to the emergence of influenza strains resistant to adamantanes, neuraminidase inhibitors became the preferable therapeutics class. [1-2] There have been numerous efforts to create influenza antivirals, including small molecules, monoclonal antibodies, and host defense peptides. [1][3] Host defense peptides (HDP) are found in innate defense mechanisms in the living organism. They are secreted in large quantities and are less susceptible to resistance. HDPs have been shown to exhibit antimicrobial and antiviral activities against different microbial organisms and viruses. For instance, the human HDP, cathelicidin LL-37, isolated from leukocytes and epithelial cells, has been shown to inhibit microbial infections, eliminate microbes, and modulate host response against infection. [4] Amphibian HDPs have been shown to not only defend against microbial infections in frogs [5] but are also active against human viruses such as HSV-1, HSV-2, and HIV-1 in vitro. [6-10] Therefore, HDP is a useful resource for developing antivirals.

In 2017, Holthausen et al. reported the isolation of a host-defense peptide called urumin from skin secretions of the frog *Hydrophylax bahuvistara*. Urumin is a 27-amino acid peptide with a net 2+ positive charge. The peptide exhibited a virucidal activity against influenza. [11] They showed that the peptide targeted and significantly inhibited the growth of H1N1 and H1N2 viruses while demonstrated slight inhibition to the growth of H3N1 and H3N2 viruses. The study further showed with ELISA, that urumin does not bind to the neuraminidase or hemagglutinin HA1 subunit in the H1 viruses. Instead, the peptide selectively bound to the conserved stalk region, hemagglutinin HA2 subunit, of the H1 viruses. Furthermore, electron microscopy showed the influenza virion (PR8) was destroyed when incubated with the peptide.

Peptidic targeting of hemagglutinin (HA) in influenza has been previously reported. [12] Kadam et al. designed a cyclic peptide that binds to the highly conserved stem region and blocks the low-pH driven conformational rearrangement in HA protein, leading to membrane fusion. [13] It was reported that a 30 amino-acid peptide derived from mouse β-defensin-4, called P9, is active against influenza A virus H1N1, H3N2, H5N1, H7N7, and H7N9. P9 first attaches to HA and gets shuttled to the late endosome. The basic nature of the peptide neutralizes the acidic environment in the late endosome, preventing membrane fusion. [14] Given the different mechanisms that peptides could take to prevent influenza infection, we question whether urumin inhibits influenza viral infection by blocking the pH-driven conformation change in the HA2 subunit.

HDPs are a class of antimicrobial peptides and can interact and disrupt lipid membranes. Well-known models of interactions between antimicrobial peptides and lipid bilayer include pore formation, micellization, binding to specific lipids, membrane thinning, phase separation, induction or inhibition of nonlamellar phases, and transversing the bilayer without disruption. [15] The HDPs LL-36 have been shown to interact and disrupt membranes with different modes of action. [16-18]. Most antimicrobial peptides are positively-charged, and they preferentially target anionic membranes via electrostatic interactions. When the peptide to lipid ratio exceeds a threshold, the peptide could insert into membranes and form transmembrane pores. [19] We question whether urumin displays selectivity towards specific lipid compositions that contribute to the disruption of PR8 influenza virion observed in electron microscopy. Specifically, how does urumin interact with the PR8 virion that consists of negatively charged PG, PA, PS lipid, zwitterionic PE, and PC lipids? [20]

In this study, we characterized the secondary structure of urumin in an aqueous solution and the presence of model lipid membranes with circular dichroism spectroscopy and fluorescence spectroscopy. We found that the peptide selectively interacted with negatively charged lipids. While it was disordered in solution, urumin folded into alpha-helical conformation or mixed conformation

depending on the lipid charge. Lastly, on a ternary lipid mixture resembling the PR8 virion membrane, the peptide did not induce membrane leakage. When urumin was incubated with the HA2 from the H3N2 X-31 strain, the peptide did not inhibit the pH-driven conformational change.

5.3 Experimental Procedures

Peptide synthesis and purification

The amino acid sequence of urumin is IPLRGAFINGRWDSQCHRFSNGAIACA. The peptide was synthesized by standard Fmoc solid-phase peptide synthesis using acid-amine coupling on a Liberty 1 peptide synthesizer (CEM, Matthews, NC) using a rink-amide resin. Fmoc protected amino acids were purchased from AnaSpec, Inc. (Fremont, CA). Purifications of the urumin peptide were completed on a reverse phase C18 column (Phenomenex, Torrance, CA) with TFA as a counterion using a linear gradient of water and acetonitrile. The masses of the purified peptides were confirmed by MALDI-MS using CHCA matrix dissolved in 50:50 mixture of water: acetonitrile. MS confirmed the presence of the urumin with a mass equal to 2961 amu.

Preparation of Large Unilamellar Liposomes (LUV)

Liposomes used in this study were POPC, DPPC, DOPG, DPPG, DOPS/DOPC (20:80 mol%), POPE/POPC (20:80 mol%), DOPS/DOPE/DOPC (20:20:60 mol%), DOPG/DOPE/DOPC (20:30:50 mol%) (Avanti Polar Lipids, Alabaster, Al). Lipids were mixed in chloroform in a glass vial and dried by N_2 gas, after which the sample was placed under vacuum for at least 5 hours to ensure complete removal of solvent. The dried lipid film was rehydrated with 10 mM sodium phosphate buffer pH 7 for 1 hour, followed by 10 rounds of freeze-thaw cycles starting at room temperature and quenching to 4 oC on ice. 100 nm unilamellar vesicles were prepared by

extruding the hydrated solutions 15 times with an extrusion kit (Avanti Polar Lipids, Alabaster, Al) through 100 nm polycarbonate filters at room temperature.

Circular Dichroism

The secondary structures of urumin with or without liposomes, or urumin with or without L40, or urumin with or without HA2 were obtained with circular dichroism spectroscopy. The urumin peptide or the L40 peptide was first dissolved in H2O. The samples were then mixed in 10mM sodium phosphate buffers of pH 4, and 7 and the CD spectra were acquired with a CD instrument equipped with a temperature controller (J-1500 series, JASCO). Samples were transferred to a 1 mm pathlength quartz cuvette. The scanning range of the instrument was set between 190 and 260 nm at a rate of 200 nm/min with a 2 s response time and a 1 nm spectral bandwidth. Molar ellipticities were calculated by:

$MRE=\theta M/ncl$

where θ is the observed ellipticity (mdeg), c is the protein concentration, l is the cuvette path length, M is the molecular weight of protein, and n is the number of peptide bonds. [21]

Tryptophan Fluorescence

Equilibrium tryptophan fluorescence of urumin with or without liposomes in 10 mM phosphor buffer at pH 7 were taken on a FluoroMax spectrophotometer (Horiba Scientific) equipped with a temperature controller (Peltier, Perkin Elmer). Samples were transferred into a 1 cm pathlength fluorescence cuvette. Data were collected using a 2 nm excitation and emission slit widths, by exciting at 280 nm with an integration time of 10 s over a total range of 285-550 nm.

Equilibrium FTIR

Urumin peptide was first subjected to two rounds of D2O and DCl exchange and dried under lyophilization. 10 mM phosphate buffer at pH 7 was subjected to two rounds of D2O exchange and dried under lyophilization. To carry out the experiment, the buffer and the urumin peptide were first rehydrated with D2O. Then the peptide was mixed with the buffer to reach a final concentration of 1mM. The spectrum was collected on a Varian 660 FTIR spectrophotometer (Agilent, Santa Clara, CA) coupled to liquid nitrogen-cooled mercury cadmium (MCT) detector. Samples were prepared in a split IR cell with a 125 μm Teflon spacer between two CaF2 windows in a copper housing. Spectra were collected for both the D2O reference and the urumin peptide sample in 10 mM phosphate buffer at pD 7. Each spectrum was an average of 500 scans at 2 cm^{-1} resolution.

Dynamic Light Scattering

Urumin was added to DOPS/DOPC (20:80 mol%), POPE/POPC (20:80 mol%), DOPS/DOPE/DOPC (20:20:60 mol%) and DOPG/DOPE/DOPC (20:30:50 mol%) liposomes at a range of lipid-to-peptide ratios: 25-to-1, 12.5-to-1, 6-to-1. 80 mL of each sample was transferred to a 1 cm quartz cuvette and data were collected with a NanoPlus-Zeta/Nano Particle Analyzer (Particulate Systems, Norcross, GA). 3x30 measurement runs were performed, with standard setting (Refractive index = 1.331, viscosity= 0.88, temperature = 25 $^{\circ}$C)

Membrane Leakage Assay

50 mM, saturated concentration, sulforhodamine B was prepared by dissolving the dye in 10 mM phosphate buffer at pH 7. DOPS/DOPE/DOPC (20:20:60 mol%) and DOPG/DOPE/DOPC (20:30:50 mol%) dried lipid films were rehydrated with the sulforhodamine

B solution and extruded through 100 nm polycarbonate membrane on a lipid extrusion setup as described previously. Excess dye was removed by a gravity drip size-exclusion Sephadex G-25 column (GE Life Sciences). The sample was excited at 566 nm and fluorescence intensity at 586nm. At 150s or 200s, the peptide was added to the LUV solution. At 600s or 700s, the sample was spiked with a concentrated solution of Tween 20 detergent to induce leakage, resulting in dilution of sulforhodamine B and increased fluorescence intensity.

5.4 Results and Discussion

Urumin is a disordered, random coil

The urumin peptide is a new antiviral peptide isolated in 2017. It has been shown that the peptide targets the HA stalk region specifically and represents a potentially exciting new therapeutics for influenza infection. To understand the peptide structure, we characterized its secondary structure with circular dichroism (CD) spectroscopy and fluorescence spectroscopy. CD spectroscopy has been used extensively to characterize peptide structure. [22]. At pH 7, the peptide showed a negative band at 200 nm, indicating a disordered, random conformation. [23] The urumin maintained its random coil conformation at pH 4. **(Fig. 1A)** The urumin peptide has one tryptophan (trp) residue making it ideal to be characterized with fluorescence spectroscopy. The trp fluorescence is ideally suited for detecting changes in solvation of tryptophan residues. Shifts in emission wavelength can reflect folding and hierarchical changes to the peptide. The urumin peptide displayed no shift in emission wavelength (343 nm) in response to low pH. **(Fig 1B)** This data suggested that the trp residue was not in a more hydrophobic environment in response to a decrease pH but was involved in a quenching interaction. The trp results corroborated with findings from CD spectroscopy. The peptide retained its structure and did not fold into other secondary structures. **Figure 1C** shows the FTIR spectrum of the urumin peptide at pD 7. **Figure 1D** is the secondary derivative of the FTIR

spectrum, enhancing the separation of overlapped peaks in the absorbance spectrum. The negative features in **figure 1D** at 1645 and 1650 cm^{-1} were assigned to the alpha helix. The absence of negative features at 1620 cm^{-1} suggests beta-sheet was not present and that the prominent negative feature at 1672 cm^{-1} was assigned to the random coil.

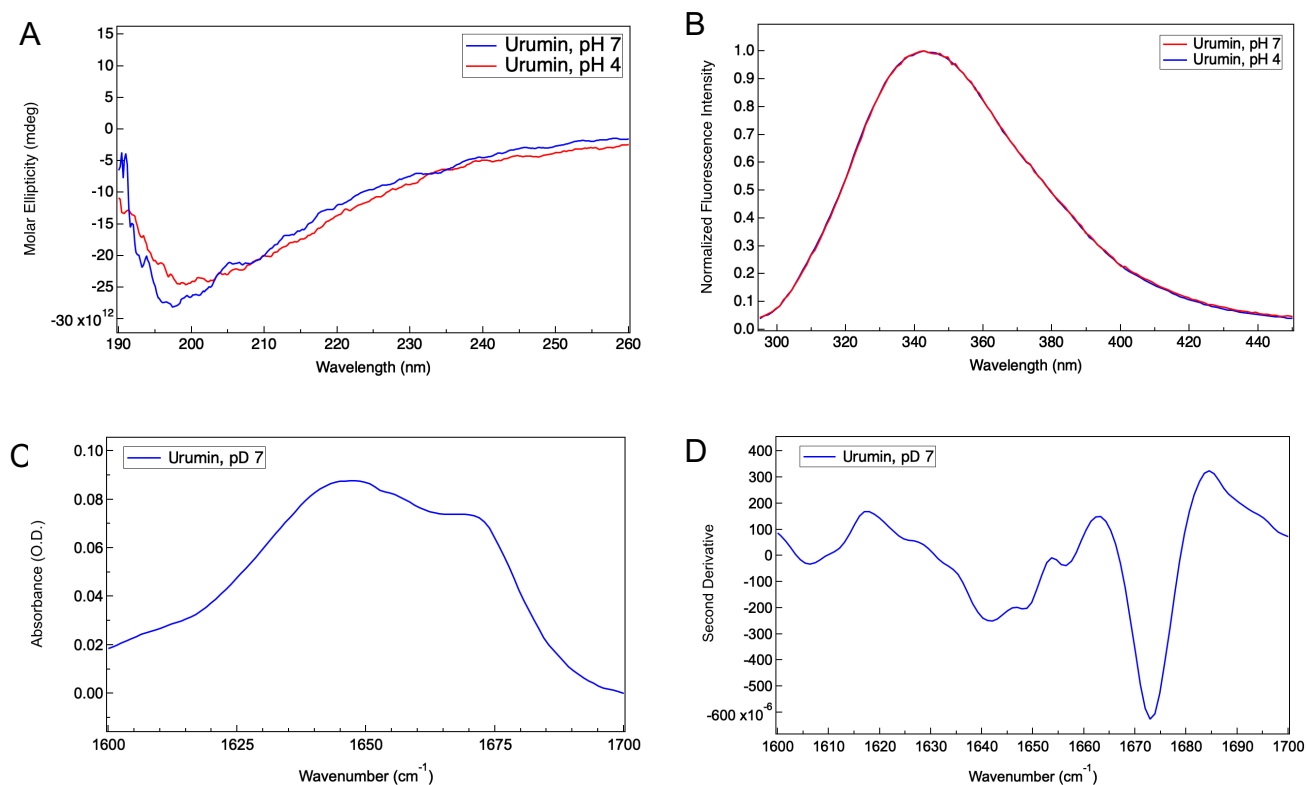**Figure 5.1**. Characterization of the urumin peptide. (A) Circular dichroism spectrum of the peptide in buffers at pH 7 and pH 4. The peptide appeared to adopt a random coil structure at both pHs. (B) Tryptophan fluorescence spectrum of the peptide in buffers at pH 7 and pH 4. (C) FTIR absorbance spectrum at pD 7. (D) Secondary derivative spectrum at pD 7 showed alpha-helix and random coil features.

Urumin did not inhibit H3N2 X31 strain subtype HA2

It has been shown previously that the urumin inhibited the growth of multiple H1N1 viral strains and the H3N2 A/Victoria/3/95. The urumin was also found to target the conserved stalk region (HA2 subunit) of H1 HA. [11] X-31 is another commonly circulated H3N2 strain, and its interaction with urumin has not been investigated. The HA2 B-loop has been regarded as the trigger that leads to the pH-driven conformational change. Upon acidification, the B-loop folds from a predominantly random coil structure to a coiled-coil motif, triggering the transition of HA2 pre-fusion to post-fusion conformation. Figure 3A showed the CD spectra of the B loop before and after acidification. The B-loop was sampled from the influenza X-31 strain HA2 subunit. When the urumin and the B-loop were mixed and acidified to pH 4, B-loop folded into an alpha-helical structure, and the urumin did not inhibit the transition. **(Fig. 2A)**
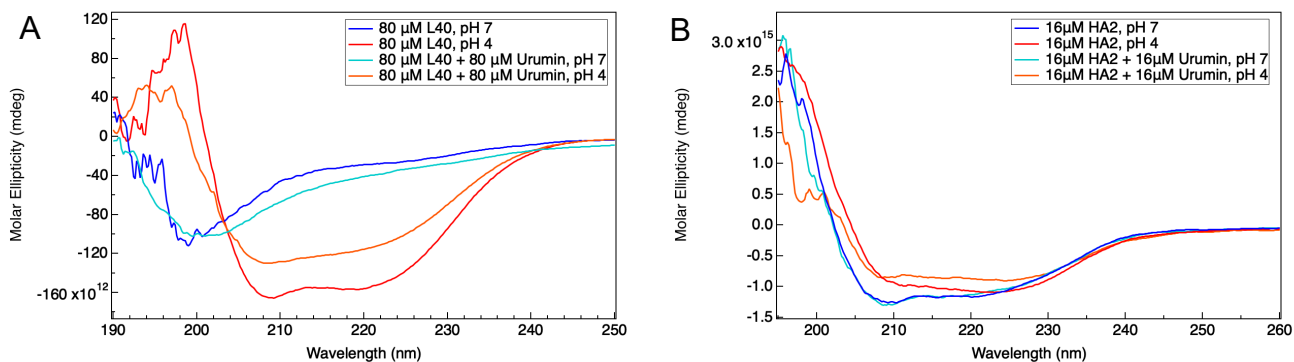
Figure 5.2. (A) Circular dichroism spectra of B-loop at pH 7 (blue) and pH 4 (red) showed the transition from random coil to alpha-helix upon acidification. The addition of urumin to L40 at pH 7 (teal) did not trigger any structural changes. However, at pH 4 (orange), even with urumin, the L40 peptide folded into an alpha helix. (B) Circular dichroism spectra of HA2 at pH 7 (blue) and pH 4 (red) showed a transition to coiled-coil upon acidification. The addition of urumin at pH 7 (teal) followed by acidification to pH 4 (orange) did not inhibit the HA2 from undergoing the pH-dependent coiled-coil formation.

Next, we investigated whether the urumin could inhibit the pH-driven conformational change in HA2. We used a full-length HA2 construct that corresponds to the influenza X-31 strain. At pH 7, the addition of urumin to HA2 did not alter the protein's secondary structure, and it remains mostly alpha-helical. When the mixture was acidified to pH 4, the HA2 was able to undergo conformation change. **(Fig. 2B)** The n - π * ratio at 220 nm to π - π * at 208 nm has been previously used to characterize helical oligomers. The ratio qualitatively indicates the presence of helical oligomers at values greater than 0.86. [24] [25] The CD data of the HA2 in the presence of the urumin indicated a shift in the 220/208 ratio consistent with a coiled-coil formation, a feature prominent in the HA2 post-fusion structure. These results suggested that the urumin did not prevent HA2 conformation change upon acidification. The urumin peptide was unable to inhibit HA2 of the H3N2 X-31 subtype, potentially due to the lack of binding specificity as with other H3N2 subtypes.

Urumin interacted with PC, PG, and PS lipids

Besides binding to the HA2 subunits of the H1 viral subtypes, the urumin peptide has also been shown to disrupt the H1 influenza virus's integrity, specifically the PR8 subtype. Incubating the PR8 virus with the urumin peptide resulted in a destroyed virion, as shown by electron microscopy. [11] This observation prompted an investigation into the interaction between the urumin peptide and lipid peptide at pH 7 using model membrane systems to modulate lipid compositions to mimic different kinds of membranes.

The PR8 virus contains glycerophospholipids with a wide distribution of lipid head groups: 47.9% PE, 24.5% PS, 17.6% SM, 7.5% PC, 2% PA, 0.3% PI, and 0.2% PG. [20] Since the urumin peptide is positively charged (2+), we hypothesized it would selectively interact with negatively charged lipids (PS, PG, PI, SM). We synthesized large unilamellar vesicles (LUV) with an average size of 100 nm and incubated the vesicles with the urumin peptide. LUVs were made of POPC,

DOPC, DPPC, DPPG, DOPG, POPE/POPC, and DOPS/DOPC. We monitored the tryptophan

(trp) fluorescence of the urumin peptide to examine potential peptide-lipid membrane interactions.
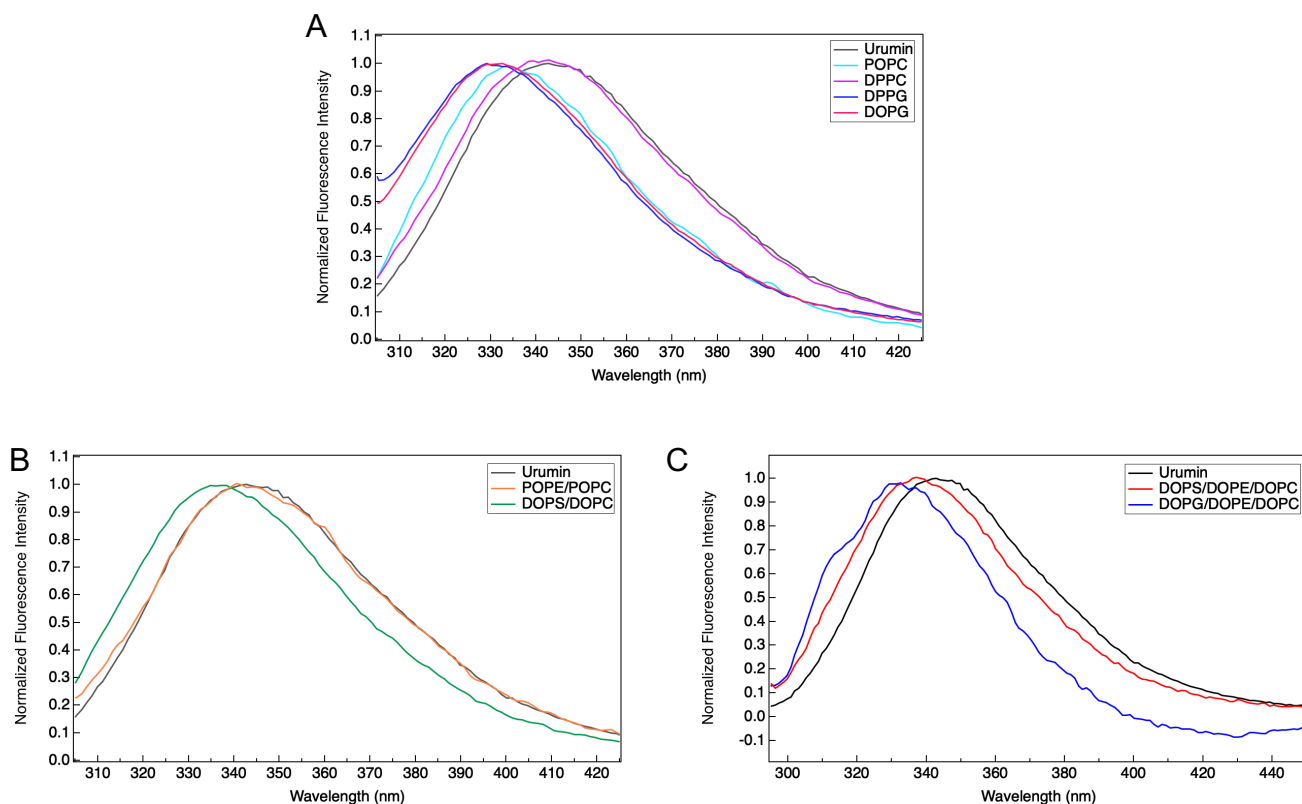
Figure 5.3. Tryptophan (trp) fluorescence of the urumin peptide in the presence of LUVs with varying lipid compositions. The intensities have been normalized to 1 to demonstrate better the blue shift of the lipid+urumin spectra compared to the urumin only spectrum. (A) trp fluorescence of urumin with POPC, DPPC, DPPC, DOPG LUVs. (B) trp fluorescence of urumin with POPE/POPC and DOPE/DOPC LUVs. (C) trp fluorescence of urumin with DOPS/DOPE/DOPC and DOPG/DOPE/DOPC LUVs.

The trp fluorescence emission wavelength of the urumin blue-shifted when incubated with POPC, DOPC, DPPG, and DOPG LUVs. **(Fig. 3A)** Since buried tryptophan residues fluoresce at a shorter wavelength, the tryptophan residues of the urumin were buried in a hydrophobic

environment with LUVs consisting of the zwitterionic PC negatively charged PG lipid headgroups. Interestingly, the trp emission only slightly blue shifted (~2 nm) in the presence of DPPC LUVs. **(Fig. 3A)**

The urumin's trp fluorescence emission wavelength did not change when mixed with POPE/POPC LUVs, suggesting a lack of interaction between the peptide and the LUVs. (Fig 4B) In contrast, there was a blue shift in the emission wavelength when the peptide was mixed with DOPS/DOPC LUVs. **(Fig. 3B) Table 1** summarized the trp emission wavelength maxima of all samples. These results showed the peptide interacted with LUVs containing PC, PG, and PS headgroups. These interactions took place regardless of the lipid chain lengths, as evidence by blue shifts in DOPC (18:1, Δ9cis) and POPC (16:0-18:1) samples.

Sample	Trp Emission Maxima
Urumin, pH 7	344 nm
Urumin, pH 4	344 nm
POPC	335 nm
DPPC	342 nm
DPPG	330 nm
DOPG	330 nm
POPE/POPC	343 nm
DOPS/DOPC	337 nm
DOPS/DOPE/DOPC	337 nm
DOPG/DOPE/DOPC	334 nm

Table 5.1. Trp emission maxima of the urumin in the presence of LUVs. These values were obtained by fitting the trp emission spectrum to the gaussian distribution.

To further investigate the peptide's conformation in a lipid membrane environment that closely resembles the PR virus, we synthesized LUV with ternary lipid mixtures: DOPG/DOPE/DOPC, DOPS/DOPE/DOPC. These mixtures have been reported in other

studies that investigate interactions between membrane and antimicrobial peptides or proteins.[26-27] As with other liposomes containing PG and PS lipids, the trp fluorescence blue-shifted when added to DOPS/DOPE/DOPC and DOPG/DOPE/DOPC LUVs. **(Fig. 3C)**

Urumin folded on PG and PS lipid headgroups

Next, we investigated the structure of the urumin peptide in the presence of LUVs with CD spectroscopy. The peptide transitioned from a disordered random coil into a folded structure with DPPC, DOPG, DPPG, and POPE/POPC. **(Fig. 4A, B)** In DOPG/DOPE/DOPC, the peptide folded into alpha-helical conformation while attaining a mixed secondary structure in POPC and DOPG/DOPE/DOPC LUVs. **(Fig. 4C)** These results further suggested the interaction between the urumin peptide and the lipid membrane and the folding of the peptide are sensitive to lipid headgroups.

These results are not surprising, given urumin as a positively charged peptide. Antiviral peptides are a subclass of the antimicrobial peptide with additional ability in inhibiting viral infection. It has been shown that the unfolded antimicrobial peptides could fold into an alpha helix or beta sheet upon interaction with lipid membrane and led to membrane lysis. [28] [29] Therefore, it is likely the charge interactions between cationic residues in urumin and negatively charged lipid headgroups led to its folding. It was interesting that the peptide would also fold in the presence of zwitterionic lipid, PC. One possible explanation could be the hydrophobic residues in peptide-induced hydrophobic interactions to the zwitterionic membrane.
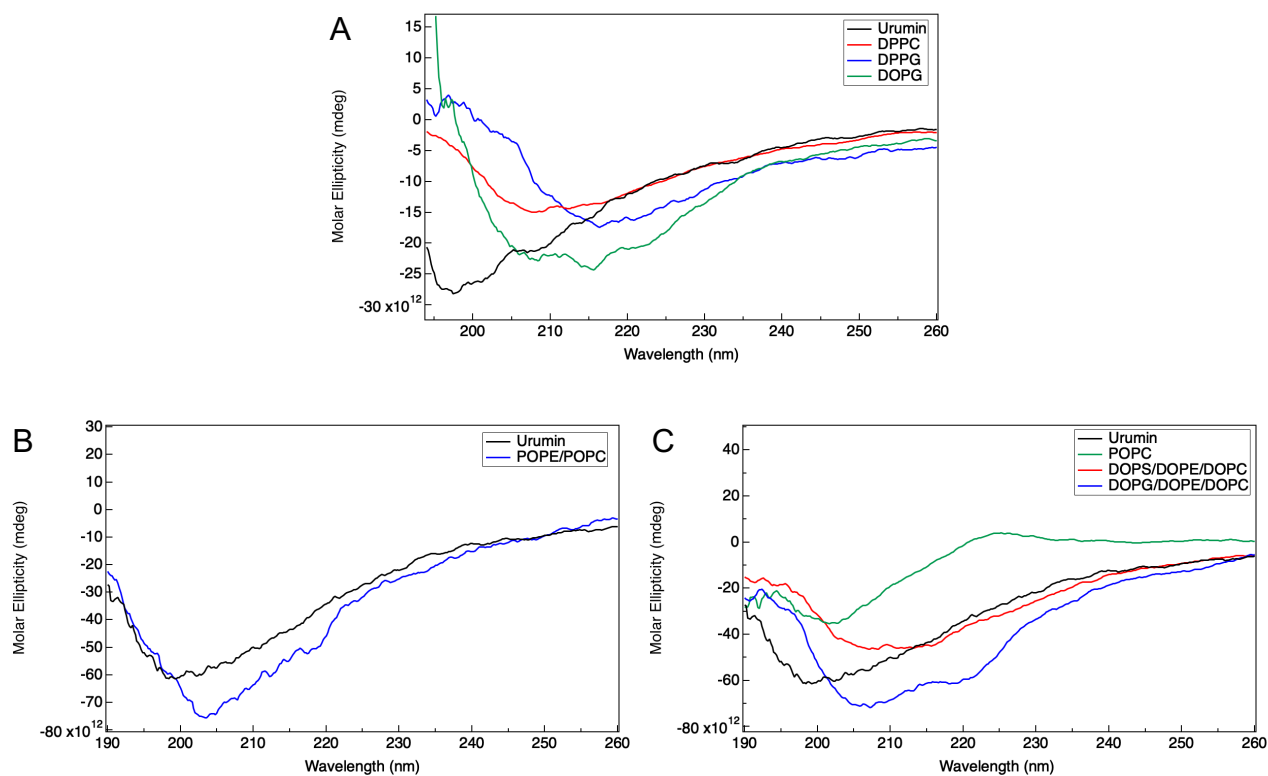
Figure 5.4. CD spectra of urumin with LUVs of various lipid compositions. (A) Urumin with DPPC, DOPC, and DOPG LUVs. (B) Urumin with POPE/POPC LUVs. (C) Urumin with POPC, DOPS/DOPE/DOPC, and DOPG/DOPE/DOPC LUVs.

Dynamic light scattering

Next, we used dynamic light scattering (DLS) to characterize changes in hydrodynamic radii of liposomes in the absence or presence of urumin. Additionally, DLS can be used to monitor membrane aggregation or fusion (an increase in hydrodynamic radius), which have been reported as mechanisms by which some cationic antimicrobial peptides exert their antimicrobial activity on anionic membranes. [30-32][33] Since urumin is a host defense peptide that belongs to a class of antimicrobial peptide, we questioned whether urumin could cause membrane aggregation or fusion that ultimately led to the disruption of the PR8 virion as reported previously. [11]
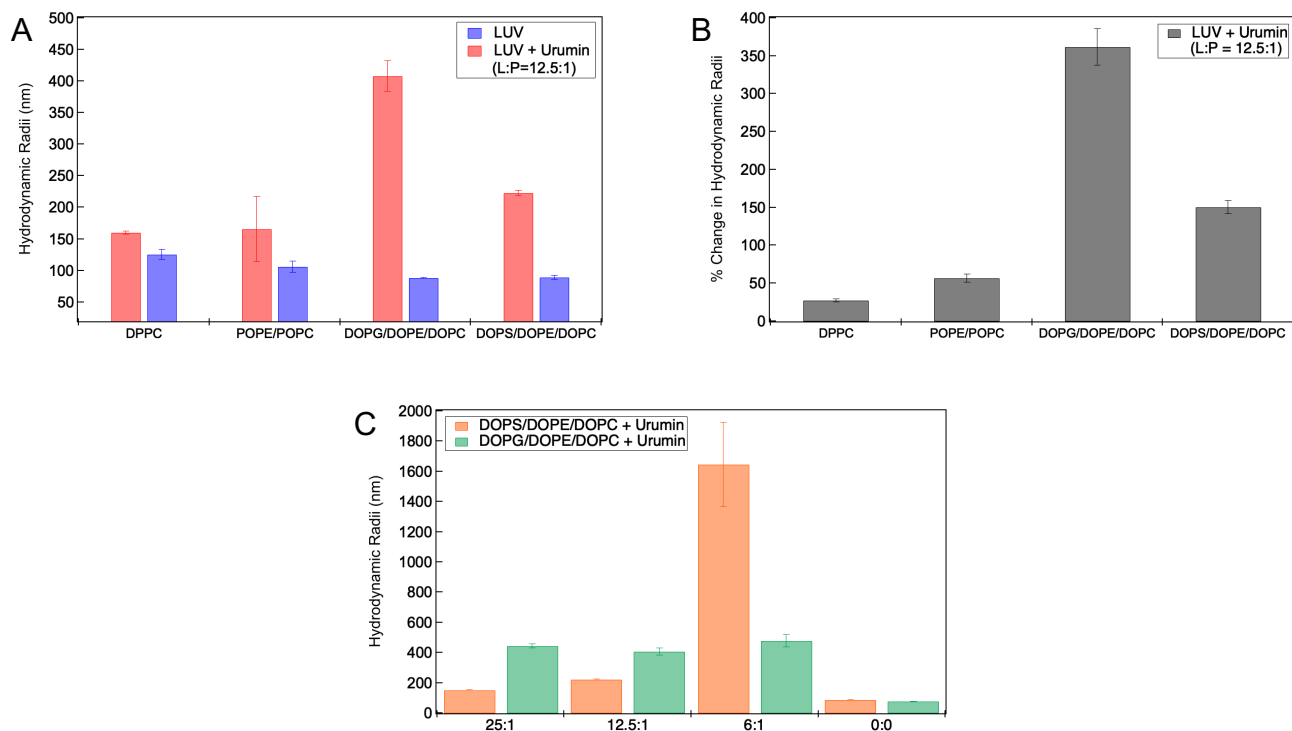
Figure 5.5 Dynamic light scattering of LUVs in the presence or absence of urumin (A) Hydrodynamic radii of LUV and urumin at L:P ratio 12.5:1 (B) Percentage change in hydrodynamic radii of LUV and urumin at L:P ratio 12.5:1 (C) Hydrodynamic radii of DOPS/DOPE/DOPC and DOPG/DOPE/DOPC LUV and urumin at L:P ratios 25:1, 12.5:1, 6:1. 0:0.

The sizes of DPPC, POPE/POPC, DOPS/DOPE/DOPC, and DOPG/DOPE/DOPC liposomes in the absence of urumin varied between 100 and 120 nm in diameter. **(Fig. 5A)** The incubation of urumin with all types of liposomes at a lipid-to-peptide (L:P) ratio of 12.5 to 1 increased the hydrodynamic radii. DOPG/DOPE/DOPC and DOPS/DOPE/DOPC liposomes exhibited the most prominent increase in hydrodynamic radii with a change of 361% and 150%, respectively. In comparison, the sizes of DPPC and POPE/POPC only increased by 27% and 56%. **(Fig. 5C)** Urumin caused an increase in hydrodynamic radii with a decreasing L:P ratio in

DOPS/DOPE/DOPC. Particularly in DOPS/DOPE/DOPC at L:P 6:1, the hydrodynamic radius reached 1645 nm. **(Fig. 5B)** In the presence of urumin, DOPG/DOPE/DOPC liposomes' sizes did not change with decreasing L:P ratio and remained at about 400 nm. **(Fig. 5B)** The increase drastic increase in DOPG/DOPE/DOPC and DOPS/DOPE/DOPC sizes, compared to DPPC and POPE/POPC, suggested that peptides led to membrane aggregation and fusion. Although trp fluorescence and CD showed there were some interactions between urumin with PC and PC/PE lipid, the significant increase in DOPG/DOPE/DOPC and DOPS/DOPE/DOPC liposomes suggests the cationic urumin favors aggregation of the anionic PS and PG lipids over the zwitterionic PE and PC lipids. In DOPS/DOPE/DOPC, as peptide concentration increased (decreasing L:P ratio) and reached a threshold, catastrophic membrane aggregation and fusion caused a further increase in liposome size.

Urumin did not induce liposome leakage

A number of antimicrobial peptides that bind to and fold on lipid membranes have been reported to induce vesicular content leakage.[34] Because urumin disrupted viral integrity as seen in electron microscopy [11], we studied its ability to induce dye leakage from lipid vesicles. A self-quenching concentration (50 mM) of sulforhodamine B dye-entrapped LUVs (DOPS/DOPE/DOPC and DOPG/DOPE/DOPC) were suspended in the buffer, peptide solutions were added, and the kinetics of dye leakage was monitored over time. **Figures 6A and 6B** show the dye leakage profile upon addition of urumin to DOPS/DOPE/DOPC and DOPG/DOPE/DOPC LUVs at varying peptide concentrations. The peptide did not induce significant dye leakage in both vesicles from the lowest concentration (0.207 μM) to the highest concentration (1.67 μm).
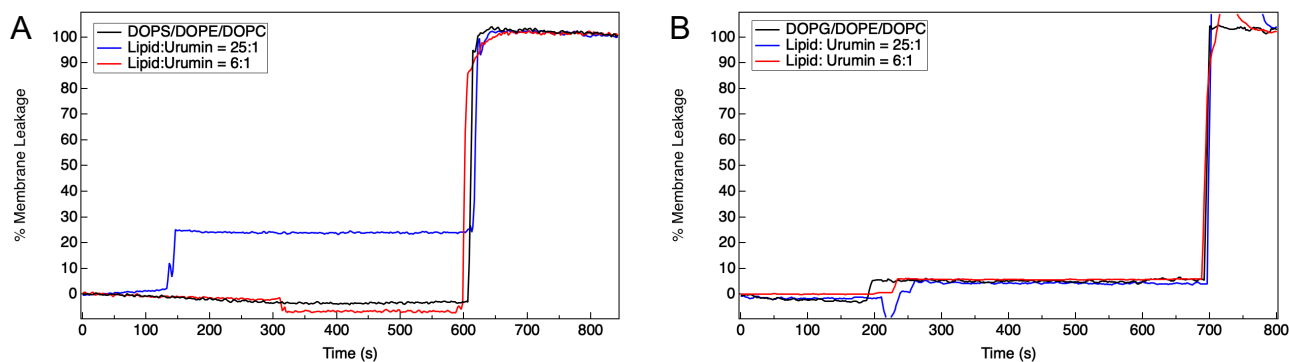
Figure 5.6. Membrane leakage assay. (A) urumin did not induce significant dye leakage in DOPS/DOPE/DOPC. The peptide was added to the LUV solution at 150s, and Triton-X was added at 600s. (B) urumin did not induce leakage in DOPG/DOPE/DOPC after being added to the LUVs at 200s. The addition of Triton-X at 700s resulted in a spike in sulforhodamine B fluorescence due to lysis and dilution.

These data showed that urumin could not permeabilize negatively charged membrane, despite its ability to bind and fold on the membrane. Similar observations have been made in the synthetic antimicrobial peptide. SynSaf synthetic peptides were designed based on class I bacteriocin, a peptide produced by bacterial ribosomes. [35] The SynSaf peptides were unable to induce dye leakage in dye-encapsulated vesicles but still exhibited antimicrobial peptide activity against plant pathogens. Therefore, it is possible that, like the SynSaf peptide, urumin may adopt an alternative antimicrobial and antiviral mechanism of action. Non-lytic activities have also been observed in other host-defense peptides such as bovine lactoferricin, daptomycin and certain peptides with propensities to form beta-sheets. [36]

In summary, trp fluorescence showed that urumin interacted with PC, PS, PG lipid, and CD showed the peptide fold into an alpha helix in the presence of PS and PG lipid. DLS further

showed that the cationic peptide exhibited favorable interaction with anionic PS and PG lipids, leading to catastrophic membrane aggregation. Leakage assay showed that the peptide did not induce sulforhodamine B leakage and therefore did not form a pore in the membrane. These results suggested that the peptide showed selectivity towards PS and PG lipids and could explain the disruption of the PR8 virion containing a high concentration of PS lipid. The peptide could first bind to the negatively charged PS and PG lipids and folds. Then the peptide induces membrane aggregation, particularly in PS lipid.

5.5 Conclusion

In summary, this chapter aims to characterize the structure of urumin, study its interaction with a lipid membrane, and investigate its potential to prevent the pH-driven conformational change in HA2. This study showed that the peptide is disordered in an aqueous solution and maintains its structure at acidic pH. Using model membrane with lipid characteristics to the influenza PR8 virion, this study revealed that urumin interact with PC, PG, and PS lipids, while folding to an alpha helix or beta-sheet with PG or PS lipid. Dynamic light scattering preliminarily showed that urumin could cause lipid aggregation, particularly in LUVs containing PS lipids. urumin failed to induce membrane leakage in LUVs containing PS/PE/PC and PG/PE/PC lipids, suggesting that it disrupts membrane via mechanisms other than pore formation. In addition to studying membrane interactions, we also showed that urumin does not interact with H3N2 X-31 HA2. Unlike other antiviral cyclic peptides, urumin does not inhibit the HA2 protein from undergoing pH-driven conformational change. This suggests that urumin has to inhibit influenza viral growth via other pathways and that membrane aggregation could be a potential mechanism. Additional studies such as measuring binding affinity between the peptide and different lipids with ITC and imaging peptide-

liposome interactions with fluorescence microscopy or TEM could help decipher urumin's viral inhibition mechanism.

5.6 References

1.   Shaw, M. L., The Next Wave of Influenza Drugs. *ACS Infect Dis* **2017,** *3* (10), 691-694.

2.   Gwyer Findlay, E.; Currie, S. M.; Davidson, D. J., Cationic host defence peptides: potential as antiviral therapeutics. *BioDrugs* **2013,** *27* (5), 479-93.

3.   Hancock, R. E.; Sahl, H. G., Antimicrobial and host-defense peptides as new anti-infective therapeutic strategies. *Nat Biotechnol* **2006,** *24* (12), 1551-7.

4.   Wu, W. K.; Wang, G.; Coffelt, S. B.; Betancourt, A. M.; Lee, C. W.; Fan, D.; Wu, K.; Yu, J.; Sung, J. J.; Cho, C. H., Emerging roles of the host defense peptide LL-37 in human cancer and its potential therapeutic applications. *Int J Cancer* **2010,** *127* (8), 1741-7.

5.   Zasloff, M., Antimicrobial peptides of multicellular organisms. *Nature* **2002,** *415* (6870), 389-95.

6.   Albiol Matanic, V. C.; Castilla, V., Antiviral activity of antimicrobial cationic peptides against Junin virus and herpes simplex virus. *Int J Antimicrob Agents* **2004,** *23* (4), 382-9.

7.   Belaid, A.; Aouni, M.; Khelifa, R.; Trabelsi, A.; Jemmali, M.; Hani, K., In vitro antiviral activity of dermaseptins against herpes simplex virus type 1. *J Med Virol* **2002,** *66* (2), 229-34.

8.   Lorin, C.; Saidi, H.; Belaid, A.; Zairi, A.; Baleux, F.; Hocini, H.; Belec, L.; Hani, K.; Tangy, F., The antimicrobial peptide dermaseptin S4 inhibits HIV-1 infectivity in vitro. *Virology* **2005,** *334* (2), 264-75.

9.   Mulder, K. C.; Lima, L. A.; Miranda, V. J.; Dias, S. C.; Franco, O. L., Current scenario of peptide-based drugs: the key roles of cationic antitumor and antiviral peptides. *Front Microbiol* **2013,** *4*, 321.

10.   Yasin, B.; Pang, M.; Turner, J. S.; Cho, Y.; Dinh, N. N.; Waring, A. J.; Lehrer, R. I.; Wagar, E. A., Evaluation of the inactivation of infectious Herpes simplex virus by host-defense peptides. *Eur J Clin Microbiol Infect Dis* **2000,** *19* (3), 187-94.

11.   Holthausen, D. J.; Lee, S. H.; Kumar, V. T.; Bouvier, N. M.; Krammer, F.; Ellebedy, A. H.; Wrammert, J.; Lowen, A. C.; George, S.; Pillai, M. R.; Jacob, J., An Amphibian Host Defense Peptide Is Virucidal for Human H1 Hemagglutinin-Bearing Influenza Viruses. *Immunity* **2017,** *46* (4), 587-595.

12.   Nyanguile, O., Peptide Antiviral Strategies as an Alternative to Treat Lower Respiratory Viral Infections. *Front Immunol* **2019,** *10*, 1366.

13.   Kadam, R. U.; Juraszek, J.; Brandenburg, B.; Buyck, C.; Schepens, W. B. G.; Kesteleyn, B.; Stoops, B.; Vreeken, R. J.; Vermond, J.; Goutier, W.; Tang, C.; Vogels, R.; Friesen, R. H. E.; Goudsmit, J.; van Dongen, M. J. P.; Wilson, I. A., Potent peptidic fusion inhibitors of influenza virus. *Science* **2017,** *358* (6362), 496-502.

14.   Zhao, H.; Zhou, J.; Zhang, K.; Chu, H.; Liu, D.; Poon, V. K.; Chan, C. C.; Leung, H. C.; Fai, N.; Lin, Y. P.; Zhang, A. J.; Jin, D. Y.; Yuen, K. Y.; Zheng, B. J., A novel peptide with potent and broad-spectrum antiviral activities against multiple respiratory viruses. *Scientific reports* **2016,** *6*, 22008.

15.   Lohner, K.; Blondelle, S. E., Molecular mechanisms of membrane perturbation by antimicrobial peptides and the use of biophysical studies in the design of novel peptide antibiotics. *Comb Chem High Throughput Screen* **2005,** *8* (3), 241-56.

16.   Xhindoli, D.; Pacor, S.; Benincasa, M.; Scocchi, M.; Gennaro, R.; Tossi, A., The human cathelicidin LL-37--A pore-forming antibacterial peptide and host-cell modulator. *Biochim Biophys Acta* **2016,** *1858* (3), 546-66.

17.   Henzler Wildman, K. A.; Lee, D. K.; Ramamoorthy, A., Mechanism of lipid bilayer disruption by the human antimicrobial peptide, LL-37. *Biochemistry* **2003,** *42* (21), 6545-58.

18.   Oren, Z.; Lerman, J. C.; Gudmundsson, G. H.; Agerberth, B.; Shai, Y., Structure and organization of the human antimicrobial peptide LL-37 in phospholipid membranes: relevance to the molecular basis for its non-cell-selective activity. *Biochem J* **1999,** *341 (Pt 3)*, 501-13.

19.   Hollmann, A.; Martinez, M.; Maturana, P.; Semorile, L. C.; Maffia, P. C., Antimicrobial Peptides: Interaction With Model and Biological Membranes and Synergism With Chemical Antibiotics. *Front Chem* **2018,** *6*, 204.

20.   Ivanova, P. T.; Myers, D. S.; Milne, S. B.; McClaren, J. L.; Thomas, P. G.; Brown, H. A., Lipid composition of viral envelope of three strains of influenza virus - not all viruses are created equal. *ACS Infect Dis* **2015,** *1* (9), 399-452.

21.   Kelly, S. M.; Jess, T. J.; Price, N. C., How to study proteins by circular dichroism. *Biochim Biophys Acta* **2005,** *1751* (2), 119-39.

22.   Woody, R. W., Circular dichroism. *Methods Enzymol* **1995,** *246*, 34-71.

23.   Greenfield, N. J., Using circular dichroism spectra to estimate protein secondary structure. *Nat Protoc* **2006,** *1* (6), 2876-90.

24.   Lau, S. Y.; Taneja, A. K.; Hodges, R. S., Synthesis of a model protein of defined secondary and quaternary structure. Effect of chain length on the stabilization and formation of two-stranded alpha-helical coiled-coils. *The Journal of biological chemistry* **1984,** *259* (21), 13253-61.

25.   Cooper, T. M.; Woody, R. W., The effect of conformation on the CD of interacting helices: a theoretical study of tropomyosin. *Biopolymers* **1990,** *30* (7-8), 657-76.

26.   Ouberai, M. M.; Wang, J.; Swann, M. J.; Galvagnion, C.; Guilliams, T.; Dobson, C. M.; Welland, M. E., alpha-Synuclein senses lipid packing defects and induces lateral expansion of lipids leading to membrane remodeling. *The Journal of biological chemistry* **2013,** *288* (29), 20883-95.

27.   Wei, G.; Liu, X.; Yuan, L.; Ju, X. J.; Chu, L. Y.; Yang, L., Lipid composition influences the membrane-disrupting activity of antimicrobial methacrylate co-polymers. *J Biomater Sci Polym Ed* **2011,** *22* (15), 2041-61.

28.   Parn, K.; Eriste, E.; Langel, U., The Antimicrobial and Antiviral Applications of Cell-Penetrating Peptides. *Methods in molecular biology* **2015,** *1324*, 223-45.

29.   Li, J.; Koh, J. J.; Liu, S.; Lakshminarayanan, R.; Verma, C. S.; Beuerman, R. W., Membrane Active Antimicrobial Peptides: Translating Mechanistic Insights to Design. *Front Neurosci* **2017,** *11*, 73.

30.   Cummings, J. E.; Vanderlick, T. K., Aggregation and hemi-fusion of anionic vesicles induced by the antimicrobial peptide cryptdin-4. *Biochim Biophys Acta* **2007,** *1768* (7), 1796-804.

31.   Domingues, M. M.; Santiago, P. S.; Castanho, M. A.; Santos, N. C., What can light scattering spectroscopy do for membrane-active peptide studies? *J Pept Sci* **2008,** *14* (4), 394-400.

32.   Gorr, S. U., Antimicrobial peptides of the oral cavity. *Periodontol 2000* **2009,** *51*, 152-80.

33.   Khurshid, Z.; Naseem, M.; Sheikh, Z.; Najeeb, S.; Shahab, S.; Zafar, M. S., Oral antimicrobial peptides: Types and role in the oral cavity. *Saudi Pharm J* **2016,** *24* (5), 515-524.

34.   Raheem, N.; Straus, S. K., Mechanisms of Action for Antimicrobial Peptides With Antibacterial and Antibiofilm Functions. *Front Microbiol* **2019,** *10*, 2866.

35.   Fields, F. R.; Manzo, G.; Hind, C. K.; Janardhanan, J.; Foik, I. P.; Carmo Silva, P. D.; Balsara, R. D.; Clifford, M.; Vu, H. M.; Ross, J. N.; Kalwajtys, V. R.; Gonzalez, A. J.; Bui, T. T.; Ploplis, V. A.; Castellino, F. J.; Siryaporn, A.; Chang, M.; Sutton, J. M.; Mason, A. J.; Lee, S., Synthetic Antimicrobial Peptide Tuning Permits Membrane Disruption and Interpeptide Synergy. *ACS Pharmacol Transl Sci* **2020,** *3* (3), 418-424.

36.   Nguyen, L. T.; Haney, E. F.; Vogel, H. J., The expanding scope of antimicrobial peptide structures and their modes of action. *Trends Biotechnol* **2011,** *29* (9), 464-72.

5.7 Supplemental Information

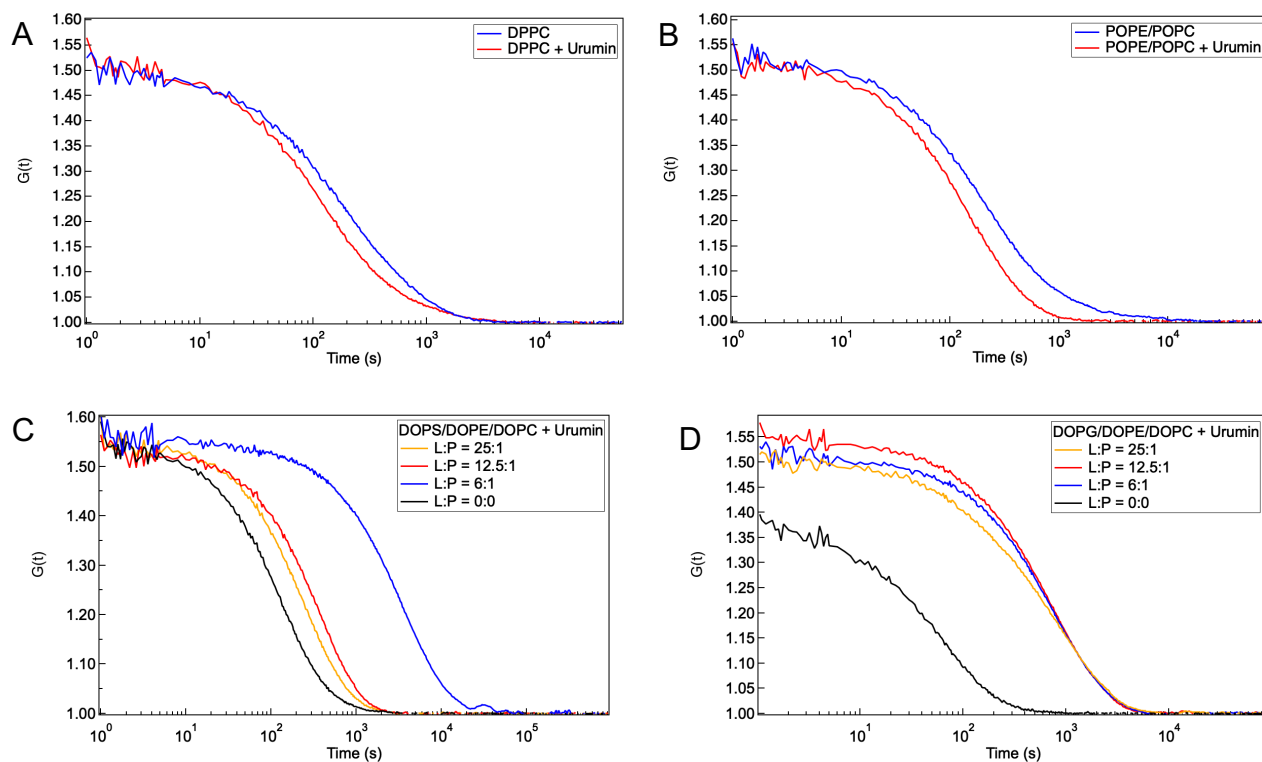*Autocorrelation functions of LUVs and urumin*

Figure S5.1 (A) ACF of DPPC with or without urumin at L:P ratio 12.5:1 (B) ACF of POPE/POPC with or without urumin at L:P ratio 12.5:1. (C) ACF of DOPS/DOPE/DOPC with or without urumin at L:P ratios 12:1, 12.5:1, 6:1, and 0:0. (D) ACF of DOPG/DOPE/DOPC with or without urumin at L:P ratios 12:1, 12.5:1, 6:1, and 0:0.

<div align="center">

Chapter 6:

Conclusion

Hew Ming Helen Siaw

</div>

6.1 Summary

This dissertation aims to study protein and membrane interactions, focusing on protein and peptide conformation changes and their impact on membrane biophysics. Protein-membrane interactions are fundamental to cellular functions and other processes such as viral infection. Specifically, the asymmetric distribution of protein has been recognized as a critical factor to cause membrane remodeling and lead to the formation of vesicles during cargo transport. [1] In the influenza virus, the conformational rearrangement of hemagglutinin generates curvature in both viral and host membrane and leads to fusion. The interactions between protein and lipid membrane extend beyond maintaining biological functions. Antimicrobial peptides and antiviral host-defense peptides secreted by living organisms act as an innate defense barrier against microbial and viral infection. These peptides exert their antimicrobial or antiviral effects by folding on lipid membranes and inducing membrane aggregation and fusion. [2-4]

We investigated the role of protein conformation change on a general membrane bending mechanism, protein crowding, and its impact on membrane bending. Then, we studied the interactions between protein and lipid membrane in a biological context, specifically with the influenza virus. We expressed the H3N2 X31 strain hemagglutinin HA2 subunit, characterized its structure at equilibrium, and resolved sub-millisecond pH-driven protein folding dynamics. Next, we studied and characterized a peptide (L40C) corresponding to the B-loop region of HA2. We use the peptide as a model to HA2 mediated membrane fusion kinetics because of its pH-dependent loop-

to-helix transition and folding into coiled-coil. Lastly, we studied a host defense peptide, urumin, and characterized its interaction with model membranes that mimic the influenza PR8 virus.

6.2 Other contributions

In addition to the studies described in this dissertation, I have also contributed to publication outside of the Dyer group:

- Merg, A. D.; Touponse, G.; Genderen, E. V.; Blum, T. B.; Zuo, X.; Bazrafshan, A.; Siaw, H. M. H.; McCanna, A.; Brian Dyer, R.; Salaita, K.; Abrahams, J. P.; Conticello, V. P., Shape-Shifting Peptide Nanomaterials: Surface Asymmetry Enables pH-Dependent Formation and Interconversion of Collagen Tubes and Sheets. *Journal of the American Chemical Society* **2020,** *142* (47), 19956-19968.

6.3 References

1. Derganc, J.; Copic, A., Membrane bending by protein crowding is affected by protein lateral confinement. *Biochim Biophys Acta* **2016,** *1858* (6), 1152-9.

2. Dugan, A. S.; Maginnis, M. S.; Jordan, J. A.; Gasparovic, M. L.; Manley, K.; Page, R.; Williams, G.; Porter, E.; O'Hara, B. A.; Atwood, W. J., Human alpha-defensins inhibit BK virus infection by aggregating virions and blocking binding to host cells. *The Journal of biological chemistry* **2008,** *283* (45), 31125-32.

3. Zins, S. R.; Nelson, C. D.; Maginnis, M. S.; Banerjee, R.; O'Hara, B. A.; Atwood, W. J., The human alpha defensin HD5 neutralizes JC polyomavirus infection by reducing endoplasmic reticulum traffic and stabilizing the viral capsid. *J Virol* **2014,** *88* (2), 948-60.

4. Wadhwani, P.; Reichert, J.; Burck, J.; Ulrich, A. S., Antimicrobial and cell-penetrating peptides induce lipid vesicle fusion by folding and aggregation. *Eur Biophys J* **2012,** *41* (2), 177-87.